Unveiling the Ansiotropy of Antarctic Ice across Spatial Scales Using Phase Coherent Radar

Dissertation

der Mathematisch-Naturwissenschaftlichen Fakultät

der Eberhard Karls Universität Tübingen

zur Erlangung des Grades eines

Doktors der Naturwissenschaften

(Dr. rer. nat.)

vorgelegt von

Mohammadreza Ershadi

aus Rudbar/IRAN

Tübingen

2023

Gedruckt mit Genehmigung der Mathematisch-Naturwissenschaftlichen Fakultät der Eberhard Karls Universität Tübingen.

Tag der mündlichen Qualifikation:	10.01.2024
Dekan:	Prof. Dr. Thilo Stehle
1. Berichterstatter/-in:	Prof. Dr. Reinhard F. Drews
2. Berichterstatter/-in:	Prof. Dr. Nanna B. Karlsson

Supervised by

Prof. Dr. Reinhard F. Drews

Prof. Dr. Olaf Eisen

Abstract

Climate change and the associated rise in temperatures have raised concerns about Antarctica's substantial contribution to sea level rise and climate change. Evaluating this impact involves utilizing ice flow models, where the implementation of ice rheology plays a crucial role in influencing predictions. Ice is an anisotropic material, meaning as ice flows, crystals within it align in response to compression and extension, forming what is known as "ice fabric." Ice fabric properties significantly affect ice flow dynamics. However, many models currently assume isotropic ice behavior, mainly due to limited observational data and the complexity involved in incorporating ice fabric anisotropy into the models. This assumption poses challenges in accurately predicting Antarctica's impact on sea level rise and climate change. To address this issue and improve the precision of ice flow models, it is essential to develop methodologies to enhance the quantity of observational data pertaining to ice fabric properties, which is the main focus of my doctoral research.

Ice cores provide reliable ice fabric anisotropy observations but are impractical for expanding spatial coverage. Geophysical methods, including seismic and ultrasonic techniques, show potential. However, recent advancements in phase-coherent radar technology, specifically the phase-sensitive radio echo sounder (pRES radar), coupled with improved processing techniques, offer the most promise in bridging the observational gap in ice fabric properties. My thesis focuses on developing a data processing technique to estimate ice fabric properties from pRES radar measurements and mobilizing the pRES system to increase the quantity of the collected data.

The initial phase of my doctoral research involves developing a nonlinear multivariable inverse algorithm, utilizing a matrix-based forward model to simulate radar backscattered signals in an anisotropic medium such as ice. In addition to that, I also developed a technique to approximate the full ice fabric orientation tensor, crucial for parameterizing ice fabric anisotropy in flow models. This method has undergone testing in three separate flow regimes in Antarctica, and the results have been validated through observations from nearby ice cores. Analyzing pRES measurements along a profile on an ice dome has demonstrated that estimated ice fabric anisotropy can reveal the Raymond effect, even when Raymond arches are absent. Although this method resolves ice fabric properties, it is limited by assumptions around initial model parameters, vertical eigenvector, and depth-invariant horizontal ice fabric orientation.

The second phase of my research centers on modifying a commercial rover's hardware and software to develop a data acquisition system. The resultant system, named SLEDGE, is a customized ice rover, towing four pRES antennas in a quad-polarimetric setup on two sleds. It employs RTK GPS for precise positioning and drives autonomously to predefined locations and actively triggers the radar system capable of collecting data for profiles spanning several kilometers. A deployment to Antarctica as proof of concept yielded 23 kilometers of quad-polarimetric

pRES measurements within 20 operational hours, covering 450 points. While the first deployment was a success, SLEDGE requires additional hardware and software refinement for future field deployment.

Overall, the developed inverse approach and SLEDGE, together, show great potential to enhance the spatial coverage of ice fabric properties in the observational data archive—a necessary step towards parameterizing ice fabric anisotropy in ice flow models.

Kurzfassung

Klimawandel und der damit verbundene Anstieg der Temperaturen haben Bedenken hinsichtlich des erheblichen Beitrags der Antarktis zum globalen Anstieg des Meeresspiegels aufgeworfen. Die Bewertung dieses Einflusses erfordert die Verwendung von Eismodellen, wobei die Berücksichtigung der Eisrheologie eine entscheidende Rolle für die Vorhersagen spielt. Eis ist ein anisotropes Material, was bedeutet, dass sich die Kristalle darin beim Fließen aufgrund von Druck und Dehnung ausrichten und eine sogenannte "Kristallstruktur" bilden. Die Eigenschaften der Kristallstruktur beeinflussen die Dynamik des Eisflusses erheblich. Viele Modelle gehen jedoch derzeit von isotropem Verhalten des Eises aus, hauptsächlich aufgrund begrenzter Beobachtungsdaten und der Komplexität bei der Berücksichtigung der Anisotropie der Kristallstruktur in die Modelle. Diese Annahme stellt eine Herausforderung für die genaue Vorhersage des Einflusses der Antarktis auf den Anstieg des Meeresspiegels und den Klimawandel dar. Um dieses Problem anzugehen und die Genauigkeit der Eismodelle zu verbessern, ist es wesentlich, Methoden zu entwickeln, um die Menge an Beobachtungsdaten zur Kristallstruktur zu verbessern, was den Schwerpunkt meiner Doktorarbeit darstellt.

Eisbohrkerne liefern zuverlässige Messungen zur Anisotropie der Kristallstruktur, sind jedoch für eine weite Ausdehnung der räumlichen Abdeckung ungeeignet. Geophysikalische Methoden, einschließlich seismischer und ultraschallgestützter Techniken, zeigen Potenzial. Allerdings bieten jüngste Fortschritte in der phasenkohärenten Radar-Technologie, insbesondere der phasensensitiven Radarecho-Sounder (pRES-Radar), in Verbindung mit verbesserten Verarbeitungstechniken die größte Aussicht, die Beobachtungslücke in den Eigenschaften der Kristallstruktur zu schließen. Meine Dissertation konzentriert sich darauf, eine Datenverarbeitungstechnik zu entwickeln, um die Eigenschaften der Kristallstruktur aus pRES-Radarmessungen abzuschätzen und das pRES-System zu mobilisieren, um die Menge der gesammelten Messdaten zu erhöhen.

Die erste Phase meiner Doktorarbeit beinhaltet die Entwicklung eines nichtlinearen multivariablen inversen Algorithmus unter Verwendung eines matrixbasierten Vorwärtsmodells zur Simulation von Radar-Rückstreusignalen in einem anisotropen Medium wie Eis. Zusätzlich dazu habe ich auch eine Technik entwickelt, um den vollständigen Orientierungstensor der Kristallstruktur abzuschätzen, der für die Parametrisierung der Anisotropie der Kristallstruktur in Flussmodellen ausschlaggebend ist. Diese Methode wurde in drei verschiedenen Flussregimen in der Antarktis getestet, und die Ergebnisse wurden mit Messungen aus nahegelegenen Eisbohrkernen validiert. Die Analyse von pRES-Messungen entlang eines Profils auf einer Eiskuppel hat gezeigt, dass die geschätzte Anisotropie der Kristallstruktur den so genannten Raymond-Effekt offenbaren kann, selbst wenn Raymond-Bögen fehlen. Obwohl diese Methode die Eigenschaften der Kristallstruktur offenbart, wird sie durch Annahmen zu den Anfangsparametern des Modells, dem vertikalen Eigenvektor und der konstanten horizontalen Ausrichtung

der Kristallstruktur mit der Tiefe begrenzt.

Die zweite Phase meiner Forschung konzentriert sich auf die Modifikation der Hardware und Software eines kommerziellen Rovers zur Entwicklung eines Datenerfassungssystems. Das resultierende System, genannt SLEDGE, ist ein individuell angepasster Eisrover, der vier pRES-Antennen in einer quad-polaren Installation auf zwei Schlitten zieht. Er verwendet RTK-GPS für präzise Positionsbestimmung, fährt autonom zu vordefinierten Standorten und löst aktiv das Radarsystem aus, das Daten entlang Profile und über mehrere Kilometer sammeln kann. Ein Probeeinsatz in der Antarktis ergab 23 Kilometer quad-polarimetrischer pRES-Messungen innerhalb von 20 Betriebsstunden und deckte 450 Punkte ab. Obwohl der erste Einsatz erfolgreich war, erfordert SLEDGE zusätzliche Weiterentwicklung von Hardware und Software für zukünftige Feldversuche.

Insgesamt zeigen der entwickelte inverse Ansatz und SLEDGE gemeinsam großes Potenzial, die räumliche Abdeckung der Eigenschaften der Kristallstruktur in der Beobachtungsdatenbank zu verbessern – ein notwendiger Schritt zur vollständigen Parametrisierung der Anisotropie der Kristallstruktur in Eismodellen.

Acknowledgements

Over the past few years, it has been a rollercoaster of challenges and triumphs, and I am genuinely thankful for making it through. The folks who had my back, showed me kindness, and kept me motivated played a massive role in getting me to this point. This dissertation wouldn't be a thing without their valuable contributions. Huge thanks to each one of them, and a special shoutout to:

My Supervisors

Prof. Dr. Reinhard Drews. Reinhard, you've been by my side every step of the way, offering consistent support and friendship that goes beyond the supervisor title. Your scientific insights and the cheerful vibes in the office and the field made this journey memorable. I truly appreciate your constant encouragement. Thank you!

Prof. Dr. Olaf Eisen. Olaf, crossing paths with you was a turning point in my PhD. I not only gained valuable scientific knowledge but also learned how to be an exceptional leader in tough situations. The three months of fieldwork in Antarctica with you were nothing short of incredible, and I absorbed insights from you like I was reading a captivating book every day. Thanks you!

The one and only Geophysics Research Group

Inka, Vjeran, Rebecca, Chris, Alexandra, Clara, Falk, Guy, Akash, Leah, Susanne, Valentina, Anne, Greta, Heiko. Many many thanks for being so amazing. All those coffee times, lunch times, beers, recently cakes, meetings, discussions and fieldworks. You were a big part of my life in the last a few years and I truly enjoyed it. Thanks!

Advisors & Colleagues

Prof. Dr. Erwin Appel.
Erwin, I've always regarded you as my mentor, and your personality, guidance and captivating lectures drew me into the fascinating world of geophysics.

Dr. Carlos Martín.
Carlos, your scientific ideas have made a substantial impact on the success of my research, and I genuinely appreciate your contributions. Also thanks for always being so positive.

Prof. Dr. Todd Ehlers.
Todd, I count myself fortunate for the chance to work with you and your group. Thanks a lot for your consistent supports and insightful advices.

Prof. Dr. Paul Bons.
Paul, your advices has been invaluable, and I'm thankful for your patience in answering all my questions.

Prof. Dr. Andreas Zell & Cognitive system Research Group.
"I greatly expanded my understanding of robotics during my brief stay in your group. Thank you for your friendliness and assistance."

Geodynamics Research Group.
Guys! you've been more than just neighbors; you've been a friendly, kind, and helpful community. Thanks for being awesome.

GUZ Administration, specially Gabi, Wolfgang, and Iris.
You are the best! Friendly, kind and extremely helpful. Much appreciated!

Financial & logistic Supports

My gratitude to *DFG and Emmy Noether Programm* for their financial support during the period of my PhD. Thanks to *AWI Logistics, Neumayer III Station, and the over winterers* for the support during the two Antarctic field seasons. Shoutout to *Martin Petri* for his exceptional friendship and support during the tough field days in Antarctica.

And Ofcourse, Friends & Family

A special thanks to all my friends who were next to me, supported me and kept me motivated throughout this journey. Heartfelt thanks to my family for their support. And finally my little brother. ***Amir***, thanks for being around. It meant so much to me and I am alway proud of you.

And to all those whose names might not be listed but have directly or indirectly contributed to my journey, thank you for your support.

To Mamasi, the best grandma in the galaxy.
Reza - Nov 2023 - Tübingen

من مست و تو دیوانه ما را که برد خانه
صد بار تو را گفتم کم خور دو سه پیمانه
در شهر یکی کس را هشیار نمی بینم
هر یک بتر از دیگر شوریده و دیوانه
Rumi

**"To know is not enough; we must apply.
Willing is not enough; we must do."
Johann Wolfgang von Goethe**

Well, this was not easy. Enduring late-night coding sessions, sleeping in the office, numerous cups of coffee, challenging fieldworks, overcoming failures, persistence, frustration, relentless writing, learning from mistakes, and the list goes on. Ya, this thesis is more than just a scientific document; it's a proof of stubbornness of a man who wouldn't back down. So, a shout-out to myself. I did it.

"Every man has two lives, and the second starts when he realizes he has just one"
Confucius

"In order to be able to think, you have to risk being offensive."
Jordan B. Peterson

در این گیتی سرار گر بگردی
خردمندی نیابی شادمانه
Balkhi

Contents

List of Figures

List of Tables

List of Publications

- ORCiD: 0000-0002-8929-1638
- Google Scholar: M. Reza Ershadi

FIRST AUTHOR

1. Published in *The Cryosphere Journal*,
Ershadi, M. R., Drews, R., Martín, C., Eisen, O., Ritz, C., Corr, H., Christmann, J., Zeising, O., Humbert, A., and Mulvaney, R.: Polarimetric radar reveals the spatial distribution of ice fabric at domes and divides in East Antarctica, The Cryosphere, 16, 1719–1739, https://doi.org/10.5194/tc-16-1719-2022, 2022.
2. Submitted for publication in *Journal of Glaciology*,
September 2023.
Ershadi, M. R., Drews, R., Henry, A. C. J., Oraschewski, F. M., Martín, C., Tison, J. L., Tsibulskaya V., Sun, S., Wauthy, S., Koch, I., Bons, P., Eisen, O., and Pattyn, F.: Investigating the dynamic history of a promontory ice rise using radar data.
3. Submitted for publication in *IEEE Transactions on Geoscience and Remote Sensing*,
October 2023.
Ershadi, M. R., Drews, R., Hawkins, J., Elliott, J., Lines, A. P., Koch, I., and Eisen, O.: Autonomous Rover Enables Radar Profiling of Ice-Crystal Fabric in Antarctica.

COAUTHOR

1. Published in *The Cryosphere Journal*,
Zeising, O., Gerber, T. A., Eisen, O., **Ershadi, M. R.**, Stoll, N., Weikusat, I., and Humbert, A.: Improved estimation of the bulk ice crystal fabric asymmetry from polarimetric phase co-registration, The Cryosphere, 17, 1097–1105, https://doi.org/10.5194/tc-17-1097-2023, 2023.
2. Published in *Nature Communications*,
Gerber, T.A., Lilien, D.A., Rathmann, N.M. **et al**. Crystal orientation fabric anisotropy causes directional hardening of the Northeast Greenland Ice Stream. Nat Commun 14, 2653 (2023). https://doi.org/10.1038/s41467-023-38139-8
3. Published in *Journal of Glaciology*,
Lilien, D.A., Rathmann, N.M., Hvidberg, C.S., Grinsted, A., **Ershadi, M.R.**, Drews, R., Dahl-Jensen, D. Simulating higher-order fabric structure in a coupled, anisotropic ice-flow model: application to Dome C. Journal of Glaciology, https://doi.org/10.1017/jog.2023.78, 2023.
4. Submitted for publication in *The Cryosphere Journal*,
November 2023.
Oraschewski, F. M., Koch, I., **Ershadi, M. R.**, Hawkins, J., Eisen, O., and Drews, R.: Layer-optimized SAR processing with a mobile phase-sensitive radar for detecting the deep englacial stratigraphy of Colle Gnifetti, Switzerland/Italy, EGUsphere [preprint], https://doi.org/10.5194/egusphere-2023-2731, 2023.

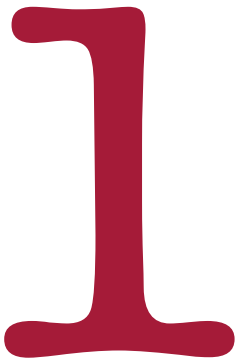

Chapter 1

Introduction

1.1 Antarctica and Global Warming

The figures in this chapter are created by the author of this thesis.

The continuous emission of greenhouse gases has led to the occurrence of global warming (Intergovernmental Panel on Climate Change (IPCC), 2023). As the Earth's temperature continues to rise, the oceans, which cover over 70% of the Earth's surface and possess high heat capacity, undergo warming. This warming effect is most consequential in Antarctica, where ice directly interacts with the ocean, initiating a sequence of events marked by basal melting and iceberg calving (Williams et al., 1998; Bintanja et al., 2015; Rintoul et al., 2016; Assmann et al., 2019; Robel et al., 2022; Russell, 2023; Naughten et al., 2023; Lauber et al., 2023).

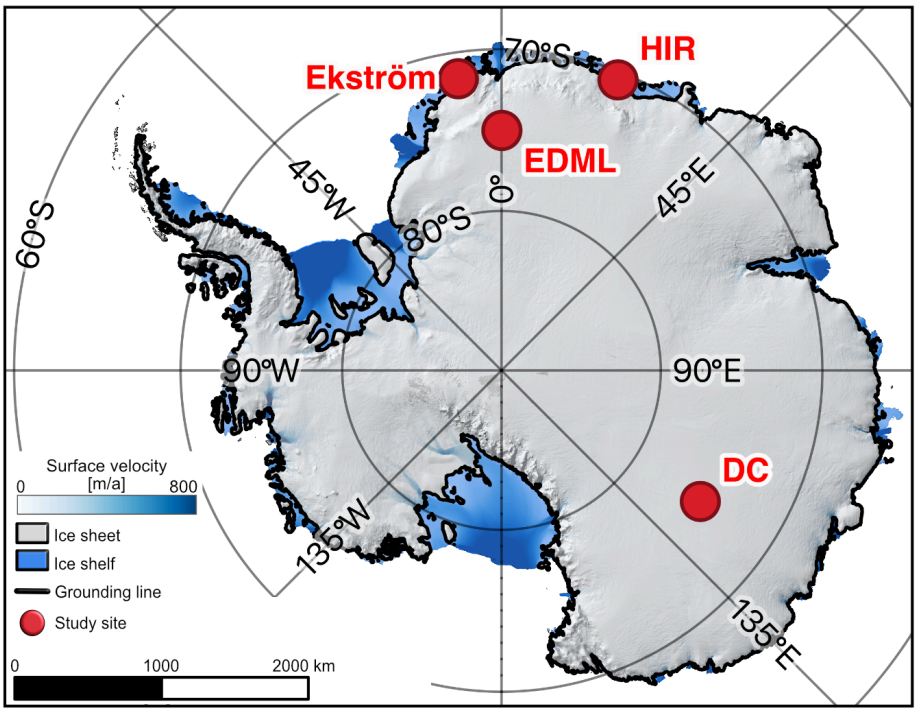

Figure 1.1: Map of Antarctica showing the surface flow velocity (Rignot et al., 2017) along with the grounded ice (ice sheet) and floating ice (ice shelf) separated by the grounding line. Elevation DEM by Helm et al. (2014).The red circles are the study sites in this thesis as Dome C (DC) and EPICA Dronning Maud Land (EDML) from chapter 2, Hammarryggen Ice Rise (HIR) from chapter 3 and Ekström Ice Shelf from chapter 4.

In Antarctica, the accumulated snow in the interior of the continent turns to ice (more on this in Sect. 1.3) and undergoes a dynamic transformation as gravitational forces compel it to flow towards the coastal regions. This flow behavior is visually depicted in Fig. 1.1. Within the grounded ice (ice sheet - white area in Fig. 1.1), the ice exhibits slow movement. As the ice approaches the grounding line (black line in Fig. 1.1) and becomes floating (ice shelf - blue area in Fig. 1.1) a significant acceleration in ice velocity becomes evident. This transition in flow behavior at the grounding line is a critical aspect of Antarctica's ice dynamics, with implications

for ice-shelf stability.

Antarctica serves as a crucial climate archive for the Earth (Brook and Buizert, 2018). Its impact extends significantly to both the Earth's climate and ocean systems.

- **Ice-shelf buttressing** While collapsing ice shelves do not contribute directly to rising sea levels because they are already attributed to floating on the ocean, they do offer a safety band. The disintegration of ice shelves weakens the stabilizing influence that once restrained grounded ice progression towards the ocean, commonly referred to as the "buttressing effect". With the reduction of these ice shelves, more ice is discharged, flowing seaward (Gudmundsson, 2013; Haseloff and Sergienko, 2018; Andreasen et al., 2023) The cumulative outcome is a substantial contribution to the rise in sea levels.

- **Ocean circulation** Observations over recent decades indicate an acceleration in mass loss from Antarctica, particularly in regions experiencing rapid ice shelf melt (Shepherd et al., 2018; Rignot et al., 2019). The melting of the grounded ice sheet and fringing floating ice shelves contributes freshwater to the Southern Ocean, impacting ocean circulation by diluting salinity (Seidov and Haupt, 2005). This phenomenon is expected to have substantial effects, contributing to feedback in global climate change (Rignot and Jacobs, 2002; Fyke et al., 2018; Bronselaer et al., 2018; Dong et al., 2022).

- **Ice-albedo feedback** Although, the impact of this phenomenon is more pronounced within sea ice and Greenland than in the Antarctic ice sheet itself it worth to be mentioned here. Antarctica's extensive snow cover plays a crucial role in the Earth's climate regulation by directly reflecting a considerable portion of incoming solar radiation back into space. This reflection assists in sustaining the frigid temperatures characteristic of polar regions. As the ice gradually recedes, the albedo, or reflective capacity, diminishes (Wendler and Kelley, 1988; Pirazzini, 2004; Seo et al., 2016; Bergstrom et al., 2020). Consequently, more heat is absorbed, initiating a self-perpetuating cycle of further melting, and warming.

In this context, a comprehensive understanding of Antarctica's future impact on global sea-level rise becomes of paramount importance. To accomplish this, it is essential to understand the intricate mechanics of its ice dynamics, a task optimally pursued through the utilization of advanced **ice-flow models**.

1.2 Ice Flow Models

Ice flow models are important to understand Antarctica's response to the global warming. They are indispensable tools for unraveling the broader implications for the Earth's climate system and the imminent challenges associated with increasing sea levels. Ice-flow models such as ELMER (Gagliardini et al., 2013) and PISM (Winkelmann et al., 2011) are mathematical representations of the physical processes governing the flow of ice serve as a fundamental framework for formulating the behavior of glacial ice. They are primarily relay on numerically solving the ful set or approximation of Stokes equations combined with the Glen's flow law (Glen, 1952; Glen and Perutz, 1997), which defines the rheology of ice. These models enable the simulation of ice-flow dynamics and an exploration of how ice masses have reacted to historical climatic variations (Schannwell et al., 2020). Moreover, they provide crucial insights into the response of these ice bodies to contemporary and future climate changes (Fürst et al., 2015) and ultimately

sea-level rise (Edwards et al., 2021). These models require the implementation of numerous parameters such as the geometry and velocity of ice, mass balance (impact of atmospheric and oceanic forcing) and properties of ice, e.g., density, viscosity, temperature. The accurate integration of these parameters into the ice-flow models significantly influence their predictions.

Attention is warranted towards a crucial aspect - the often overly simplified parameterization of ice rheology, influenced by **ice-fabric anisotropy**, acknowledged as one of the less comprehended phenomena in glaciology (elaborated in the following section). Despite commendable research efforts (Azuma, 1994; L.Wang and Warner, 1999; Gillet-Chaulet et al., 2005; Seddik et al., 2008; Martín et al., 2009a; Seddik et al., 2011; Martín and Gudmundsson, 2012; Graham et al., 2018; Lilien et al., 2023), this aspect remains inadequately represented in present-day models owing to limitations in observations and model complexity. It is imperative to recognize that most of the models conceptualize ice as an isotropic material, whereas ice is both mechanically and dielectrically anisotropic (direction dependent). Consequently, this existing model framework introduces uncertainty in predicting the future trajectories of polar ice sheets and glaciers.

1.3 Ice Fabric Anisotropy

To understand ice fabric anisotropy we must begin with the formation of ice crystals. The process begins with the compaction of snowflakes, where older snowflakes become buried under the overburden weight of new snowfall. This overburden pressure transforms snowflakes into individual ice crystals, commonly referred to as ice I_h (Hooke, 2005), featuring a hexagonal crystalline structure with a basal plane comprised of hexagonal oxygen rings (Fig. 1.2a) where the ice is softer and deforms preferentially on this plane by slip (Duval et al., 1983). The determination of the c-axis, perpendicular to the basal plane, relies on the orientation of the fourth oxygen atom within a tetrahedral configuration (Hooke, 2005).

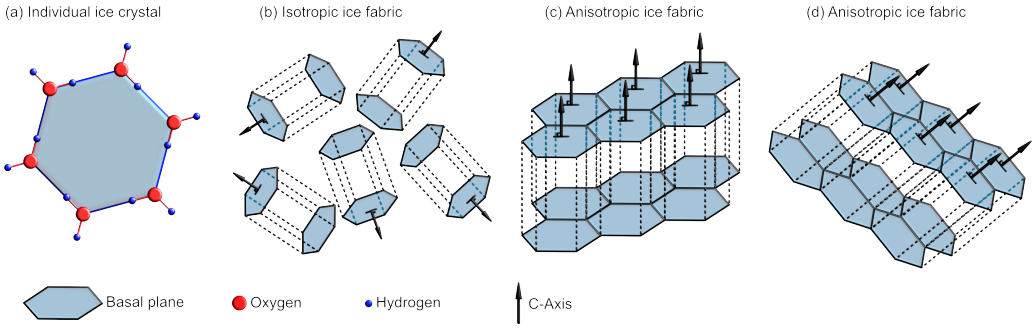

Figure 1.2: (a) The hexagonal shape of an individual ice crystal. (b) Several ice crystals forming isotropic fabric. (c) and (d) Several ice crystals forming anisotropic fabric in two different directions.

Initially, ice crystals are randomly oriented (Fig. 1.2b). As time progresses, the collective mass of ice starts to mobilize and flow. Under various stress conditions, the ice crystals undergo deformation (strain). In response to stress, individual crystals accommodate this deformation by rotating and/or merging with neighboring crystals. Rotation of ice crystals tends towards a

specific orientation relative to the applied stress (Gow and Williamson, 1976). In general, individual ice crystals tend to rotate towards the direction of compression and away from extension, leading to a common alignment of randomly oriented crystals (Fig. 1.2b&c). This overall preferential alignment culminates in the formation of what is commonly known as Lattice Preferred Orientation (LPO), Crystal Preferred Orientation (CPO), Crystal Orientation Fabric (COF), or simply ice fabric (terminology of this thesis).

The assessment of ice fabric anisotropy finds application in two significant areas.

1. Ice fabric embodies the accumulated strain and stress history of the ice sheet, offering insights into its integrated flow history (Doake et al., 2003; Llorens et al., 2022). Therefore, the current state of ice fabric is an indication of the strain experienced by the ice that can be used to understand the ice rheology of the area.

2. Ice fabric significantly influences ice rheology, determining how ice flows. The generation of different types of ice fabric during ice flow impacts both ice viscosity and texture. This, in turn, shapes the behavior of ice flow in diverse ways (Budd and Jacka, 1989; Alley, 1992; Azuma, 1994; Pettit et al., 2007; Llorens et al., 2022; Gerber et al., 2023). Thus, the incorporation of ice fabric knowledge into ice-flow models enhances the precision of predicting future ice-flow behavior. Conversely, neglecting to account for ice fabric can lead to inaccurate predictions of sea level rise.

The primary method to measure ice fabric involves the analysis of thin sections of ice cores under polarized microscopes (fabric analyzer) in the laboratory. Each ice crystal reflects the emitted polarized light in a distinct colors corresponding to its c-axis direction (Azuma et al., 1999; Durand et al., 2009; Montagnat et al., 2014; Weikusat et al., 2017). Subsequently, these c-axes are projected onto a sphere to create a Schmidt diagram (Fig. 1.3), representing the ice fabric type in the form of the bulk distribution of c-axis. The ice fabric is mainly categorized in three types which are isotropic where crystals are distributed in random directions (Fig. 1.3a), girdle where crystals are forming a belt (Fig. 1.3b) and cluster where crystals are pointing towards the same direction (Fig. 1.3c).

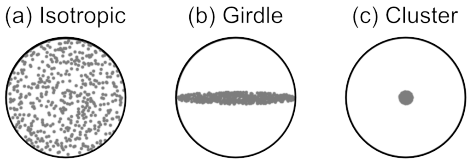

Figure 1.3: An example of c-axis distribution on a Schmidt diagram demonstrating the three main ice fabric types.

Directly observing and measuring the c-axis orientation in ice cores provides a unique characterization of its fabric. Conversely, geophysical methods (to be further discussed) estimate and depict the bulk ice-fabric properties. The bulk ice fabric pattern is described with a second-order orientation tensor (Gödert, 2003; Gillet-Chaulet et al., 2006; Martín et al., 2009a) using the eigenvectors ($\mathbf{v_1}$, $\mathbf{v_2}$, and $\mathbf{v_3}$) and eigenvalues (λ_1, λ_2, and λ_3) of an ellipsoid that best represents the average c-axis orientation of all ice crystals in the sample. Normalizing the eigenvalues as $\lambda_1 + \lambda_2 + \lambda_3 = 1$, with the hierarchy $\lambda_1 < \lambda_2 < \lambda_3$, categorizes primary ice fabric types as isotropic ($\lambda_1 \simeq \lambda_2 \simeq \lambda_3$), girdle ($\lambda_1 \ll \lambda_2 \simeq \lambda_3$), and cluster ($\lambda_1 \simeq \lambda_2 \ll \lambda_3$). Assuming one

The effect of tilted $\mathbf{v_3}$ is studied by Jordan et al. (2019, Appendix A) and Rathmann et al. (2022)

eigenvector is oriented vertically (e.g., $\mathbf{v_3}$), and the other two eigenvectors are in the horizontal plane ($\mathbf{v_1}$ and $\mathbf{v_2}$), it is possible to determine the magnitude of ice fabric anisotropy in the horizontal ($\Delta\lambda_H = \lambda_2 - \lambda_1$) and vertical ($\Delta\lambda_V = \lambda_3 - \lambda_2$) directions, as well as the orientation of horizontal ice fabric anisotropy ($\mathbf{v_1}$ and $\mathbf{v_2}$).

Woodcock (1977) proposed a visualization technique of fabric shape and strength (not necessarily for ice) which is applicable across various Earth science branches including glaciology (ice fabric). In this technique the most relevant Schmidt diagram (ice fabric type) can be determined using the eigenvalues. This is achievable through the definition of $K = \frac{\ln(\lambda_3/\lambda_2)}{\ln(\lambda_2/\lambda_1)}$ and $C = \ln(\lambda_3/\lambda_1)$. The K value distinguishes between cluster and girdle fabric types, whereas the C value quantifies the randomness of the c-axis distribution within the fabric. Illustrated in Fig. 1.4, the fabric type is delineated based on K, C, $\Delta\lambda_H$, and $\Delta\lambda_V$. Ice cores, while valuable

This figure is based on (Woodcock, 1977, Fig. 1).

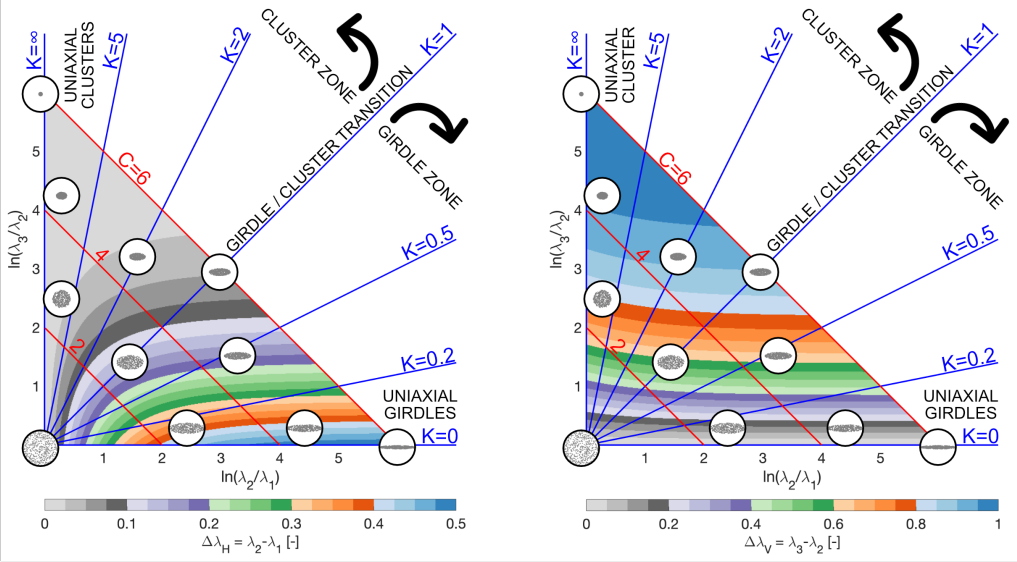

Figure 1.4: Both figures depict the distribution of ice fabric type based on K and C values. The background color on the left and right figures show the horizontal and vertical anisotropy, respectively.

sources of information on ice fabric anisotropy, possess inherent limitations. Determining the orientation of ice fabric from ice core observations presents a challenge due to the absence of reference in the orientation of ice core samples, despite attempts have been made to reconstruct the sample orientations (Westhoff et al., 2020). Furthermore, the distribution of ice cores is primarily optimized to collect paleoclimate records, typically positioned at ice domes, ice divides, or shallow flanks with unique flow characteristics (Thorsteinsson et al., 1997; Diprinzio et al., 2005; Montagnat et al., 2012; Faria et al., 2014b). As a result, there is a shortage of observations regarding the spatial distribution of how ice-fabric anisotropy evolves along the flow of ice.

In addition to ice cores, geophysical methods such as seismic techniques, ultrasonic measurements, and radar-based approaches are employed to investigate ice fabric anisotropy. The seismic method encounters challenges, including limitations in depth assessment and complexities in interpreting reflection amplitudes (Diez et al., 2014; Picotti et al., 2015; Smith et al., 2017).

Ultrasonic sounding measurements present a more accessible approach for detecting anisotropy; however, this method necessitates frequencies within the range of KHz to MHz and the utilization of boreholes or ice cores (Bentley, 1972; Gusmeroli et al., 2012). In contrast, radar-based investigations offer a more logistically feasible application for wide area data acquisition. However, conventional radar measurements on ice sheets are insufficient for estimating ice fabric properties as they only record amplitude variations of the reflected signal.

The hexagonal structure of ice crystals (Fig. 1.2a) and their anisotropic formation render ice a birefringent medium, wherein the backscattered radar signal depends on the polarization direction of the transmitted wave (Doake, 1981). When a linearly polarized electromagnetic wave permeates this medium, it splits into two distinct waves: the ordinary wave and the extraordinary wave, perpendicularly polarized and generally differing in wave speed. Ice crystals are uniaxial (i.e., two out of three principal components of the dielectric tensor are equal), therefore, an ordinary wave and an extraordinary wave overlap. The azimuth dependency of the backscattered power results from both anisotropic scattering and birefringence, which possess different symmetries (Hargreaves, 1977). Within birefringence, amplitude variation arises from the superposition of the two characteristic waves with a phase shift. Therefore, quantifying this phenomenon entails measuring the phase shift between the transmitted and received signal. Nevertheless, effective use of radar to estimate ice fabric properties necessitates the application of multi-frequency and multi-polarization analyses with **phase-coherent radar** systems capable in storing precise phase shifts.

1.4 Phase Coherent Radar

Radar technology has established itself as an essential instrument for investigating the interior of polar ice (Eisen et al., 2003, 2007; Drews et al., 2012, 2015b, 2017; Schroeder, 2023), glaciers (Eisen et al., 2011; Nobes, 2011; Church et al., 2021), and planetary bodies characterized by ice (Seu et al., 2007; Holt et al., 2008; Karlsson et al., 2015), primarily due to its low signal attenuation within the ice medium. A standard radar system consists of a transmitting antenna that emits electromagnetic waves at specific frequencies into the ice and a receiving antenna that records the resulting backscattered signals. The complex nature of ice properties, encompassing attributes such as density, acidity, and anisotropy, evolves with increasing depth, thereby influencing the characteristics of the radar signals that are reflected.

Traditional radar surveys on ice, encompassing satellite-based (e.g., Goldstein et al., 1993; Thompson et al., 2020; Surawy-Stepney et al., 2023), airborne (e.g., Tabacco et al., 2002; Matsuoka et al., 2004; Frémand et al., 2022; Franke et al., 2022), and ground-based radar (e.g., Arcone, 1996; Eisen et al., 2003) methodologies, have been extensively utilized to assess fundamental parameters including ice thickness (e.g., Griggs and Bamber, 2011; Chuter and Bamber, 2015), subglacial topography (e.g., Ridley et al., 1993; Tsutaki et al., 2022), and the internal stratigraphy of ice bodies (e.g., Franke et al., 2023; Wang et al., 2023) for establishing chronological associations with events recorded in ice cores, such as volcanic eruptions, thereby facilitating the development of critical age-depth relationships.

In the field of glaciology, a ground-based Autonomous phase-sensitive Radio Echo Sounder, referred to as ApRES radar (Brennan et al., 2014; Nicholls et al., 2015), has been designed for extended field deployments due to its autonomous and energy-efficient iteration. ApRES radar is an advanced variant of pRES radar (Corr et al., 2002) where its roots can be traced back to the 1970s when its foundational principles were established at the University of Bristol (e.g.,

Walford and Harper, 1981).

The ApRES radar, characterized as a phase-coherent radar system, possesses the capability to comprehensively untangle scattering phenomena within ice sheets across a broad frequency spectrum. It is a stepped frequency radar that uses inverse Fourier transform for the recovery of the impulse response while preserving phase information. This approach substantially augments measurement precision, achieving a signal-to-noise ratio of 17 dB. It facilitates the detection of exceedingly subtle phase variations, as minor as 1°, equivalent to a mere 1 mm range deviation (Brennan et al., 2014; Nicholls et al., 2015). ApRES employs the frequency-modulated continuous wave (FMCW) technique, enabling the transmission of linearly polarized electromagnetic waves within the 200 to 400 MHz frequency range over a one-second interval to produce a chirp. This versatile system operates effectively in both attended and unattended modes (autonomous), exhibiting resilience even in extreme cold, with operational capabilities extending to temperatures as low as -40°C. Additionally, it integrates an Iridium data link and GPS receiver to ensure precise timing (Nicholls et al., 2015). A notable innovation of ApRES lies in its capacity to switch between up to eight transmit and eight receive antennas, a feature that substantially enhances its imaging capabilities and its ability to resolve intricate return signals from the ice by collecting data in different polarization.

The adaptability of this radar extends to the measurement of critical parameters such as rates of basal melt beneath ice shelves as its main purpose (Corr et al., 2002; Jenkins et al., 2006; Dutrieux et al., 2013; Zeising et al., 2022). Furthermore, it is proficient in monitoring the vertical movement of internal ice layers and delineating profiles of vertical ice strain, as demonstrated by Kingslake et al. (2014). These measurements provide insights into vertical strain rates and the compaction of firn layers within ice sheets, contributing to the development of age-depth relationships essential for the interpretation of climatic records stored in ice cores (Gillet-Chaulet et al., 2011; Kingslake et al., 2014). The ApRES radar is also capable of dealing with complex data scenarios, such as those involving multiple returns from the basal reflector (Vaňková et al., 2021). In the context of detecting ice fabric anisotropy from radar data, as mentioned earlier, it is crucial to utilize a multi-frequency and multi-polarization phase-coherent radar capable of recording phase shifts between the transmitted and received signals. This makes the ApRES radar, an instrument, that holds the potential to unveil ice fabric properties (Brisbourne et al., 2019; Jordan et al., 2019).

1.5 Previous Studies on Radar and Anisotropy

References cited in this section predate the initiation of this study in 2019.

The research on electromagnetic wave propagation in birefringent media, particularly in polar ice, has seen significant activity. Studies by Hargreaves (1977, 1978); Ackley and Keliher (1979); Woodruff and Doake (1979); Doake (1981) primarily focused on theoretical aspects. Another set of investigations were conducted by Fujita and Mae (1993); Liu et al. (1994); Fujita et al. (1999, 2003, 2006); Siegert and Kwok (2000); Doake et al. (2002); Matsuoka et al. (2003, 2004); Eisen et al. (2007); Wang et al. (2008); Dall (2010); Drews et al. (2012), centered around multi-frequency and multi-polarization radar measurements. These studies provided valuable insights into characterizing ice fabric from polarimetric radar measurements.

Traditionally, algorithms for radio-wave birefringence propagation have primarily utilized simple convolution (Moore, 1988; Miners et al., 1997; Kohler et al., 2003) or numerical expressions of Maxwell's equations (Kanagaratnam et al., 2001; Miners et al., 2002; Eisen et al., 2003). Fujita et al. (2006) introduced a matrix-based approach, influenced by geometrical optics, to model

radio-wave birefringence in ice sheets. This method addresses the layered structure of ice, allowing for easy expansion and flexibility. The model accounts for the anisotropic properties of ice and integrates contemporary insights into radio-wave backscatter, facilitating the examination of the two-way travel of depolarized radio waves within birefringent ice. It is capable of handling multiple anisotropic and isotropic scattering interfaces.

While it is imperative to acknowledge that none of the prior studies directly presented a method for the estimation of ice fabric anisotropy from radar data, Fujita's foundational work represented a significant advancement in comprehending the patterns subsequently observed in pRES [1] radar data, as shown later by Brisbourne et al. (2019) and Jordan et al. (2019).

The next step towards estimating ice fabric anisotropy from pRES data was introduced by Jordan et al. (2019). He proposed a method that entails coherence phase analysis between co-polarized [2] and cross-polarized [3] pRES data, which was later expanded to collecting pRES data in quad-polarimetric mode [4]. Under the assumption that one eigenvector is oriented vertically, if the two signals exhibit a certain degree of coherence, then the depth gradient of the coherent phase along either of the two main optical axes can serve as an estimate of horizontal ice fabric anisotropy ($\Delta\lambda_H$). This approach marked a significant advancement in the inference of ice fabric anisotropy from pRES radar data.

The introduction of pRES as a phase-coherent radar (Brennan et al., 2014; Nicholls et al., 2015), along with the matrix-based model proposed by Fujita et al. (2006) and the coherence phase analysis technique developed by Jordan et al. (2019), marks a significant milestone in the endeavour to estimate ice fabric properties from radar data. These pioneering steps lay the groundwork for the primary objectives of the present study.

1.6 Research Questions in this Study

In the previous sections, I highlighted the significance of ice fabric anisotropy in ice rheology, directly impacting ice flow behavior. The prevailing treatment of ice as isotropic in many ice flow models poses challenges in accurately predicting Antarctica's influence on sea level rise and climate change. This limitation primarily arises due to the insufficient observation of spatial changes in ice fabric anisotropy. **To bridge this gap, my doctoral research is fundamentally driven by the question of how we can significantly enhance observational knowledge of spatial ice fabric properties distribution**. Leveraging the promising potential of the pRES radar in detecting ice fabric properties and its logistical advantages in the field, my research focus is centered on harnessing this technology. This choice leads to the pursuit of two main research questions:

1. ***How can a method be developed to estimate ice fabric properties from quad-polarimetric pRES radar data?***

2. ***How can an autonomous rover be designed to collect quad-polarimetric pRES radar data at predetermined locations?***

[1] The data in this study were collected using ApRES radar, although we did not utilize its unattended/autonomous feature. Consequently in this thesis, with the exception of Chapter 2 and its Appendix (6), the term ApRES has been substituted with pRES.

[2] The polarization direction in both the transmitter and receiver antennas are in the same direction.

[3] The polarization direction in the transmitter and receiver antennas differ by 90 degrees.

[4] Collecting pRES data in four different antenna orientations.

1.7 General Approach

The primary approach adopted in this study hinges upon the exploitation of ice's birefringent characteristic, to infer ice fabric anisotropy from the phase shifts deduced from pRES radar signals. The radar data utilized in this study were obtained employing the pRES radar system in quad-polarimetric mode, a specialized data acquisition method utilizing four distinct antenna polarization combinations enabling the reconstruction of a full azimuthal signal for precise tracing of the ice fabric properties. This configuration is briefly introduced in Chapter 2 (Sect. 2.3.3) and thoroughly expounded upon in Chapter 4 (Sect. 4.2.4) and Chapter 6 (Sect. 6.5). The principal methodology employed in this study centers around the formulation of a non-linear multivariable inverse approach, making use of the existing matrix based forward model. Within this method, the algorithm is tasked with optimizing estimations for magnitude ($\Delta\lambda_H$) and orientation ($\mathbf{v_1}$ & $\mathbf{v_2}$) of the horizontal ice fabric anisotropy at varying depths of the ice column, enabling the forward model to replicate the observed radar data. A comprehensive explanation of this methodology is presented in the preliminary section of Chapter 2, supplemented by further details provided in Chapter 6.

1.8 Thesis Structure

Chapter 2 In this chapter, I address the first research question, aiming to develop a method for estimating ice fabric properties from quad-polarimetric pRES data. I explore the impact of birefringence and ice fabric anisotropy on the backscattered polarimetric radar signal. Sensitivity tests on the existing matrix-based forward model (Fujita et al., 2006) are conducted to analyze these effects. Subsequently, a non-linear multivariable inverse approach is developed to optimize ice fabric properties in Fujita's model, ensuring the reproduction of observed radar patterns. The method is then extended to estimate the full orientation tensor of ice fabric using the obtained ice fabric anisotropy from the inverse approach. Validation of the effectiveness of the developed method is achieved by comparing the estimated ice fabric anisotropy with observations from nearby ice cores in two distinct flow regimes, Dome C (DC in Fig. 1.1) and Dronning Maud Land (EDML in Fig. 1.1). Finally, evidence is provided in the appendix, demonstrating the synthesis of a full azimuthal signal using quad-polarimetric radar. Chapter 6 is the appendix of this chapter.

Chapter 3 In this chapter, I applied the developed inverse method from the previous section to analyze a 5 km quad-polarimetric pRES data set collected on Hammarryggen ice rise (HIR in Fig. 1.1). Hammarryggen is a promontory ice rise, and its flow is influenced by a triple junction geometry, resulting in a relatively complex flow regime. The primary objectives of this chapter are twofold. Firstly, to assess the accuracy of the inverse method in estimating ice fabric anisotropy within this intricate flow regime by comparing the estimated values with those observed in the nearby ice core. Secondly, to combine various observations, including ice fabric anisotropy from pRES radar, internal reflection horizons from airborne radar, vertical strain rate over a year from pRES data, and the estimated horizontal strain rate from the Shallow Ice Approximation. The aim is to determine if the ice fabric anisotropy derived from quad-polarimetric pRES data in a profile has the potential to unveil the ice dynamics history and the stability of ice rises. Chapter 7 is the appendix of this chapter.

Chapter 4 In this chapter, I address the second research question, focusing on the technical aspects of developing a rover-based data acquisition system. This system is designed to

autonomously collect quad-polarimetric pRES data at predetermined locations utilizing GPS. The details of constructing this system and outlining its key components are presented. The initial deployment of the system to the grounding zone of Ekström Ice Shelf in Antarctica (Ekström in Fig. 1.1) is documented. A total of 450 measurement points covering approximately 23 kilometers of quad-polarimetric data were gathered during this deployment, within a 20-hour operational timeframe. Chapter 8 is the appendix of this chapter.

Chapter 5 In this chapter, I conclude my thesis by summarizing the primary findings in my doctoral research, discussing the topic that I did not explore in this study and offering recommendations for future research.

1.9 Field Campaigns

Throughout my doctoral research, I engaged in multiple field campaigns. Time constraints prevented the incorporation of data and results from these campaigns into my thesis, except for chapter 4. Below, I list and briefly outline the purposes of these field campaigns.

Antarctica

Ekström Ice Shelf (November 2021 - January 2022)

Figure 1.5: SLEDGE collecting quad-polarimetric pRES data at Ekström Ice Shelf.

As a member of the ReMeltRadar team, I conducted the collection of quad-polarimetric pRES data using three distinct approaches. The first set of data involved gathering measurements at various points with a 5 km spacing along the flow line spanning over 100 km across the ice shelf. Additionally, several short profiles were taken across the flow line. The primary objective of these measurements was intended to assess basal melt rate, vertical strain rate and the spatial and temporal change in ice fabric properties in the ice shelf by repeating these measurements one year later. The second set of data involved burying a pRES system with 4 antennas (quad-polarimetric mode) at the grounding line of the Ekström ice shelf for a year in unattended

measurements mode. Measurements were taken at 4-hour intervals to detect basal melt rate, vertical strain rate, and changes in ice fabric properties over the course of the year. Lastly, a proof of concept was achieved by collecting data using the developed autonomous rover system in quad-polarimetric mode (SLEDGE), as detailed in Chapter 4. This thesis showcases the development of the autonomous rover and presents a demonstration of the collected data from this field campaign.

Ekström Ice Shelf (December 2022 - March 2023)

In this field campaign, I undertook the task of conducting repeat measurements at all previously surveyed pRES points from the preceding year. My responsibilities extended to the maintenance and recovering the collected data of the buried ApRES unit located at the grounding line.

The Alps

Hintereisferner glacier - Austria (May 2021)

Figure 1.6: pRES measurement - Hintereisferner glacier.

During the field campaign, my responsibility involved gathering quad-polarimetric pRES data to analyze ice fabric properties in a temperate glacier. Despite facing challenges due to the intricate behavior of ice fabric in the recorded signal, I observed that the individual pRES radar signal, irrespective of polarization, struggled to identify the glacier's base due to significant signal attenuation in the temperate glacier. However, I identified a potential solution: utilizing the phase coherent quad-polarimetric signal might enable the detection of the glacier's base.

Hintereisferner glacier - Austria (April 2022)

Last year's results from this glacier showed potential to develop a method for detecting the base of a temperate glacier using phase coherence radar. On this occasion, we collected not

only a quad-polarimetric pRES profile along the flow line but also a reflection seismic profile to serve as a reference for identifying the glacier's base. This thesis does not include any results or findings related to this topic. However, it was presented in an EGU talk (Ershadi et al., 2022a, EGU abstract) as a work in progress.

Colle Gnifetti glacier - Switzerland/Italy (September 2021)

Figure 1.7: pRES measurement at Colle Gnifetti glacier.

In this field campaign, my primary responsibility was to collect quad-polarimetric pRES data. The objectives were twofold: firstly, to examine the ice fabric anisotropy in the accumulation zone of this glacier, and secondly, to compare it with the ice fabric anisotropy in the ablation zone of the Hintereisferner glacier. However, this was not the main objective of this field campaign. Conventional radar measurements in this region previously faced challenges in clearly detecting the internal reflection horizons (IRHs) within the deeper sections of the glacier. These horizons hold crucial data about historical glacier surfaces, providing insights into past accumulation, ice deformation, and facilitating the correlation of ice core chronologies. The primary goal of this study was to utilize phase-coherent radar data and obtain high spatial resolution pRES data through the use of two antennas. The objective was to employ Synthetic Aperture Radar (SAR) processing to reveal the deeper layers of the glacier. This work led by Falk Oraschewski is submitted for publication in The Cryosphere Journal.

1.10 Spinoff Contributions

The research conducted during my doctoral studies has provided me the opportunity to participate in several spinoff contributions including:

- **Zeising et al. (2023)** where I contributed to processing the pRES radar data. This study diverges from the coherence inverses approach, instead utilizing a cross-correlation of co-polarized measurements to accurately determine travel-time differences caused by dielectric anisotropy. Unlike previous methods, the polarimetric cross-correlation approach

enables the analysis of significant horizontal fabric asymmetries at greater depths. The notable alignment between the vertical profile of horizontal fabric asymmetry, derived from the analyses of multiple polarimetric pRES measurements, and the fabric measured in the EastGRIP ice core underscores the robustness and precision of this method.

- **Gerber et al. (2023)** where I simulated the radar beat frequency modulation for different degree of ice fabric anisotropy. This work involved integrating airborne and ground-based radar data with ice core and ice flow models. The findings of the study suggest that crystal orientation fabric anisotropy is a contributing factor to directional hardening in ice streams.

- **Lilien et al. (2023)** where I provided inverse results from the pRES radar at Dome C and participated in interpreting the model-observation comparison. The work incorporates a fabric evolution model into a large-scale ice-flow model capable of including lattice rotation, rotation recrystallization, and migration recrystallization. These three processes are considered crucial for fabric development, coupling the fabric to ice flow through a rheology with fewer approximations than previous models. The resulting model simulated ice flow and fabric development on a transect across Dome C, East Antarctica.

- **Oraschewski et al. (2023)** where I was part of the field team and tasked to collect quad-polarimetric pRES data. I also developed a "start-stop" algorithm for the pRES measurements using RTK GPS to trigger the radar every 10 cm. The research aimed to identify internal reflection horizons (IRHs) in the deeper sections of the accumulation zone of Colle Gnifetti glacier. This process provides insights into past accumulation, ice deformation, and aids in correlating ice core chronologies. The approach involved using high spatial resolution (10 cm) pRES data and applying Synthetic Aperture Radar (SAR) processing techniques.

Chapter 2

Polarimetric Radar Reveals the Spatial Distribution of Ice Fabric at Domes and Divides in East Antarctica

M. Reza Ershadi[1], Reinhard Drews[1], Carlos Martín[2], Olaf Eisen[3,5], Catherine Ritz[4], Hugh Corr[2], Julia Christmann[3,6], Ole Zeising[3,5], Angelika Humbert[3,5], Robert Mulvaney[2]

[1] Department of Geosciences University of Tübingen, Tübingen, Germany. [2] British Antarctic Survey, Natural Environment Research Council, Cambridge, UK [3] Alfred Wegener Institute Helmholtz-Centre for Polar- and Marine Research, Bremerhaven, Germany [4] University Grenoble Alpes, CNRS, IRD, IGE, Grenoble, France [5] Department of Geosciences, University of Bremen, Bremen, Germany [6] Institute of Applied Mechanics, University of Kaiserslautern, Germany

Published in *The Cryosphere Journal*
https://doi.org/10.5194/tc-16-1719-2022

Author Contribution

First author:
Scientific ideas: 70%, Data generation: 30%,
Analysis & interpretations: 75%, Paper writing: 60%

M. Reza Ershadi lead the code development and writing of the manuscript. Reinhard Drews, Carlos Martín, and Olaf Eisen designed the study outline. Robert Mulvaney, Catherine Ritz, Hugh Corr led the quad-polarimetric acquisition scheme and data collection at Dome C. Julia Christmann, Ole Zeising, and Angelika Humbert lead data acquisition at EDML. All authors contributed to the writing of the final manuscript.

Abstract

Ice crystals are mechanically and dielectrically anisotropic. They progressively align under cumulative deformation, forming an ice-crystal-orientation fabric that, in turn, impacts ice deformation. However, almost all the observations of ice fabric are from ice core analysis, and its influence on the ice flow is unclear. Here, we present a non-linear inverse approach to process co- and cross-polarized phasesensitive radar data.We estimate the continuous depth profile of georeferenced ice fabric orientation along with the reflection ratio and horizontal anisotropy of the ice column. Our method approximates the complete second-order orientation tensor and all the ice fabric eigenvalues. As a result, we infer the vertical ice fabric anisotropy, which is an essential factor to better understand ice deformation using anisotropic ice flow models. The approach is validated at two Antarctic ice core sites (EPICA (European Project for Ice Coring in Antarctica) Dome C and EPICA Dronning Maud Land) in contrasting flow regimes. Spatial variability in ice fabric characteristics in the dome-to-flank transition near Dome C is quantified with 20 more sites located along with a 36 km long cross-section. Local horizontal anisotropy increases under the dome summit and decreases away from the dome summit. We suggest that this is a consequence of the nonlinear rheology of ice, also known as the Raymond effect. On larger spatial scales, horizontal anisotropy increases with increasing distance from the dome. At most of the sites, the main driver of ice fabric evolution is vertical compression, yet our data show that the horizontal distribution of the ice fabric is consistent with the present horizontal flow. This method uses polarimetric-radar data, which are suitable for profiling radar applications and are able to constrain ice fabric distribution on a spatial scale comparable to ice flow observations and models.

2.1 Introduction

The movement of glaciers and ice sheets has two components: ice deformation and basal sliding. Satellites provide widespread and increasingly well-resolved temporal surface velocities. In most cases, however, it is difficult to differentiate the contribution of ice deformation and basal sliding. This results in increased uncertainty in several areas, such as ice flow model initialization with data assimilation techniques (Schannwell et al., 2019) or predicting erosion rates from surface velocities (Headley et al., 2012; Cook et al., 2020). Even in ice-sheet-covered areas where basal sliding can certainly be excluded, e.g., near ice domes or beneath ice rises (Matsuoka et al., 2015), knowledge of internal ice deformation is important for predicting age–depth relationships for new ice core drill sites (Parrenin et al., 2007; Martín et al., 2009a; Martín and Gudmundsson, 2012) or for using internal layer architecture to reconstruct paleo-ice dynamics (Matsuoka et al., 2015). The temperature-dependent, non-linear, and anisotropic rheology of ice governs how ice deforms and poses many challenges to numerical ice flow models. Most models do not consider ice fabric anisotropy because this quantity is currently poorly constrained by observations. The most reliable observations of ice fabric come from the analysis of thin ice core sections using ice fabric analyzers detecting single ice crystals' lattice orientation using transmitted light microscopy (Durand et al., 2009; Weikusat et al., 2017). The underlying principle used is that single ice crystals are uniaxially birefringent for electromagnetic waves. This causes the polarization-dependent formation of ordinary and extraordinary waves that propagate through the lattice and superimpose with a phase shift at the detector. Constructive and destructive superposition of these waves can be used to characterize ice fabric in thin sections at

a vertical spacing of centimeters to decimeters (Kerch et al., 2020). Ice-penetrating radar on ice sheets employs a similar principle to optical methods but slightly different because it is based on measuring a bulk anisotropy rather than an intrinsic. In comparison, the dielectric anisotropy of ice observed by radar is a combined effect of the ice crystal birefringence and crystal-orientation fabric with different spatial scales and applied electromagnetic frequencies. As is explained in more detail below (Sect. 2.3.3), ground-penetrating radar systems such as the ground-based autonomous phase-sensitive radio echo sounder (ApRES) (Brennan et al., 2014; Nicholls et al., 2015) can detect the polarization-dependent phase shift induced by ice birefringence and also quantify the degree of anisotropic scattering which may be caused by abrupt vertical changes in ice fabric. Other geophysical methods to detect ice fabric anisotropy are sonic logging of boreholes (Gusmeroli et al., 2012; Pettit et al., 2007) or surface-based seismic surveys (Diez and Eisen, 2015; Diez et al., 2015; Smith et al., 2017; Brisbourne et al., 2019).

Ice-core- and borehole-based methods are reliable and can be obtained in a high vertical resolution (sub-centimeter scale). However, in deep ice, where grains may be large compared with the typical ice core diameter of 10 cm, they are statistically not well constrained. They also do not provide much spatial context and are often obtained at dome locations where the horizontal advection is negligible, and the climate record is easier to interpret. The surface seismic methods are more challenging in terms of field logistics, but they inherently provide wide-angle information, which radar typically does not. The majority of radar profiles are not analyzed with respect to ice fabric anisotropy often because the radar systems do not provide the required precision or are collected with a single polarization only. The collection of crossing radar lines partially remedies this issue. However, newer radar systems collect data with cross-polarized arrays so that area-wide detection of ice anisotropy appears to be a target within reach (Yan et al., 2020). The theory of radar birefringence in glaciology has long been known (Hargreaves, 1978; Woodruff and Doake, 1979; Matsuoka et al., 1997; Fujita et al., 1999) and has recently been significantly extended to exploit the capacity of phase information from newer radar systems that were previously not available (Dall, 2010; Jordan et al., 2019, 2020). Examples for applications of radar polarimetry exist near ice domes in Greenland (Gillet-Chaulet et al., 2011; Li et al., 2018; Jordan et al., 2019) and Antarctica (Fujita et al., 1999; Brisbourne et al., 2019), on ice rises (Drews et al., 2015a; Matsuoka et al., 2015; Brisbourne et al., 2019), in flank-flow regimes (Eisen et al., 2007), in divides (Young et al., 2021), and for ice streams (Jordan et al., 2020). However, there is not yet a clear observation-based picture of how ice fabric develops across the different flow regimes.

Here, we built on a previously derived forward modeling framework (Fujita et al., 2006) that can model polarimetric backscattered signal as a function of vertical distribution of ice fabric, extended by (Jordan et al., 2019, 2020). We develop it further with theory relating to anisotropic reflections and then develop an inverse approach that also attempts to characterize ice fabric types continuously along depth and for all of the three bulk crystallographic axes. The technical developments will allow the ice fabric orientation to be automatically georeferenced and its full variability with depth to be reconstructed. But the major achievement in this method is to estimate the depth variability in the horizontal ice fabric anisotropy along with reflection ratio, which allows all the possible eigenvalues of the ice fabric to be estimated. This leads to quantifying the ice fabric type and its vertical anisotropy. We demonstrate this for 21 ApRES measurements conducted near two ice core drill sites drilled by the European Project for Ice Coring in Antarctica (EPICA). Of the radar measurements, 20 cover the dome–flank transition at the EPICA ice core site in Dome C (EDC) and one additional measurement at the EPICA ice core site in the eastern Dronning Maud Land (EDML). The successful validation with ice

core data suggests that polarimetric radar is now capable of providing all directional constraints required for parameterization of an anisotropic flow law.

Table 2.1: Important variables sorted in order of appearance.

Symbol	Unit	Description
$\mathbf{v_1}, \mathbf{v_2}, \mathbf{v_3}$	-	Ice fabric eigenvector
$\lambda_1, \lambda_2, \lambda_3$	-	Ice fabric eigenvalue
ε'	-	Principal Dielectric Tensor
$\mathbf{E}$	-	Electric field vector
H, V	-	Horizontal and Vertical polarization plane
TR	-	Tx-Rx aerial line
θ	$^\circ$	Ice fabric orientation
α	$^\circ$	Georeferencing angle
z	m	Depth (0 at the surface, positive downward)
i	-	Stratified ice layer index
N	-	Number of layers
$\mathbf{T}$	-	Transmission matrix
k_x, k_y	$rad\, m^{-1}$	Wavenumbers along the two principal axes
$\mathbf{\Gamma}$	-	Reflection matrix
$\mathbf{S}$	-	Scattering matrix
s_{HH}, s_{VV}	-	Complex co-polarized scattering signals
s_{HV}, s_{VH}	-	Complex cross-polarized scattering signals
$\mathbf{R}$	-	Rotation matrix
r	-	Reflection ratio
$\Delta\lambda$	-	Ice fabric horizontal anisotropy
C_{HHVV}	-	Complex polarimetric coherence
ϕ_{HHVV}	rad	Polarimetric coherence phase
Ψ	-	Scaled phase derivative
P	dB	Power anomaly
n	-	Number of angular increments
AD	$^\circ$	Nodes angular distance
J	-	Cost function

2.2 Study Areas

We use radar data near two deep ice core drill sites in East Antarctica. One is located at Dronning Maud Land (DML), near the German summer station (Kohnen at -75.00° S , 0.00°). The other site is located at Dome C, close to Concordia station (-75.10° S, 123.35° E). We use the measured ice fabric data from both ice cores published by Weikusat et al. (2017) and Durand et al. (2009), respectively, to validate our polarimetric-radar data inferences. At Dome C, radar data were additionally collected at 20 stations along with a 36 km long profile across the dome, enabling us to track ice fabric variability in the dome–flank transition zone. Surface topography at Dome C (Helm et al., 2014; Howat et al., 2019) exhibits an ice dome elongated in the SW–NE direction (Fig. 2.1a). Surface velocities are too slow ($<$0.02 $\mathrm{m\ a^{-1}}$) for reliable detection with satellite

imagery. GPS measurements show that the ice flow direction follows the surface maximum gradient direction, increases with distance from the dome, and is near-parallel to the transect described above (Vittuari et al., 2004). The Kohnen station (Fig. 2.1b) is located near a transient ice-divide triple junction in a flank-flow regime, and the ice flow is significantly faster (≈ 0.74 m a^{-1}) than at Dome C. The largest principal strain rate at Dome C and EDML is oriented SW–NE (Rémy and Tabacco, 2000; Vittuari et al., 2004) and 24° N (Wesche et al., 2007; Drews et al., 2012), respectively.

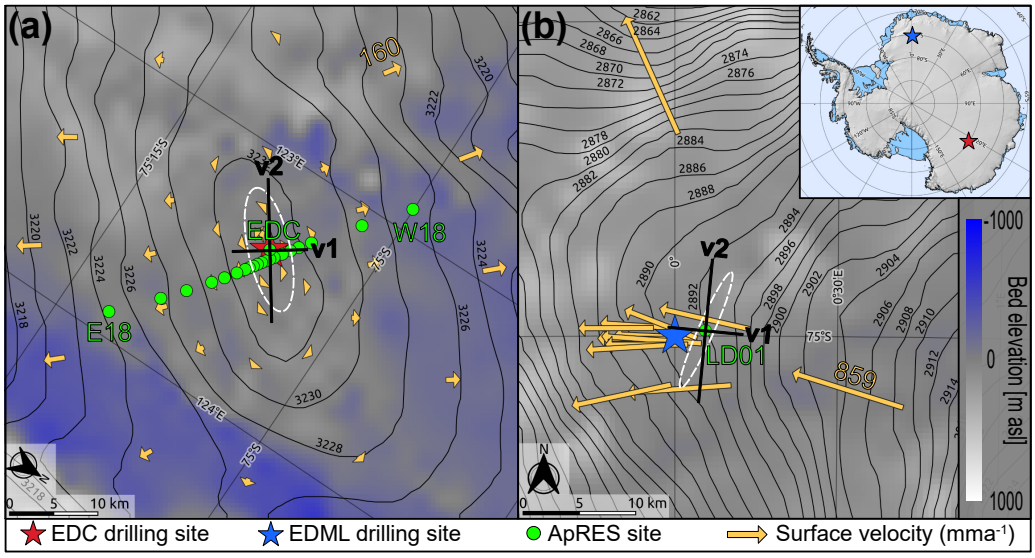

Figure 2.1: Map of the study areas. (a) EPICA Dome C (EDC). (b) EPICA Dronning Maud Land (EDML). Black contour lines are the surface elevation (Helm et al., 2014). The background color is the bed elevation (Morlighem et al., 2020). Yellow arrows are the magnitude and direction of the surface velocities at EDC (Vittuari et al., 2004) and EDML (Wesche et al., 2007). The white strain ellipses mark the directions of the maximum and minimum strain rate. The ice fabric's horizontal eigenvectors are represented by **v1** and **v1**, and they are based on the results in Sect. 2.4.1 and 2.4.2. Note that (a) and (b) have a different scale and orientation.

2.3 Methods

2.3.1 Quantitative Metrics Used to Define the Ice Fabric

Ice crystallizes in the shape of hexagons, and the direction normal to the basal plane is described with the c axis (Hooke, 2005). Ice crystals are strongly anisotropic and 60 times softer along the basal plane than perpendicular to it (Duval et al., 1983; Smith et al., 2017). In a given strain regime, individual ice crystals deform preferentially along the basal plane and orient themselves so that the bulk c-axis orientation forms a distinct pattern, which we refer to as ice fabric. Elsewhere it is also described as crystal-orientation fabric (COF) or lattice-preferred orientation (LPO) (Weikusat et al., 2017). The radio waves are sensitive to the dielectric anisotropy, which

follows the mechanical anisotropy described by the second-order orientation tensor (Gödert, 2003; Gillet-Chaulet et al., 2006; Martín et al., 2009a). The bulk ice fabric pattern is described with a second-order orientation tensor (we refer to this as orientation tensor) using the eigenvectors (**v1**, **v2**, and **v3**) and eigenvalues ($\lambda1$, $\lambda2$, and $\lambda3$) of an ellipsoid that best represents the average c-axis orientation of all ice crystals in the sample. The eigenvalues are normalized

$$\lambda1 + \lambda2 + \lambda3 = 1, \tag{2.1}$$

and to be consistent with the past polarimetric radar studies, we assume

$$\lambda1 < \lambda2 < \lambda3. \tag{2.2}$$

Combination of Eqs. (2.1) and (2.2) set bounds on the eigenvalues ($0 \leq \lambda1 \leq 0.33$, $0 \leq \lambda2 \leq 0.5$, and $0.33 \leq \lambda3 \leq 1$). The eigenvalues can be used to distinguish the ice fabric types such as isotropic ($\lambda1 \approx \lambda2 \approx \lambda3$), girdle ($\lambda1 \ll \lambda2 \approx \lambda3$), and single maximum ($\lambda1 \approx \lambda2 \ll \lambda3$) (Woodcock, 1977; Azuma, 1994; Fujita et al., 2006). The eigenvalues and eigenvectors can be used to describe the dielectric permittivity tensor ε', containing the bulk permittivities ϵ'_x, ϵ'_y, and ϵ'_z relevant for radio wave propagation (Sect. 2.3.3).

2.3.2 Data Collection

The radar data in this study were collected using a phase-sensitive frequency-modulated continuous-wave radar system (Brennan et al., 2014; Nicholls et al., 2015) with a 200 MHz bandwidth and $f_c = 300$ MHz center frequency. This radar emits linearly polarized electromagnetic waves using a slot antenna where the direction of the polarization plane is aligned with the direction of the electric field vector (**E**) in the antenna as shown in Fig. 2.2a.

We use terminology from satellite radar polarimetry to dis- tinguish the directions of the polarization with H and V, al- though, in a nadir-looking geometry, these are arbitrarily determined because H and V both have horizontal polarization plane at depth. Here, we name the horizontal (H) and vertical (V) polarization plane consistent with Jordan et al. (2019). However, we want to point out that this definition is different to the one applicable to seismic shear waves, where vertical receivers have a vertical component upon reflection at depth for non-vertical angles of incidence, and vice versa. The model coordinate system is shown in Fig. 2.2c. The aerial line (TR) connects transmitter (Tx) and receiver (Rx), and by convention, we assume that H is parallel to TR; **v1** and **v2** are the horizontal eigenvectors which align with the direction of the smallest (ϵ'_x) and largest (ϵ'_y) horizontal principal permittivity, respectively (Fujita et al., 2006; Jordan et al., 2019). Hence, $\theta = 0°$ if H is aligned with **v1**. The angle α is measured by compass with $\pm 15°$ uncertainty for georeferencing the data. Here, we use polar stereographic coordinates, where counterclockwise rotation is positive.

Radar data at all the sites were collected at a fixed α, obtained from different antenna orientation in co-polarization (HH, VV) and cross-polarization (HV, VH) configurations (Hargreaves, 1977; Fujita et al., 2006) as shown in Fig. 2.2b. We refer to these measurements as quad-polarimetric measurement. Radar data at Dome C were collected at 20 sites in January 2014. One of the sites is located within walking distance of the ice core site EDC. The remaining 19 sites (termed E(ast)0-E18, and W(est)0.5-W18, with the numbers relating to the distance in kilometers away from the dome) are aligned in a profile which is approximately perpendicular to the long axis of the dome and parallel to the flowline (Fig. 2.1a). At EDML, data were collected in January 2017, approximately 2.7 km northeast of the ice core site EDML (Fig. 2.1b). More information related to the individual ApRES sites is shown in Appendix 6.1.

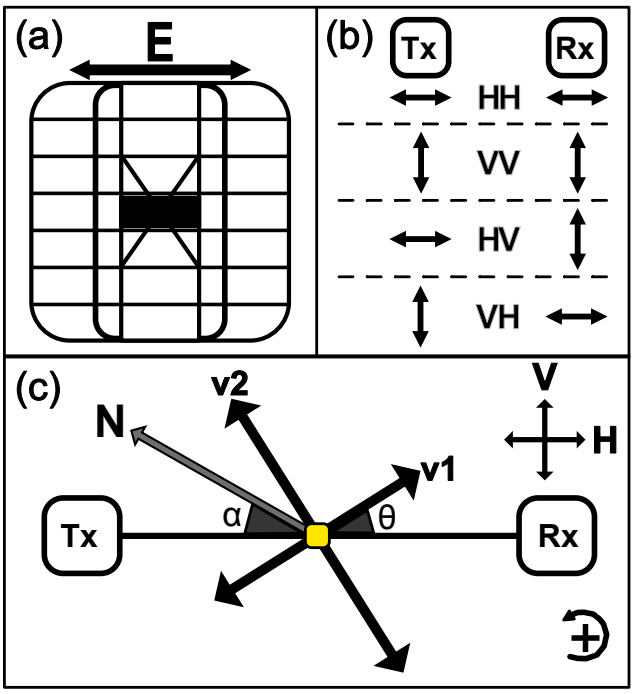

Figure 2.2: (a) Bird's-eye view of the ApRES slot antenna with the direction of the electric field vector (**E**). (b) The terminology of the co-and cross-polarized ApRES measurements defined using **E**. The direction of wave propagation is into the page (⊗). (c) The model coordinate system where transmitting (Tx) and receiving (Rx) antennas are connected with the aerial line (TR). The horizontal (H) and vertical (V) polarization planes are defined so that H is parallel to TR. The directions of the ice fabric horizontal principal axes are represented by **v1** and **v2**. θ is the angle between H and **v1**, and α is used for georeferencing.

2.3.3 Background of Radar Polarimetry

Radio signal propagation through ice sheets is polarizationdependent because of the dielectric anisotropy of the ice fabric. If the direction of **v3** is vertical, and the remaining two eigenvectors (**v1**, **v2**) are in the horizontal plane, then the relation between the depth profile of the dielectric permittivity tensor and the orientation tensor is given by Fujita et al. (2006):

$$\varepsilon'(z) = \begin{pmatrix} \epsilon'_x & 0 & 0 \\ 0 & \epsilon'_y & 0 \\ 0 & 0 & \epsilon'_z \end{pmatrix} = \begin{pmatrix} \epsilon'_\perp + \Delta\epsilon'\lambda 1 & 0 & 0 \\ 0 & \epsilon'_\perp + \Delta\epsilon'\lambda 2 & 0 \\ 0 & 0 & \epsilon'_\perp + \Delta\epsilon'\lambda 3 \end{pmatrix}. \tag{2.3}$$

For the dielectric permittivity at radio frequencies perpendicular to c axes, we use $\epsilon'_\perp = 3.15$ (Fujita et al., 2000), which is slightly lower than the value found by Bohleber et al. (2012). The value of a dielectric anisotropy for a single crystal is set to $\Delta\epsilon' \approx 0.034$ (Matsuoka et al., 1997). The vertical **v3** assumption in this study is justified through measurements at the EDC ice core, where the direction of **v3** varies only by about 5° around the vertical (Durand, Svensson, Persson, Gagliardini, Gillet-Chaulet, Sjolte, Montagnat, and Dahl-Jensen, 2009). Elsewhere in ice sheets, this may not be the case, which will cause an additional source of horizontal birefrin-

gence (Matsuoka, Wilen, Hurley, and Raymond, 2009; Jordan, Schroeder, Castelletti, Li, and Dall, 2019).

We model radio wave propagation through birefringent ice using the method developed by Fujita et al. (2006). It includes transmission and reflection of initially linearly polarized waves emitted with two polarization modes (H and V, with direction defined in the previous section). If z is the depth from the surface (positive downward), it assumes stratified ice with $i = 1,\ldots N$ layers predicting the radar response as a function of the emitted polarization plane and ice fabric parameters. Radar transmission ($\mathbf{T}$) and reflection ($\mathbf{\Gamma}$) are represented by 2×2 matrices only because radar signal propagation is insensitive to the vertically directed $\mathbf{v3}$. The transmitted radar wave $\mathbf{E}_T$ and the corresponding radar reflection $\mathbf{E}_R$ are 2×1 vectors, with each component containing the electric field information of the H and V polarization components, respectively (Doake et al., 2003). Because only relative phase and amplitude variations are considered, all information about the radio wave transmission and reflection can be inferred from the scattering matrix ($\mathbf{S}$) at layer N:

$$\mathbf{E}_R = \mathbf{S}_N\mathbf{E}_T, \tag{2.4}$$

containing the complex scattering unit

$$\mathbf{S}_N = \begin{pmatrix} s_{HH} & s_{VH} \\ s_{HV} & s_{VV} \end{pmatrix}_N =$$

$$D^2(z_N)\prod_{i=1}^{N}[\mathbf{R}(\theta_{N+1-i})\mathbf{T}_{N+1-i}\mathbf{R}'(\theta_{N+1-i})]\mathbf{R}(\theta_i)\mathbf{\Gamma}_i\mathbf{R}'(\theta_i)\prod_{i=1}^{N}[\mathbf{R}(\theta_i)\mathbf{T}_i\mathbf{R}'(\theta_i)], \tag{2.5}$$

where D and $\mathbf{R}$ are the depth factor and rotation matrix, respectively. The four elements of the scattering matrix are described as co-polarized scattering signals (s_{HH} and s_{VV}) and cross-polarized scattering signals (s_{HV} and s_{VH}).

To consider the polarization dependence of the reflection boundary, we formed the reflection ratio

$$r = \frac{\Gamma_y}{\Gamma_x}, \tag{2.6}$$

where Γ_x and Γ_y are the elements of the reflection matrix $\mathbf{\Gamma}$ known as complex amplitude reflection coefficients (Ackley and Keliher, 1979; Ulaby and Elachi, 1990; Fujita, Matsuoka, Ishida, Matsuoka, and Mae, 2000; Fujita, Maeno, and Matsuoka, 2006) . Here we only use the real part of Γ_x and Γ_y. Therefore, r is a scalar quantity. Further details about the radar forward model implementation and definition of all the parameters in Eq. (2.3.3) are described in Appendix 6.2 and Fujita et al. (2006).

The parameters of interest that we aim to infer from the radar observations for each layer are the horizontal anisotropy $\Delta\lambda = \lambda2 - \lambda1$, the ice fabric orientation angle θ, and the reflection ratio r. All of these quantities may vary with depth. Much information is gained by interpreting the coherence phase difference between s_{HH} and s_{VV}, which is a crucial development in the works from Dall (2010), extended by Jordan et al. (2019). The coherence phase difference ϕ_{HHVV} is the argument of the complex polarimetric coherence C_{HHVV}, estimated via a discrete approximation,

$$C_{HHVV} = \frac{\sum_{b=1}^{M} s_{HH,b}\cdot s^*_{VV,b}}{\sqrt{\sum_{b=1}^{M}|s_{HH,b}|^2}\sqrt{\sum_{b=1}^{M}|s_{VV,b}|^2}}, \tag{2.7}$$

with * as complex conjugate,

$$\phi_{HHVV} = \arg\left(C_{HHVV}\right), \tag{2.8}$$

where$M$ is the number of range bins used for vertical aver- aging, and b is the summation index. The depth gradient of ϕ_{HHVV} provides a way to relate the local phase gradient to $\Delta\lambda$ at the direction of the horizontal principal axes (Jordan et al., 2019, 2020)

$$\Psi = \frac{2c\sqrt{\epsilon'}}{4\pi f_c \Delta\epsilon'} \frac{d\phi_{HHVV}}{dz}, \tag{2.9}$$

with

$$\Delta\lambda(z) = \Psi(z, \theta = 0°, 90°). \tag{2.10}$$

The coherence magnitude $0 < |C_{HHVV}| < 1$ also tracks phase errors so that unreliable regions with ϕ_{HHVV} can be avoided (Jordan et al., 2019, 2020). Therefore, we restrict the analysis to the top 2000 m, where typically $|C_{HHVV}| > 0.4$.

The ApRES stores the deramped signal (Brennan et al., 2014; Jordan et al., 2020), which is not represented in Eqs. (2.7) and (2.8). The deramping corresponds to a complex conjugation of C_{HHVV} (Jordan et al., 2020). Therefore, we use Eq. (2.7) for the models and the conjugate of Eq. (2.7) for the radar data to calculate the coherence phase. We simplified Eq. (2.3.3) to a single-layer case (Appendix 6.3), showing that the polarity of Ψ can differentiate the direction of **v1** and **v2** (Appendix 6.4). If the coherence phase is based on the received signal, **v2** is in the direction of $\Psi > 0$ (i.e., TR $\parallel$ **v2**), and **v1** is in the direction of $\Psi < 0$ (i.e., TR $\parallel$ **v1**). When using observations, the depth gradient calculation of ϕ_{HHVV} is inherently difficult because any differencing scheme amplifies noise (Chartrand, 2011). We follow Jordan et al. (2019) and apply a 1D convolutional derivative on both real and imaginary components of the complex coherence, which also avoids phase unwrapping.

In Appendix 6.5, we show that the quad-polarimetric measurement (Fig. 2.2c) can be used to synthesize the full radar return from any antenna orientation using a matrix transformation

$$\mathbf{S}_N(\theta \pm \gamma) = \mathbf{R}(\theta \pm \gamma)\mathbf{S}_N(\theta)\mathbf{R}'(\theta \pm \gamma), \tag{2.11}$$

where γ is the angular offset from θ. Equation (2.11) is the mathematical equivalent to rotating the antennas in the field for each polarimetric configuration. As demonstrated in Fig. 6.1, we find no significant differences between the synthesized and the full azimuthal rotation dataset with $22.5°$ increments.

2.3.4 Demonstration of Anisotropic Signatures in Radar Data Using a Synthetic Model

For a given depth profile of $\Delta\lambda(z)$, $\theta(z)$, and $r(z)$, the radar return can be simulated using the forward model described by Eqs. (2.4)-(2.3.3). We show a seven-layer synthetic model in Fig. 2.3 to visualize features in the radar data, which can be linked to ice fabric parameters. The model parameters used to generate Fig. 2.3 are shown in Table 2.2. Power anomalies illustrate the effects of anisotropic ice

$$\delta P_{xx}(\theta, z) = 20\log_{10}\left(\frac{|s_{xx}(\theta, z)|}{\frac{1}{n}\sum_{b=1}^{n}|s_{xx}(\theta_b, z)|}\right) \quad \text{for xx = HH, VV, HV, VH,} \tag{2.12}$$

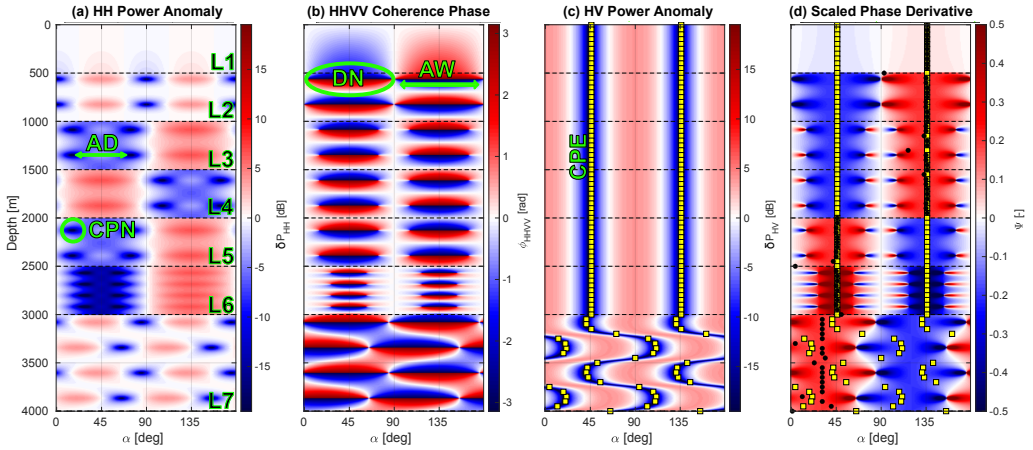

Figure 2.3: A seven-layer synthetic model generated by Eq. (2.3.3) using the model parameters in Table 2.2. Horizontal dashed black lines are the layer boundaries with layer numbers from L1 to L7. (a) HH power anomaly (δP_{HH}) representing co-polarization node (CPN) and node angular distance (AD). (b) HHVV coherence phase (ϕ_{HHVV}) displaying dipole co-polarized node (DN) and node angular width (AW). (c) HV power anomaly (δP_{HV}) representing cross-polarization extinction (CPE). (d) Scaled phase gradient (9) displaying the direction of **v1** (yellow squares in blue areas) and **v2** (yellow squares in red areas). The magnitude of Ψ at the black dots is the value of horizontal anisotropy ($\Delta\lambda$).

where $|s_{xx}|$ is the amplitude of the complex received signal, and n is number of angular increments for θ. In δP_{HH}. In δP_{HH}, a number of co-polarization nodes (CPNs) occur, which result from destructive superposition of ordinary and extraordinary waves (Fig. 2.3a). The number of nodes per layer is only a function of ice fabric anisotropy in that layer, with higher horizontal anisotropy resulting in more nodes. The nodes occur at a variable angular distance (termed AD in Fig. 2.3a) if anisotropic reflection is relevant (e.g., L2 and L3 in Fig. 2.3a). The angular dependency of the co-polarization nodes on anisotropic scattering can be identified using a depth-invariant ice fabric orientation (constant θ). Previously, Fujita et al. (2006) approximated the correlation between AD and r with a linear regression. As detailed in Appendix 6.6 we improved this by finding the analytical solution

$$r = \frac{1}{\tan^2(\frac{AD}{2})}. \tag{2.13}$$

Differences in both approaches are illustrated in Fig. 2.4. Two important features in δP_{HH} are therefore the frequency of occurrence of co-polarization nodes with depth (a first-order proxy for the horizontal anisotropy) and their angular distance (a mixed proxy for anisotropic reflections or depthvariable ice fabric orientation). δP_{HH} can be $90°$ (e.g., L2) or $180°$ (e.g., L3) symmetric if $r_{dB} = 0$ or $r_{dB} \neq 0$, respectively. In a depth-invariant ice fabric orientation, the minima in δP_{HV} align with **v1** and **v2**, termed cross-polarization extinction (CPE in Fig. 2.3c). Using the radar forward model, this can be derived analytically for a single-layer case as

$$\delta P_{HV}(\theta, z) = 20 \log_{10} \left(\frac{\sin(\theta, z)\cos(\theta, z)}{\frac{1}{n}\sum_{b=1}^{n} \sin(\theta_b, z)\cos(\theta_b, z)} \right), \tag{2.14}$$

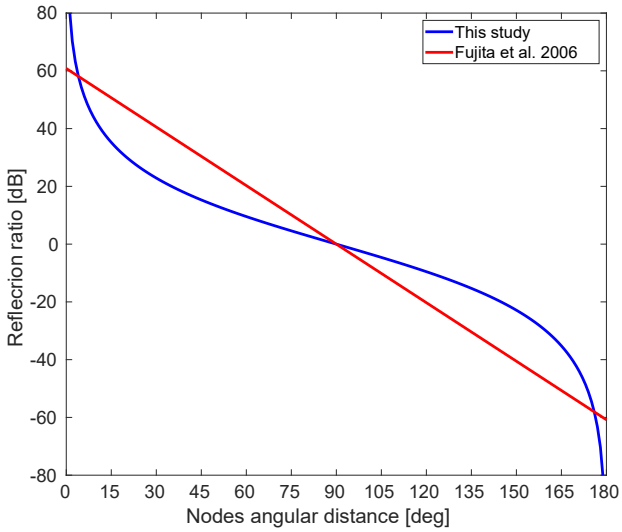

Figure 2.4: Dependence of reflection ratio on the azimuthal difference between two nodes as determined by Fujita et al. (2006) and through Eq. 2.13.

where the solutions are at $\theta = 0°$ and $\pm 90°$. In multi-layer cases, where θ changes with depth (e.g., L6 and L7 in Fig. 2.3b), δP_{HV} also depends on other parameters, making it difficult to infer θ using δP_{HV} alone.

The co-polarization nodes in δP_{HH} can also be observed in ϕ_{HHVV} (termed DN in Fig. 2.3b). The depth of the node can be automatically estimated at the zero-phase transition. Unlike δP_{HH}, the nodes in ϕ_{HHVV} are $90°$ anti-symmetric, and their polarity is insensitive to r. This can be used to determine the directions of **v1** and **v2**. The angular width of the nodes (termed AW in Fig. 2.3b) decreases when $r_{dB} \neq 0$ (e.g., L3 or L4). The absolute value of Ψ at the principal axis's directions (**v1** or **v2**) is a first-order proxy for $\Delta\lambda$ at a given depth (Eq. 2.10, Fig. 2.3d). Since the scaled phase gradient (Fig. 2.3d) is anti-symmetric, and only the positive gradient is in the direction of **v2**, we mask negative parts of Ψ from now on.

Table 2.2: The model parameters used to generate Fig. 2.3. In Eq. (2.3.3), components of $\mathbf{T}$ are calculated from $\Delta\lambda$ assuming $\epsilon'_x = 3.15$, and components of $\mathbf{\Gamma}$ are calculated from r assuming $\Gamma_x = 10^{-12}$. The vertical gridding of the model is 1 m.

Layer Name	Depth [m]	$\Delta\lambda$ [−]	r [dB]	θ [°]
L1	0-500	0.025	0	45
L2	500-1000	0.2	0	45
L3	1000-1500	0.2	10	45
L4	1500-2000	0.2	-10	45
L5	2000-2500	0.2	-10	135
L6	2500-3000	0.45	-20	135
L7	3000-4000	0.2	0	120

2.3.5 An Inverse Approach to Infer Ice Fabric from Quad-Polarimetric Returns

Fujita et al. (2006) focused on the power anomalies from co- and cross-polarized measurements (δP_{HH}, δP_{HV}). Dall (2010) and Jordan et al. (2019) included the coherence phase gradient (Ψ) to quantify the ice fabric horizontal anisotropy $\Delta\lambda$). However, particularly for multi-layer cases where the ice fabric parameters vary with depth, there has not yet been an established procedure for how ice fabric parameters can be reliably inverted from observations. Here, we use the previous work from Fujita et al. (2006), Dall (2010), and Jordan et al. (2019) and provide additional justification to infer all the ice fabric parameters in a continuous depth profile.

Our approach involves data preprocessing, initializing the model parameters, and parameter optimization using a constrained multivariable non-linear least-square inverse approach (Powell, 1983; Waltz et al., 2006). All the three eigenvalues are then estimated from the estimated $\Delta\lambda$ and optimized r using a top-to-bottom, layer-by-layer approach assuming isotropic ice at the surface.

Data Preprocessing

The full angular response is synthesized from HH, VV, and HV observations for a single TR orientation (θ) using Eq. (2.11) at 1° increments. The amount and method of smoothing applied to the data depend on nodes' vertical frequency and the phase polarity's sharpness. The power anomalies are smoothed by moving-average and 2D Gaussian convolution. The coherence phase (ϕ_{HHVV}) is inherently smoothed, depending on the size of the depth window in Eq. (2.7), while its gradient (Ψ) is smoothed with a 1D Gaussian convolution at each azimuth.

Model Parameterization

We investigate two parameterization types for the free model parameters (θ, $\Delta\lambda$, r) with depth: piecewise constant and a superposition of Legendre polynomials. The former has the highest number of free model parameters but can capture abrupt variability with depth. The latter has a reduced set of free model parameters with improved performance during the inversion but varies more smoothly with depth. At Dome C, no abrupt variability is visible in the data so that we use the Legendre polynomials with 40 free model parameters (30 for θ, and 10 for r). At EDML, because of abrupt depth variability in r and θ, we default to the piecewise constant parameterization, resulting in 80 free model parameters (40 piecewise constant intervals at 50 m spacings for r and θ).

Derivation of Initial Guess

The non-linear optimization problem depends on a welldefined initial guess based on our inferences from the synthetic data. Initial guesses of variables are marked with superscript 0. We first derive the initial guess for the orientation of the ice fabric $\theta^0(z)$ using the minima in δP_{HV}, polarity in ϕ_{HHVV}, and the sign of Ψ. We then infer $\Delta\lambda^0(z)$ using the absolute value of Ψ at the minima of δP_{HV}. The initial guess for $r^0_{dB}(z)$ is zero. The underlying assumption for all of the initial guesses is that θ does not vary significantly with depth.

Cost Function and Optimization

We optimize θ and r for all depth intervals, while at this stage we accept the estimated $\Delta\lambda^0$ for horizontal anisotropy. There are a number of possible model data misfit metrics of power anomalies and phase differences,

$$J_{\phi_{HHVV}} = ||\phi^{\text{obs.}}_{HHVV} - \phi^{\text{mod.}}_{HHVV}||^2, \tag{2.15}$$

$$J_{\delta P_{HH}} = ||\delta P^{\text{obs.}}_{HH} - \delta P^{\text{mod.}}_{HH}||^2, \tag{2.16}$$

$$J_{\delta P_{HV}} = ||\delta P^{\text{obs.}}_{HV} - \delta P^{\text{mod.}}_{HV}||^2, \tag{2.17}$$

and the total misfit between the observed (obs.) and the modeled data (mod.) is defined as

$$J_{total} = l_1(J_{\phi_{HHVV}}) + l_2(J_{\delta P_{HH}}) + l_3(J_{\delta P_{HV}}), \tag{2.18}$$

where l_1, l_2, and l_3 are constants (0 or 1). Note that ϕ and δP in Eqs. 2.15 to 2.17 are standardized. In Table 2.3, we show the values of l_1, l_2, and l_3 that we used for Dome C and EDML sites. The coherence phase misfit was not applicable in EDML due to strong ice fabric anisotropy. To further constrain the inversion, we set bounds on the model parameters so that $0 < \Delta\lambda_i < 0.5$, $0° < \theta_i < 180°$, and -30 dB $< r_i < 30$ dB. This is implemented in the cost function in the form of log-barrier functions using MATLAB's fmincon algorithm.

Table 2.3: The constant l_1, l_2, l_3 for ice fabric parameters θ and r at Dome C and EDML.

Site	θ	r
Dome C	1,0,0	0,1,0
EDML	0,1,0	0,1,0

2.3.6 Reconstruction of All Eigenvalues

Once the radar forward model is optimized, we attempt to reconstruct all the three eigenvalues in a top-to-bottom approach. We use an additional assumption for the standard scattering model where the reflection coefficient can be described using the Fresnel equations (Paren, 1981; Drews et al., 2012). If anisotropic scattering is caused by depthvariable ice fabric, then the reflection ratio at the interfaces i and $i+1$ can be approximated by

$$r_i = \pm\sqrt{\left(\frac{\lambda 2_i - \lambda 2_{i+1}}{\lambda 1_i - \lambda 1_{i+1}}\right)^2}. \tag{2.19}$$

Here, for the sake of simplicity, we only use the positive results for r. Solving Eq. 2.19 using the optimized r and $\Delta\lambda$ can fully reconstruct $\lambda 1$, $\lambda 2$, and $\lambda 3$ in a nadir geometry, which will resolve the ice fabric types' ambiguity, as explained in Appendix 6.7. At the surface, ice is assumed to be isotropic (an assumption that we discuss later in Sect. 2.5.1) so that $\lambda 1_1 \approx 0.33$, allowing $\lambda 2_1$ and $\lambda 3_1$ to be inferred from the estimated $\Delta\lambda_1$

$$\lambda 2_1 = \Delta\lambda_1 + \lambda 1_1, \tag{2.20}$$

$$\lambda 3_1 = 1 - \lambda 2_1 - \lambda 1_1. \tag{2.21}$$

The eigenvalues for the surface can be estimated by iterating through Eqs. (2.20) and (2.21) and decreasing the value of $\lambda 1_1$ by $1.0 \cdot 10^{-5}$ at each iteration until all the surface eigenvalues fulfill the requirements in Sect. 2.3.1. For deeper layers $i+1$, all three eigenvalues can be reconstructed analytically by solving

$$\lambda 1_{i+1} = \lambda 1_i - \left(\frac{\Delta\lambda_i - \Delta\lambda_{i+1}}{r_i - 1} \right) \tag{2.22}$$

for $\lambda 1_{i+1}$ and inferring $\lambda 2_{i+1}$ and $\lambda 3_{i+1}$ with

$$\lambda 2_{i+1} = \Delta\lambda_{i+1} + \lambda 1_{i+1}, \tag{2.23}$$

$$\lambda 3_{i+1} = 1 - \lambda 2_{i+1} - \lambda 1_{i+1}, \tag{2.24}$$

where Eq. (2.22) is a reformed version of Eq. (2.19). However, errors during the optimization may result in a reconstruction of the three eigenvalues, which do not comply with limits inferred in Sect. 2.3.1. In that case, $\Delta\lambda$ and r are varied in a systematic search to find eigenvalues within the permissible limits. Solutions, in this case, are not unique, and additional constraints on the vertical gradients are required. Here, we use the vertical gradient between the two largest adjacent eigenvalues, where $-5.0 \cdot 10^{-4} < \frac{\lambda 3_i - \lambda 3_{i+1}}{z_i - z_{i+1}} < 1.5 \cdot 10^{-3}$ and $|\frac{\lambda 3_i - \lambda 3_{i+1}}{z_i - z_{i+1}}| > 1.0 \cdot 10^{-6}$. This correction does not significantly alter the results from the previous section but assures that the inferred eigenvalues are internally consistent.

2.4 Results

2.4.1 Ice Fabric Parameters from Polarimetric ApRES at EDC

Polarimetric ApRES data collected at EDC are shown in Fig. 2.5a–d. A co-polarization node occurs at 1100m depth, and a second node develops at about 2000m depth (Fig. 2.5a, b). The existence of only one pair of nodes over 2000m indicates comparatively small horizontal ice anisotropy (i.e., low $\Delta\lambda$), similar to what has been observed at Dome Fuji (Fujita et al., 2006). The angular distance between the two copolarization nodes is close to $90°$, consistent with r close to 0 dB (Fig. 2.5a). δP_{HV} shows little depth variability (Fig. 2.5c), suggesting that the ice fabric orientation angle (θ) does not vary strongly with depth. The scaled phase derivative (Ψ, Fig. 2.5d) is unclear in terms of polarity for the top 150 m. Below that, the polarity more clearly indicates the orientation of the largest horizontal eigenvectors.

Optimized model results in Fig. 2.5e–h reproduce the principal patterns of the radar observations. The reconstructed eigenvalues (Fig. 2.5i) capture the observed transition from isotropic to a girdle-type ice fabric in the ice core data. The reconstructed horizontal anisotropy (Fig. 2.5j) captures the mean well ($\overline{\Delta\lambda}_{(z>150\mathrm{m})} = 0.037$), albeit showing less depth variability than the observations. Note that there is no significant change in the eigenvalues and horizontal anisotropy at a depth of the node's occurrence since the node's depth depends on the integration of the horizontal anisotropy above that depth and not at that depth. The ice fabric orientation at the top 150 m is poorly constrained due to the low horizontal anisotropy (Fig. 2.5k). The mean orientation of **v2** below 150 m is $124°$ relative to true north, which is almost perpendicular to the surface flow direction towards $45°$. The orientation cannot be validated with ice core data, which is azimuthally unconstrained. The mean estimated reflection ratio below 150 m is low ($\overline{r}_{(z>150\mathrm{m})} = -3$ dB, Fig. 2.5l), indicating that the role of anisotropic reflections is small.

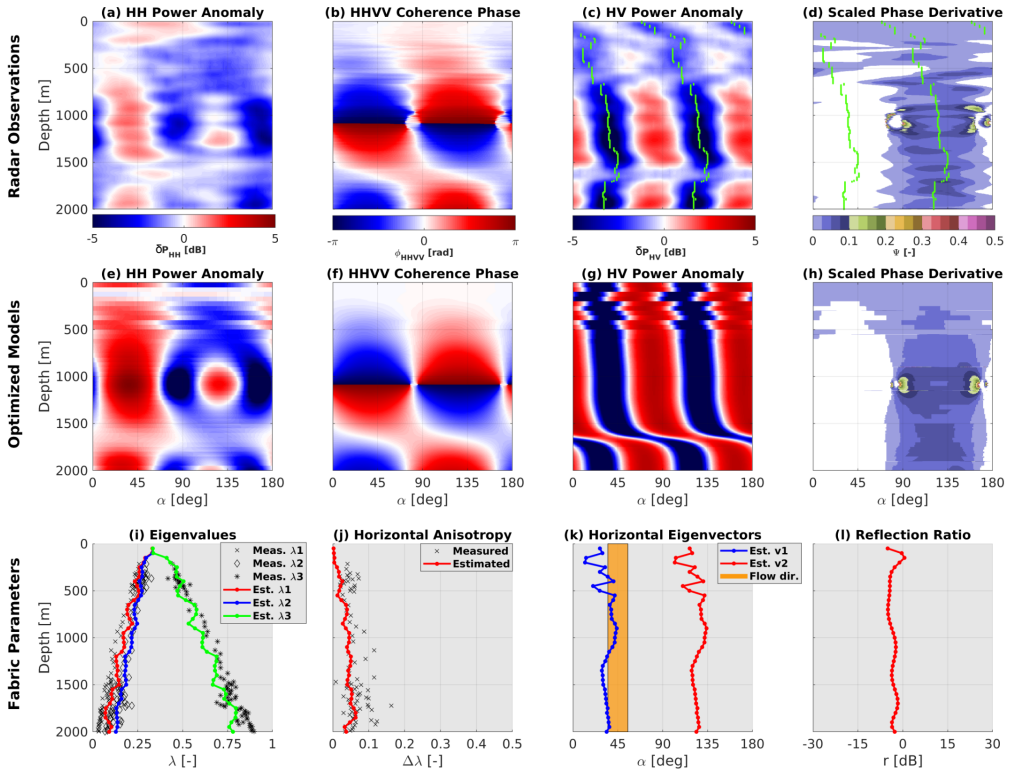

Figure 2.5: Results for EDC: (a)–(d) radar observations, with green lines in (c) and (d) marking the minima in δP_{HV}. (e)–(h) Optimized model output capturing the principle patterns of the observations. (i)–(l) Inferred model parameters validated with ice core data (Durand et al., 2009) in terms of eigenvalues (i) and horizontal anisotropy (j). The inferred **v2** is perpendicular to the mean surface flow direction (k), and the anisotropic reflection ratio is small (l). Note that the negative Ψ values in (d) and (h) are masked for a better demonstration of **v2** orientation.

2.4.2 Ice Fabric Parameters from Polarimetric ApRES at EDML

Next, we apply the inverse approach to ApRES data collected at the EDML drill site. Contrary to what has been observed at EDC, co-polarization nodes can barely be localized in δP_{HH} as no 90° symmetry is apparent (Fig. 2.6a). This indicates that anisotropic scattering is relevant ($r \neq 0$ dB), as already noticed earlier (Drews et al., 2012). Moreover, the coherence phase shows many nodes (Fig. 2.6b), indicating a much stronger horizontal anisotropy (i.e., large $\Delta\lambda$). This is comparable to the ice core at Mizuho, equally located in a flank flow regime (Fujita et al., 2006). Although δP_{HV} shows almost no depth variability in ice fabric orientation (Fig. 2.6c), it is not straightforward to identify the direction of **v1** and **v2** using the polarity of Ψ because of the strong ice anisotropy (Fig. 2.6d).

The optimized model (Fig. 2.6e–h) reproduces all basic features seen in the radar data. Inferred model parameters closely follow the ice core measurements both in terms of absolute

eigenvalues (Fig. 2.6i) and horizontal anisotropy (Fig. 2.6j). A shallower development of the girdle ice fabric compared to EDC is detected. At this site, the mean ice fabric anisotropy at the top 200 m is weak, but in comparison to EDC it is strong enough to detect the ice fabric orientation. The mean estimated horizontal anisotropy below 200 m in EDML ($\overline{\Delta\lambda}_{(z>200\mathrm{m})} = 0.265$) is more than 7 times stronger than EDC. The mean inferred orientation of $\mathbf{v2}$ below 200 m is 174° relative to true north (Fig. 2.6k). Similar to EDC, this is near-perpendicular to the ice flow direction at the surface towards 90°. The estimated reflection ratio in EDML (Fig. 2.6l) can be divided into two major zones ($\overline{r}_{(200\mathrm{m}<z<850\mathrm{m})} = 16$ dB, and $\overline{r}_{(z>850\mathrm{m})} = -15$ dB). Contrary to EDC, anisotropic reflections are more relevant, and the previously suggested existence of two anisotropic scattering zones above and below approx. 850 m (Drews et al., 2012) appears in the observations and the optimized model output.

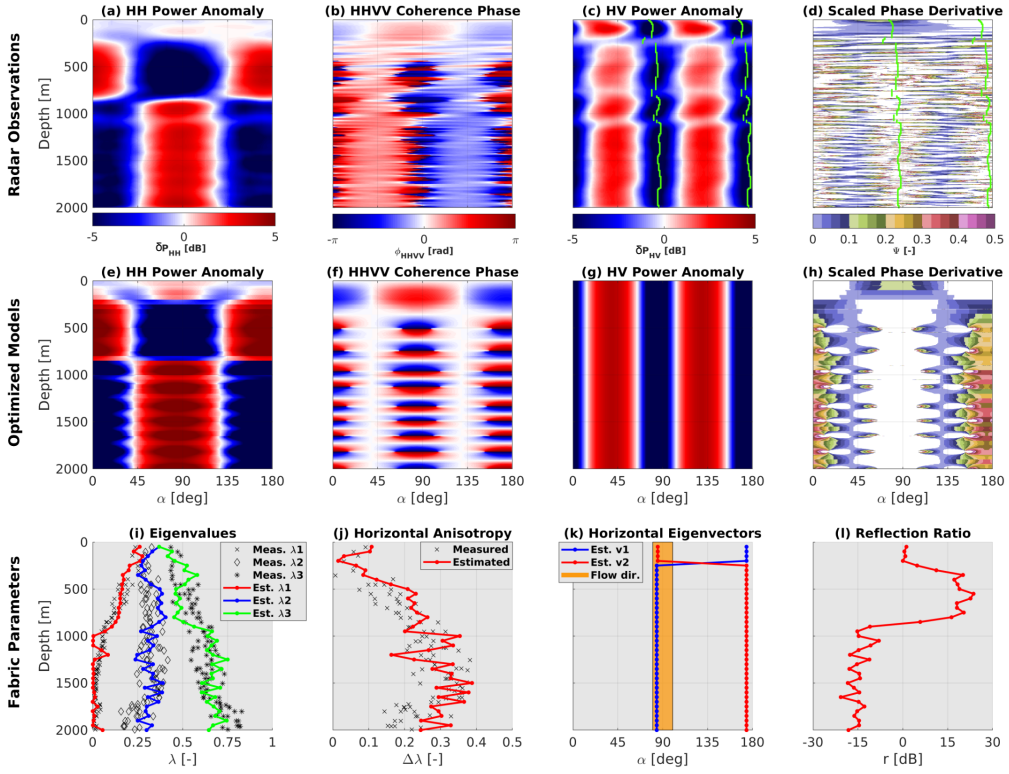

Figure 2.6: Results for EDML: same as Fig. 2.5, with the exception that the measured parameters in (**i**) and (**j**) are from Weikusat et al. (2017).

2.4.3 Spatial Variability of Ice Fabric Parameters in the Local Dome-Flank Transition Zone

After investigating specific characteristics of a dome position (EDC) and a flank-flow regime (EDML), we next investigate a local dome-to-flank transition (36 km). At Dome C, 19 sites are

located along a profile extending 18 km away to either side from the local ice dome (Fig. 2.1a), and a summary of the results is presented in Fig. 2.7. We focus on the upper 2000 m, where the signal-to-noise ratio and the coherence magnitude are sufficiently high. All stations yield coherent results, showing an isotropic ice fabric that gradually evolves into a weak girdle with depth. The depths of the first co-polarization nodes can be detected at all sites (dashed green line in Fig. 2.7b). It is shallowest beneath the dome and moves to larger depths further away from the dome in the flanks. The depth variability in the co-polarization nodes results in a $\Delta\lambda$ that is most anisotropic beneath the dome and less anisotropic in the flanks (Fig. 2.7c). The orientation of the eigenvectors is poorly constrained in the upper 200 m. At larger depths, they are oriented parallel (**v1**) and perpendicular (**v2**) to the surface flow direction, in line with what is inferred in Sect. 2.4.1.

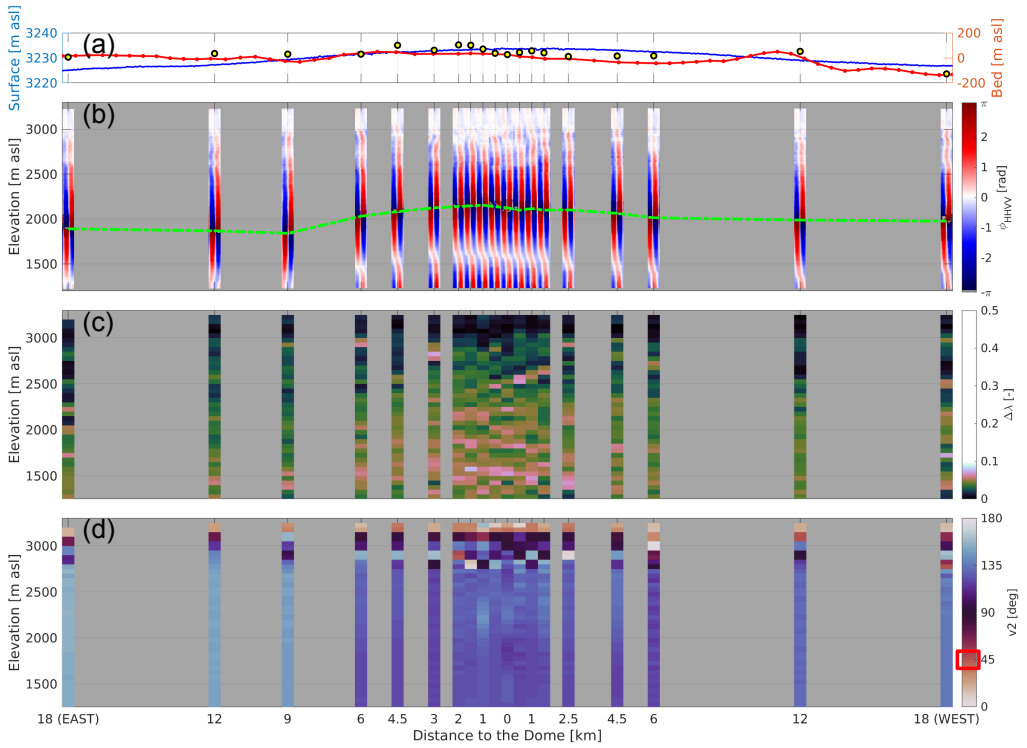

Figure 2.7: Ice fabric evolution in the local dome-to-flank transition at Dome C. (a) Surface (Howat et al., 2019) and bed (Morlighem et al., 2020) elevation in meters above sea level. Yellow circles are the measured bed elevation from radar power return at each site. (b) Observed polarimetric coherence phase difference (ϕ_{HHVV}) at each site. The dashed green line connects the nodes at each site. (c) The optimized horizontal anisotropy ($\Delta\lambda$). (d) The optimized orientation of the largest horizontal eigenvector (**v2**). The red rectangle in the legend marks the surface flow direction. All panels are corrected for the surface elevation, i.e., statically corrected.

2.5 Discussion

2.5.1 Radar Polarimetry as a Tool to Characterize Ice Fabric Variability Horizontally and Vertically

The method we developed in this study extracts the depth variability in ice fabric horizontal anisotropy ($\Delta\lambda$) and anisotropic reflection ratio (r), which leads to estimating all three eigenvalues required for the second-order ice fabric orientation tensor. We also estimate the georeferenced ice fabric orientation (**v2**) as a function of depth. The results of our method are comparable with laboratory measurements (Durand et al., 2009; Weikusat et al., 2017) and could be integrated into anisotropic ice flow models (Azuma, 1994; Azuma and Goto-Azuma, 1996; Gagliardini et al., 2009). Our main assumption is that the strongest eigenvector (and with it the orientation tensor) is aligned in the vertical.

In terms of the data preprocessing, there are no structural differences in our data between synthesizing the polarization dependency out of a single set of quad-polarimetric measurements (Appendix 6.5) and the more common polarimetric measurements in glaciology, where antennas are kept parallel or perpendicular while being rotated several increments between 0 and $180°$ (Fujita et al., 2006). In addition to significantly reducing the field time for data acquisition, an advantage of these measurements is that the georeferencing error only occurs once during antenna setup and is not accumulated over multiple re-positioning cycles. However, it is required that the data have a sufficiently high signal-to-noise ratio (e.g., using $|C_{HHVV}|$) in order to not synthesize misleading symmetries out of noise.

The signal quality and noise level, particularly in the HHVV coherence phase, are important. In areas with high horizontal anisotropy and consequently densely spaced coand cross-polarization nodes (i.e., the EDML case), care needs to be taken that the denoising does not average over multiple nodes. Derivation of the initial guess for the inverse approach depends on the data quality and is guided by characteristic features in synthetic forward models, some of which can be analytically described for one-layer cases. Multi-layer cases, however, are difficult to interpret, particularly if the ice fabric orientation (**v2**) changes strongly (by several tens of degrees) with depth (e.g., ice shelves and glaciers). Fortunately, this does not appear to be the case for the data presented here (Figs. 2.5k, 2.6k) so that the initial guess already results in a forward model that adequately captures characteristic features in the data. The optimization improves the model–data misfit but does not lead to significant differences with our first informed guess. Nevertheless, this step is required to predict the depth variability in all the three eigenvalues (Sect. 2.3.6).

The reconstruction of the eigenvalues assumes isotropic ice and firn for the surface ($\lambda 1 = 0.33$). This is reasonable for the dome and flank-flow settings considered here but may need to be revisited in other settings where ice fabric can develop near the surface as ice streams and ice shelves. More critical is the reflection ratio itself, which is ill-constrained in magnitude and amplifies small changes in the eigenvalues across the reflection boundaries. This is mitigated by the range of allowed eigenvalues (Sect. 2.3.1), and it is those constraints that facilitate the derivation of all eigenvalues from the anisotropic reflection ratio. The predicted eigenvalues ($\lambda 1$, $\lambda 2$, and $\lambda 3$) in this method show a good match to the ice core observations in both cases.

The azimuthal constraints that radar polarimetry provides can, in general, not be validated by ice core measurements, with few exceptions (e.g., Westhoff et al., 2020). However, the alignment of the ice fabric principal axes with the surface-flow direction detailed below adds credibility to our inferences and shows advantages of this approach over previous attempts focusing on

the power anomalies only (Fujita et al., 2006; Matsuoka et al., 2012). The underlying reason for this is that the polarity of the depth gradient of the polarimetric coherence phase is independent of anisotropic scattering.

The inversion requires an initial guess (Sect. 2.3.5) that is based on experience from synthetic test cases. In our experience with radar polarimetry and the explored ice dynamic context, this grants a robust solution, also because a wrong initial guess results in a large model–data misfit that can be identified easily. In the future, this can be improved by using gradient-free optimization schemes (e.g., in a Bayesian framework) that can correct for a poor initial guess by exploring the parameter space more systematically.

Our strongest assumption is that the strongest eigenvector ($\mathbf{v3}$) should be close to vertical. While this assumption is justified here, as flow at domes is dominated by vertical compression, and the crystal c axis tends to be aligned in the vertical, it may not apply elsewhere in ice sheets and cause an additional source of horizontal birefringence (Matsuoka et al., 2009). While it is possible to explore other effects than that of the largest eigenvector being vertical (Jordan et al., 2019, p. 13), it is impossible to circumvent the fact that the radio wave propagation is vertical and hence insensitive to changes along that direction. In the future, we envision the use of wide-angle surveys with curved ray paths (e.g., Winebrenner et al., 2003) to overcome this limitation.

With the assumptions mentioned above, radar polarimetry is now a step closer to constrain the second-order orientation tensor. However, this is still not the full representation required to characterize all ice fabric types, for example because a strong vertical girdle and weak horizontal cones will have a similar second-order orientation tensor. A combination with seismic studies recovering the fourth-order elasticity tensor (Diez and Eisen, 2015; Diez et al., 2015) is therefore still warranted.

2.5.2 Spatial Variability of Ice Fabric Types in Dome-Flank Transitions

We now investigate our inferred characteristics of ice fabric variation at the dome, where flow is dominated by vertical compression, compared with the flanks, where flow is dominated by vertical shear. Our inverse approach shows higher horizontal ice anisotropy at EDML compared to Dome C throughout the ice column. This increase from the dome to the flank supports earlier inferences that ice anisotropy is larger in areas with significant horizontal strain compared to settings where vertical compression is dominant (Fujita et al., 2006; Matsuoka et al., 2012). This is in contrast, however, with the observed decrease in ice anisotropy in the Dome C transect (Fig. 2.7c), where the ice fabric is more anisotropic at the Dome compared to the flanks. Our hypothesis is that this near-field anomaly reflects ice dynamic modification of ice fabric through the Raymond effect (Raymond, 1983). Martín et al. (2009a) predict local ice-dynamically induced ice fabric variability up to approximately five ice thicknesses to either side of ice divides. The 36 km long Dome C transect images an ice thickness of about 3000 km and hence approximately covers this domain. The absence of Raymond arches in the radar stratigraphy beneath Dome C (Cavitte et al., 2016, p. 325) suggests that these need a longer time to evolve, whereas the ice fabric pattern likely reflects the instantaneous operation of the Raymond effect. We acknowledge that there are other explanations for the ice fabric pattern under Dome C, such as across-profile flow or bedrock influence. In any case, we want to highlight here how, due to the spatial extension of our observations, our inferred ice fabric distributions combined with an anisotropic flow model can be used to test these and other hypotheses.

Focusing on the top 200 m of the inferred $\Delta\lambda$ and $\mathbf{v2}$ reveals a significant difference between the two sites. At EDML, the ice fabric anisotropy is stronger in the top 200 m, resulting in a

better-constrained ice fabric orientation, whereas at EDC it is entirely unconstrained (Figs.2.5d and 2.6d). It appears that the ice fabric orientation develops more rapidly in areas with significant horizontal flow compared to areas with essentially vertical compression only.

In both the EDML and Dome C areas, the inferred ice fabric orientation varies little over the depth intervals considered, and in both cases, the inferred orientations line up with the surface flow field. More specifically, $\mathbf{v1}$ is approximately oriented along-flow, and $\mathbf{v2}$ is approximately oriented acrossflow. Those directions also align with the principal strain rate components (Fig. 2.1) in Dome C (Rémy and Tabacco, 2000; Vittuari et al., 2004) and EDML (Drews et al., 2012). In both cases, $\mathbf{v2}$ is approximately parallel to the direction of the maximal principal strain rate component, whereas $\mathbf{v1}$ is aligned with the along-flow minimal principal strain rate component. At Dome C, where ice flow velocities are low, derivation of the strain rate field is not trivial and adds additional assumptions of the surface topography (Vittuari et al., 2004). Note that ice is compressing in the direction of flow and not extending, as is often assumed in simplified theoretical examples, which is why it is important to reference the ice fabric to the direction of extension and compression and not the flow.

The origin of the difference in radar polarimetry between EDC and EDML is the degree of ice fabric alignment in the horizontal, which can be quantified as the difference between the horizontal eigenvalues of the orientation tensor. This difference is larger for EDML than for EDC. Our study adds to the body of evidence that ice fabric is induced by flow because the preferred direction for horizontal ice fabric aligns with the direction of compression (Drews et al., 2012). In addition, the stronger horizontal alignment of the ice fabric at EDML, compared to EDC, corresponds to a stronger compression that can be observed by comparing the strain ellipses in Fig. 2.1. It is interesting to notice how sensitive radar polarimetry is to horizontal ice fabric alignment, the main observable for downward-looking radar. Despite the small differences in horizontal ice fabric eigenvalues at EDC ($\Delta\lambda < 0.05$ in Fig. 2.5j) our technique is able to recover ice fabric in most of the column. This is of particular interest as the ice fabric could contain a record of past changes in ice flow conditions (Brisbourne et al., 2019).

More theoretical work is required to understand the vertical variability in horizontal anisotropy, which is picked up in radar polarimetry through the strength of the anisotropic reflection ratio. At EDML, the reflection ratio is a dominant and required factor to explain the radar signatures, while at Dome C, it is close to negligible. Fujita et al. (2006) have observed a similar increase in anisotropic scattering between Dome F and Mizuho, suggesting that this may be a generic feature in ice sheets that requires more investigation. Contrary to EDML, the signal at Dome C is dominated by birefringence, and the contribution of anisotropic reflection is small. Yet, it appears that it leaves a small signature in the data that can be detected. Moreover, our analysis suggests that there are no other mechanisms (e.g., a directional interface roughness) contributing to anisotropic reflections. This point requires confirmation from other ice core sites because the recovery of all three eigenvalues (and their corresponding directions) offers significant possibilities of constraining ice fabric in ice sheets in general.

Although anisotropic reflections at Dome C are small, there is a noticeable change in the δP_{HH} of direction in the depth interval from 1500–1700 m, which coincides with the transition from Holocene to glacial ice, as is also the case for the EDML site (Drews et al., 2012). The inversion does not pick up this feature in r as it is at the boundary of the domain (Fig. 2.5l), and we do not have a complete understanding why glacial–interglacial transitions should be accompanied by changing reflection ratios. Nevertheless, this may provide us with an additional tool to explore age–depth relationships at future ice core sites.

2.6 Conclusion

We show here the spatial distribution of ice fabric in domes: from the summit, where flow is dominated by vertical compression, to the flanks, where flow is driven by vertical shear. The combination of co- and cross-polarized power anomaly along with the depth gradient of polarimetric coherence phase provides three major parameters and their changes over depth, i.e., the ice fabric orientation, horizontal anisotropy, and its vertical variability. We quantify these changes using an inverse approach that extracts ice fabric information from radar polarimetry. Our method approximates the full orientation tensor including the vertical ice anisotropy. This information can be used in the future to better understand, for example, how susceptible the ice is to shearing within the ice column (Azuma and Goto-Azuma, 1996). We validate our technique with data from two ice core locations situated in contrasting ice flow regimes. The inferred ice fabric orientation aligns with the observed surface velocity and surface strain rate fields. This suggests that polarimetric radar is an ideal tool to map ice fabric characteristics elsewhere as well.

We present ice fabric spatial distribution across a flow plane at Dome C. The 20 ApRES sites in that area are internally consistent, and small changes in the horizontal anisotropy can be horizontally tracked in the polarimetric coherence phase. We detect a minor decrease in horizontal anisotropy away from the dome that we tentatively link to the operation of the Raymond effect. On larger spatial scales, the horizontal anisotropy increases in the flanks (i.e., at EDML), and our findings are consistent with previous studies. Our analysis suggests that ice fabric characteristics can now be reliably inferred in larger parts of Antarctica and the Greenland ice sheet, given that more and more profiles are recorded in a quad-polarimetric configuration. This will be a decisive step to further constrain the anisotropic nature of ice and better understand its contribution to internal deformation.

Chapter 3

Investigating the Dynamic History of a Promontory Ice Rise using Radar Data

M. Reza Ershadi[1], Reinhard Drews[1], A. Clara J. Henry[1,2], Falk M. Oraschewski[1], Carlos Martín[3], Jean-Louis Tison[4], Veronica Tsibulskaya[4], Sainan Sun[5], Sarah Wauthy[4], Inka Koch[1], Paul Bons[1], Olaf Eisen[6,7], and Frank Pattyn[4]

[1]Department of Geosciences, University of Tübingen, Tübingen, Germany. [2]Max Planck Institute for Meteorology, Hamburg, Germany. [3]British Antarctic Survey, Natural Environment Research Council, Cambridge, UK. [4]Department of Geosciences, Environment, Society, Université libre de Bruxelles, Brussels, Belgium. [5]Department of Geography and Environmental Sciences, Northumbria University, Newcastle upon Tyne, UK. [6]Glaciology, Alfred Wegener Institute, Helmholtz Centre for Polar and Marine Research, Bremerhaven, Germany. [7]Department of Geosciences, University of Bremen, Bremen, Germany.

Submitted for publication in *Journal of Glaciology* - September 2023.

Author Contribution

First author:
Scientific ideas: 60%, Data generation: 60%,
Analysis & interpretations: 70%, Paper writing: 75%

M. Reza Ershadi led the code development, analyzing the pRES data, and writing of the manuscript. **M. Reza Ershadi**, Reinhard Drews and Carlos Martín designed the study outline. Frank Pattyn and Sainan Sun collected the pRES data at HIR. Veronica Tsibulskaya, Jean-Louis Tison, Sarah Wauthy led the ice core analysis. Reinhard Drews, Inka Koch and Olaf Eisen led the UWB data analysis and interpretation. Clara Henry designed the SIA model. Falk Oraschewsk inferred the vertical strain rate. Paul Bons and Jean-Louis Tison led the interpretation of the fabric type. All authors contributed to the writing of the final paper.

Abstract

Ice rises hold valuable records revealing the ice dynamics and climatic history of Antarctic coastal areas from the Last Glacial Maximum to today. This history is often reconstructed from isochrone radar stratigraphy and simulations focusing on Raymond arch evolution beneath the divides. However, this relies on complex ice-flow models where many parameters are unconstrained by observations. Our study explores quad-polarimetric, phase-coherent radar data to enhance understanding near ice divides and domes, using Hammarryggen Ice Rise as a case study. Analysing a 5 km profile intersecting the dome, we derive vertical strain rates and ice-fabric properties. These align with ice core data near the summit, increasing confidence in tracing signatures from the dome to the flanks. The Raymond effect is evident, correlating with surface strain rates and radar stratigraphy. Stability is inferred over millennia for the saddle connecting HIR to the mainland, but dome ice-fabric appears relatively young compared to 2D model predictions. In a broader context, quad-polarimetric measurements provide valuable insights into ice-flow models, particularly for anisotropic rheology. Including quad-polarimetric data advances our ability to reconstruct past ice flow dynamics and climatic history in ice rises.

3.1 Introduction

Ice rises are grounded, locally elevated, ice features surrounded by ice streams or ice shelves. They form above areas of shallower bathymetry, which facilitates the accumulated ice to remain above this area. This then results in a locally different flow regime (Matsuoka et al., 2015). Promontory ice rises, such as Hammarryggen Ice Rise (HIR) (Fig. 3.1), are connected to the main ice sheet via a saddle in the surface topography. They may form triple junctions near their domes, from which three ridges extend into the ice-rise flanks. Ice rises have two main characteristics that make them of particular interest: Firstly, they decelerate ice flux from the main ice sheet towards the ocean and consequently delay grounding-line retreat (Favier et al., 2012, 2014; Favier and Pattyn, 2015; Schannwell et al., 2019; Henry et al., 2022). Secondly, they are an archive for the local atmospheric and ice-dynamic history. The latter is accessible through the interpretation of Raymond arches, which are anticlines in the ice stratigraphy that evolves once a local ice dome or ice divide has formed (Raymond, 1983). The presence or absence of Raymond arches provides insight into the ice-rise history, especially the temporal stability of the configuration, and can be used as a tie-point of the ice thickness to constrain continental ice-flow models. Such tie-points are important, as other constraints, such as exposure dating of rock outcrops (Davies et al., 2012), are unavailable for most of the Antarctic perimeter.

Much progress in previous studies has guided the interpretation of observed Raymond stacks (i.e., individual Raymond arches and their evolution with depth) in the context of the ice-dynamic history of a respective catchment (Matsuoka et al., 2015). Clear signatures of transience are Raymond stacks that do not align with contemporary ice divides (Nereson and Waddington, 2002), such as at Siple Dome (Nereson et al., 1998). Fully evolved Raymond stacks that align with the contemporary ice divide location are at the other end of the spectrum and indicate stability (e.g., Derwael Ice Rise; Drews et al. (2015b)). Cases between these two end members (Goel et al., 2020) are more difficult to interpret and require advanced model-data comparison, including thermomechanically-coupled full Stokes models with anisotropic rheology (Martín et al., 2009a,b; Martín and Gudmundsson, 2012) and a dynamically evolving grounding line (Schannwell et al., 2019, 2020; Henry et al., 2022).

A drawback of the model-guided interpretation of observed Raymond stacks is the poorly constrained parameter space. The arch amplitude is impacted by many factors, such as the degree of non-linearity in the Glen's flow law exponent that defines a higher non-linearity (Gillet-Chaulet et al., 2011; Bons et al., 2018) and leads to larger arch amplitudes (Martín et al., 2009a,b; Drews et al., 2015b); the along-ridge flow component, that leads to smaller arches (Martín et al., 2009a,b); the bed topography, a bumpy bed can produce smaller arches (Kingslake et al., 2014) basal sliding that leads to smaller arches (Petit et al., 2003) the surface mass balance, localised erosion at the crest leading to larger arch amplitudes (Drews et al., 2015b; Conway and Wilbour, 1999), the thinning/thickening history, that translates into larger/smaller arches relative to present geometry (Martín et al., 2006; Goel et al., 2018); and the ice anisotropy that affects the geometry of amplitudes of the arches (Martín and Gudmundsson, 2012).

Ice-core analysis, in combination with shallow and deep radar, can constrain the three-dimensional ice geometry (Hindmarsh et al., 2011) and the Holocene surface accumulation history (Philippe et al., 2016; Goel et al., 2017; Cavitte et al., 2022). Strain measurements such as the coffee-can method (Hamilton and Whillans, 2000) and repeat surveys with phase-coherent radar can provide additional constraints on the vertical strain rates (Kingslake et al., 2014). However, other factors, such as ice anisotropy, remain unconstrained, resulting in ambiguous matching of observed Raymond arch stacks with ice-flow models (Drews et al., 2015b). Consequently, so far, ice rises and their inferred dynamic history play a minor role in constraining larger-scale ice flow models (Bentley et al., 2014).

Phase coherent radar polarimetry using a ground-based phase-sensitive Radio Echo Sounder (pRES) (Brennan et al., 2014) has seen much development in terms of inferring ice-fabric types for various flow regimes using the polarimetric coherence phase as a metric to extract information from the birefringent radar backscatter (Dall, 2010; Jordan et al., 2019, 2020; Ershadi et al., 2022b; Rathmann et al., 2022; Zeising et al., 2023). Anisotropic ice-flow models of steady-state ice rises (Martín et al., 2009a,b; Martín and Gudmundsson, 2012) predict strong gradients in ice-fabric types on either side of an ice divide. However, this has thus far not been compared with observations.

Here, we investigate to what extent ice-fabric properties can be derived from quad-polarimetric radar data near a triple junction of HIR in Dronning Maud Land, East Antarctica. We validate the inferred ice-fabric types with ice-core data near the summit and provide additional context in terms of variability in vertical strain rates and corresponding signatures in the radar stratigraphy.

3.2 Study Area

Hammarryggen Ice Rise is a promontory ice rise located in eastern Dronning Maud Land (Fig. 3.1). It has a discernible dome at 367 $\mathrm{m\,a\,s\,l}$ (Howat et al., 2022) that is co-located with a triple junction from which three ridge divides extend into the ice-rise flanks. The ice thickness at the dome is approximately 550 m (Fig. 7.1). In 2019, the airborne ultra-wideband (UWB) radar from the Alfred Wegener Institute was deployed to survey the area providing ice thickness and internal ice stratigraphy data at multiple cross sections roughly oriented along the East-West direction. A 263 m long ice core at the dome provided the age-depth relationship used to date near-surface radar stratigraphy imaged with a different ground-based radar in order to extrapolate the surface mass balance spatially (Cavitte et al., 2022). The ice core was also analysed to investigate ice crystal fabric, and we will use these data to verify inferences drawn from 15

quad-polarimetric radar observations. The average accumulation rate and mean ice thickness within the 5 km pRES profile are reported as 0.4 $\mathrm{m/a}$ (Cavitte et al., 2022) and 550 m, respectively. The ratio of both values provides a characteristic time scale (Martín et al., 2009a), t_D, which for HIR is approximately 1400 years.

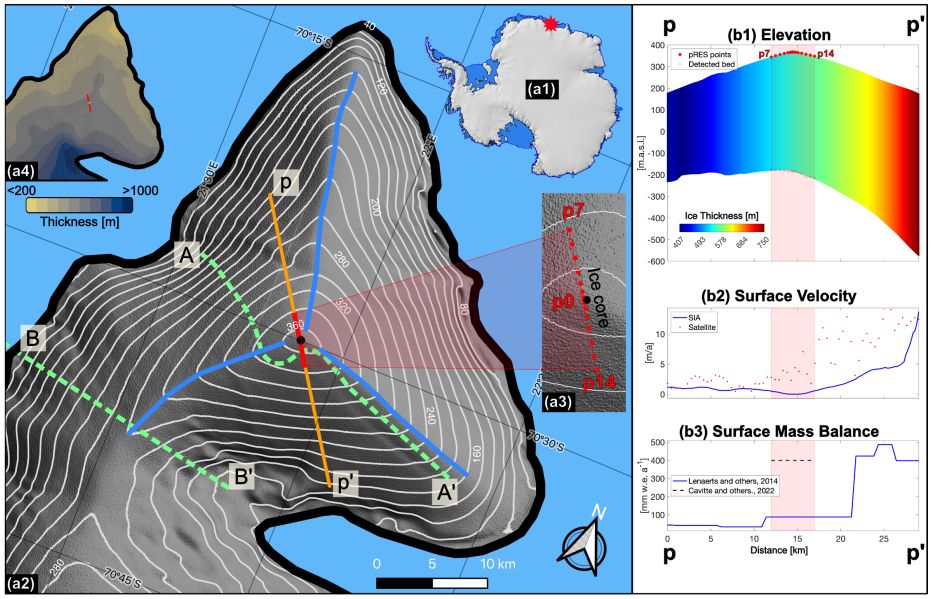

Figure 3.1: (a1) The location of study area in Antarctica. (a2) Hammarryggen ice rise, the white contour lines and satellite background represents the surface elevation derived from the REMA dataset (Howat et al., 2022) . Two green dashed lines represent the UWB flight lines. The blue lines denote the approximate position of the ridges. The black dot represents the location of the ice core and, the red line indicates the pRES profile. (a3) pRES measurement points depicted as red dots in the inset. (a4) shows the ice thickness at HIR (Morlighem, 2022). (b1) to (b3) A cross-sectional view along the extended pp' profile, illustrating key variables including surface elevation (Howat et al., 2022), bed elevation and ice thickness (Morlighem, 2022), surface velocity (SIA and Rignot et al. (2017)), and surface mass balance (Lenaerts et al., 2014; Cavitte et al., 2022). The red shading corresponds to the location of the pRES profile.

3.3 Methods

In 2019, 15 static, quad-polarimetric measurements were taken along a 5 km profile crossing the triple junction HIR in northwest-to-southeast direction (Fig. 3.1a2 - red line). At each site, we infer the magnitude and the orientation of ice fabric with depth (Sect. 3.3.1). One static measurement (site name p0) was taken at a few tens of metres distance from the ice core, which validates our inference with values derived from ice-core data (Sect. 3.3.2). In 2020, all static sites were revisited to determine the yearly-averaged vertical strain rates (Sect. 3.3.3). Additional geophysical context is provided with airborne radar profiles (Sect. 3.3.4) and an approximation of surface velocities and corresponding horizontal strain rates based on the shallow ice approximation (Sect. 3.3.5).

3.3.1 Ice-Fabric Derived from Static, Phase-Coherent Radar

The quad-polarimetric data (Pattyn et al., 2023) at each site were collected with a fixed antenna distance (5 m between centres), and with variable antenna orientation. Following the notation from the satellite remote sensing literature, the two orthogonal polarisations are referred to as horizontal (H) and vertical (V), although they are both situated in the horizontal plane. Each quad-polarimetric measurement consists of four individual measurements with co-polarised (HH, VV) and cross-polarized (HV, VH) orientations. The data can be synthesised to mimic a full azimuthal orientation of the antennas and variations in backscatter power are displayed correspondingly (Young et al., 2021; Ershadi et al., 2022b). The absolute, georeferenced orientation of the baseline connecting the two antennas is determined with a compass with approximately 15° uncertainty.

The backscattered power depends on the antenna orientation due to birefringence and anisotropic reflections that originate from aligned crystal orientation fabric (or in short ice-fabric) which is mechanically and dielectrically anisotropic. The degree of anisotropy is typically described using three eigenvectors ($\vec{v}_1$, $\vec{v}_2$, $\vec{v}_3$) and eigenvalues (λ_1, λ_2, λ_3 with $\lambda_1 < \lambda_2 < \lambda_3$ and $\lambda_1 + \lambda_2 + \lambda_3 = 1$) which correspond to an ellipsoid best describing the crystal c-axis distribution at a given depth interval. The theory of radar polarimetry is detailed in a number of previous publications (Hargreaves, 1977, 1978; Fujita et al., 2006; Dall, 2010; Jordan et al., 2019, 2020). Here, we determine the horizontal ice fabric anisotropy ($\Delta\lambda_H = \lambda_2 - \lambda_1$) and its georeferenced orientation as the direction of the strongest horizontal eigenvector ($\vec{v}_2$) using the approach outlined in Ershadi et al. (2022b). This method employs HH and HV power anomaly data and the HHVV coherence phase, defined as the argument of the complex polarimetric coherence and its scaled phase derivative, which estimates the depth variability of $\Delta\lambda_H$ and $\vec{v}_2$ assuming that one (in this case $\vec{v}_3$) of the eigenvectors is pointing vertically. Additionally, the method allows for the estimation of all three eigenvalues assuming that ice is isotropic at the surface. This enables the reconstruction of the vertical anisotropy ($\Delta\lambda_V = \lambda_3 - \lambda_2$) in a top-to-bottom approach. For HIR specifically, we limit our analysis to a magnitude of coherence of 0.4 following recommendations from Jordan et al. (2019). This covers approximately the upper 400 m, corresponding to approximately 70% of the total ice thickness near the dome (Fig. 7.1).

In order to classify the observed fabric types and their evolution with depth we use a classification scheme that uses logarithmic ratios of the eigenvalues to differentiate between cluster-type (point maximum) and girdle-type ice fabrics (Woodcock, 1977). Shown here are $K = \frac{\ln(\lambda_3/\lambda_2)}{\ln(\lambda_2/\lambda_1)}$ and $C = \ln(\lambda_3/\lambda_1)$. K distinguishes between a uniaxial girdle and a uniaxial cluster, whereas C is a metric for the strength of the respective ice-fabric types.

3.3.2 Ice-Fabric from Ice-Core Data

During the 2018-2019 austral summer field season, a 263 m long ice core was drilled at the summit of HIR (-70.49960°S, 21.88019°E, green dot in Fig. 3.1). The ice core was cut in 0.5 m sections on site, then packed, transported to and stored at the Laboratoire de Glaciologie (Université libre de Bruxelles (ULB), Belgium) respecting the cold chain (temperature below -25°C) at all times. Dating and interpretation of a series of environmental and climatic proxies for the upper 120 metres of the core are beyond the scope of this paper and are in Wauthy et al. (2023) presented separately. Here we will focus on the ice-fabric properties of the entire ice core, more specifically the eigenvalues of the eigenvectors, characterizing the ice-fabric anisotropy that we aim to reconstruct from the pRES measurements.

To determine the eigenvalues of the ice fabric from the ice core, 114 regularly spaced 8 cm high and 500 $\mu\mathrm{m}$ thick vertical thin sections of ice were produced following the standard procedure of Langway (1958). Crystal (optic) c-axes orientations were measured using the G-50 Automated Ice Fabric Analyzer (Russell-Head Instruments, e.g., Wilson et al. (2003)). Eigenvectors and eigenvalues were calculated using the FAME software (Hammes and Peternell, 2016). The same software was used to determine grain boundaries, to plot c-axis orientation density distributions in a lower hemisphere, equal-area or Schmidt diagram. Schmidt diagrams are a common representation in geology providing equi-areal 2D projections of the ice crystal's c-axes intersection with a lower hemisphere into the equatorial plane, chosen in the plane of the vertical thin sections in this study. Density diagrams are constructed by counting the number of c-axes falling in a reference counting circle displaced on a regular grid across the Schmidt diagram.

3.3.3 Vertical Strain Rate

The sites used for the polarimetric surveys (Sect. 3.3.1) were marked with bamboo stakes and revisited one year later. The phase-coherent repeat measurements enable tracking of the submergence of internal reflections relative to the bed (Kingslake et al., 2014). This allows us to infer yearly averaged vertical strain rates, a method which is commonly applied to ice shelves in order to isolate the basal melt rate signal from observed thickness change (e.g., Nicholls et al. (2015); Sun et al. (2019)). For HIR specifically, we calculated depth-averaged values for ice thickness intervals over tens of metres in order to highlight signatures of the Raymond effect.

3.3.4 Airborne Radar Data

The airborne radar data were collected in December 2018 and January 2019 as part of CHIRP (Channel and Ice Rise Project; Fromm et al. (2019)) using the ultra-wideband radar system (UWB) of the Alfred Wegener Institute, Helmholtz Centre for Polar and Marine Research (AWI) with a frequency range of 150-520 MHz. The system is an improved version of the Multichannel Coherent Radar Depth Sounder (MCoRDS 5) developed at the University of Kansas, Center for Remote Sensing and Integrated Systems (Rodriguez-Morales et al., 2014; Paden et al., 2021), operated on AWI's Polar6 BT-67 aircraft (Wesche et al., 2016a). The radar system consists of an eight-element antenna array polarised in HH, which serves as a transmitter and receiver unit for radar signals. Data acquisition and processing methods are detailed in (Koch and others, 2023, in review) and are similar to those described by Franke et al. (2021) and Franke et al. (2022). During CHIRP, the radar transmitted three-stage linear modulated chirp signals (1 μs low-gain, 1 μs high-gain and 3 μs high-gain to sound the upper, middle and deeper part of the ice column in high quality) in a frequency range of 150-520 MHz and at an acquisition height of $\sim$360 m above ground. Radar data processing was conducted with the CReSIS Toolbox (Paden et al., 2021) and comprises pulse compression, synthetic aperture radar (SAR) processing with a wide angular range, and array processing (Rodriguez-Morales et al., 2014; Hale et al., 2016; Franke et al., 2022). The processed radar data have a range resolution of $\sim$0.35 m and an along-track trace spacing of approximately 6 m. Here, we use selected sections of the airborne radar data to analyse signatures of the Raymond arches beneath the dome and the landward-oriented ice divide (Fig. 3.1).

3.3.5 Shallow Ice Approximation: Surface Velocities and Strain Rates

Surface velocities at HIR are too slow to be reliably picked up by remote sensing data. Therefore, we use the shallow-ice approximation (SIA; Hutter (1983); Greve and Blatter (2009)) as a rough estimate of the surface velocity and maximum horizontal strain rate ($\dot{\varepsilon}_{max}$), whilst being aware that a higher-order ice flow model would be more accurate in the region. We use the calculated surface flow direction and the maximum strain rate direction, $\dot{\varepsilon}_{max}$, to compare with the estimated strongest horizontal anisotropy eigenvector, $\vec{v}_2$. The map of HIR with the estimated magnitude and orientation of the surface velocity and maximum horizontal strain rate is shown in Appendix 7.4.

3.4 Results

3.4.1 Internal Stratigraphy

The airborne UWB radar profiles (Fig. 3.2) image ice thickness and internal radar stratigraphy (a. k .a. the isochronal stratigraphy) in profiles located near perpendicular to the local ice divides (Fig. 3.1). The average ice thickness is between 500 and 600 m beneath the divides. The bed increases in elevation towards the west and deepens from the triple junction into the landward direction. The bed beneath the saddle (Profile B-B') appears distinctly rougher than beneath the dome area (Profile A-A'). The internal radar stratigraphy is clearly visible in both profiles but cannot be identified unambiguously at depths deeper than the surface multiple (Koch and others, 2023, in review). Continuous tracking of the stratigraphy is also difficult in areas where internal layers are more inclined (i.e., near the divides), and in areas where the flight track is curved (Fig. 3.1). Nevertheless, internal radar stratigraphy close to the surface appear deeper in the south-eastern flanks compared to the north-western flanks, and their syncline arching beneath the divide is clearly visible in B-B' (i.e., beneath the saddle) and to a lesser extent also along A-A' (just north-west of the dome). The arches increase in amplitude with increasing depth and are vertically aligned with today's divide position (Fig. 3.1).

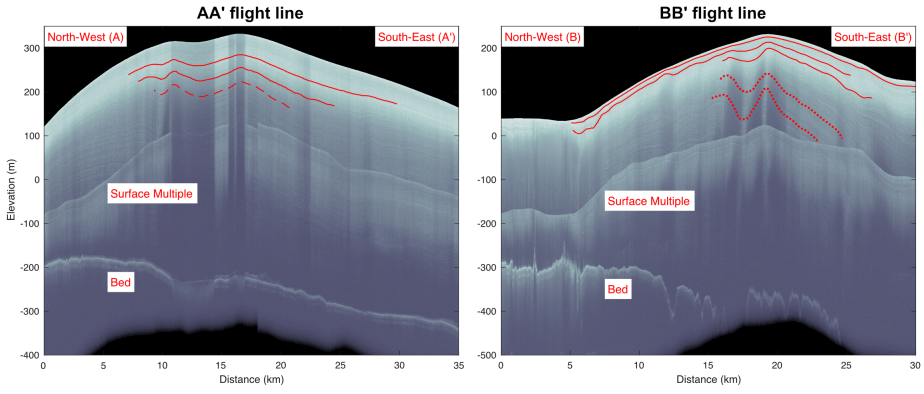

Figure 3.2: Airborne UWB radargrams crossing two ridges of the triple junction dome (A-A') and the saddle ridge (B-B'). Red curves highlight laterally coherent internal reflection horizons, and red dashed lines contain in parts data gaps, particularly in areas where the layers are more inclined.

3.4.2 Inference of Ice-Fabric Parameters from pRES Measurements

We use the pRES measurement site closest to the ice-core site (marked p0 in Fig. 3.1) to illustrate results from the quad-polarimetric analysis. The observations from the quad-polarimetric measurements are displayed using multiple metrics. The HH Power anomaly (Fig. 3.3a) represents the backscatter dependence as a function of antenna orientation and is indicative of anisotropic reflections, e.g., due to vertical variability in ice-fabric strength. The HHVV coherence phase (Fig. 3.3b) shows the phase correlation between the HH and VV directions. Stronger vertical gradients correspond to a stronger $\Delta\lambda_H$. The HV power anomaly (Fig. 3.3c) is an analogue to the HH power anomaly but for the depolarization component and is a proxy for the ice-fabric orientation (marked with green dots). The scaled phase derivative (Fig. 3.3d) of the ice-fabric orientation for a given depth interval (marked with green dots) is defined as $\Delta\lambda_H$. Fig. 3.3e to f show the same metrics based on a radio-wave propagation model (Fujita et al., 2006) and ice-fabric parameters resulting from a non-linear optimization method (Ershadi et al., 2022b).

The characteristic signatures (e.g., nodes, location of maxima, etc.) in the observations (Fig. 3.3a-d) are well reproduced by the simulations (Fig. 3.3e-h) demonstrating that the inferred ice-fabric eigenvalues and their changes with depth are adequately captured by the inversion. The gradient in the polarimetric phase coherence indicates a gradual strengthening of $\Delta\lambda_H$ with depth, and the minima in the HV power anomaly suggest that the ice-fabric orientation changes are small with depth. An exception occurs in the depth interval between 150 and 200 m, where a cross-polarization extinction node suggests a rotation of the $\vec{v}_2$ eigenvector of several degrees (see Fig. 3.3c,g). We first substantiate the inferred ice-fabric parameters from the radar polarimetry by comparing them to ice-core measurements in the following section, and then continue by tracing the ice-fabric parameters away from the ice core into the ice-rise flanks.

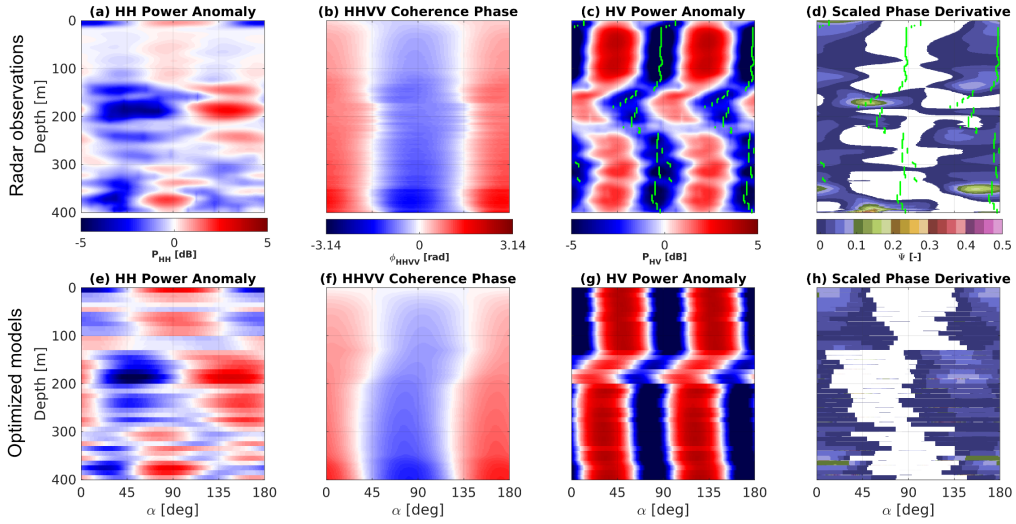

Figure 3.3: Results for the p0 radar site: (a) to (d) pRES observations, with green dots in (c) and (d) marking the minima in PHV. (e) to (h) Optimised model output capturing the principal patterns of the observations.

3.4.3 Ice Core Validation

The fabric data measured from ice core samples show an increase with depth of λ_3 and a decrease of both λ_1 and λ_2 (Fig. 3.4). The measured $\Delta\lambda_H$ indicates a weak horizontal anisotropy within the ice column and remains almost constant with depth. In contrast the measured $\Delta\lambda_V$ increases with depth. This behaviour of eigenvalues results in Woodcock parameters $K > 1$ and $C < 2$ which categorize the fabric type into the weak uniaxial cluster. This behaviour is also visible in the density Schmidt diagrams (increasing areal concentration of crystals c-axes from white to red) shown in Fig. 3.4c for samples below 150 m where the distribution of the crystals slowly (low values on the density scale) evolves from a more random distribution in the top of the ice core towards a single maximum closely centred on the vertical.

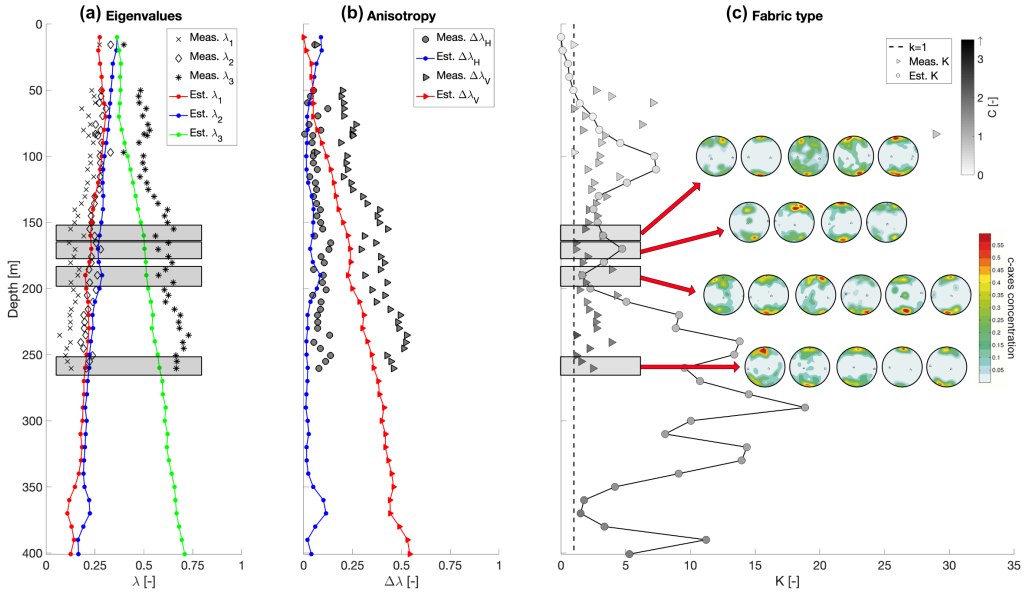

Figure 3.4: Comparison between estimated and measured (a) eigenvalues, (b) horizontal and vertical ice fabric anisotropy as $\Delta\lambda_H$ and $\Delta\lambda_V$, respectively and (c) Woodcock values K and C with density Schmidt diagrams measured from the ice core. Note that the estimated values are the results from the inverted radar data, and the measured values are from the ice-core laboratory analysis.

The estimated eigenvalues from the quad polarimetric radar measurement at site p0 are compared with the measured ice-core eigenvalues (Fig. 3.4). The estimated eigenvalues and anisotropy in both horizontal and vertical direction following the same behaviour as the measured. However the estimated λ_1 and λ_2 (Fig. 3.4a) are about 0.07 and 0.03 larger than the measured values, respectively, and consequently, the estimated λ_3 is systematically smaller than the measured value. Both estimated and measured $\Delta\lambda_H$ are weak (approximately 5% of the maximum possible horizontal anisotropy $\Delta\lambda_H = 1$ (Fig. 3.4b), with the estimated one being slightly weaker than the measured one). In contrast, both the estimated and measured vertical ice fabric anisotropy $\Delta\lambda_V$ increase with depth (Fig. 3.4c). Similar to $\Delta\lambda_H$, the estimated $\Delta\lambda_V$ is also weaker than the measured $\Delta\lambda_V$.

Similarly to the ice core data, the radar-derived fabric shows a tendency to form clusters which increase in strength with increasing depth (Fig. 3.4c). The differences seen in the eigenvalue magnitudes correspondingly translate into the K and C classification: The estimated C values (colour of marks in Fig. 3.4c) are weaker than the measured ones, particularly on the shallower part of the ice column. The minimum C value estimated from radar at site p0 is 0.19, and the maximum is 1.81. In contrast, the ice core values are 0.36 and 2.35, respectively. The estimated $\Delta\lambda_H$ between 350 and 380 increases to 0.12 (Fig. 3.4b), resulting from the corresponding change in λ_1 and λ_2 (Fig. 3.4a). This behaviour does not affect $\Delta\lambda_V$ (Fig. 3.4c), but it does affect the K value (Fig. 3.4c) which is close to one here. However, no ice-core data is available at that depth to validate this behaviour.

3.4.4 Spatial Changes in Ice-Fabric and Vertical Strain Rates Along the 5 km Transect

After comparing the consistency between the estimated eigenvalues derived from polarimetric radar data at the p0 site and the measured ice core eigenvalues, we reconstruct ice-fabrics for all sites p1 to p14 along the 5 km long tranSect. To interpret our results, we normalize distances and elevation with the ice thickness at the dome ($H \simeq 550$ m). The distance of the pRES points from the dome denoted as X is normalized as $x = X/H$. Additionally, elevation is expressed as the normalized ice height above the bedrock, denoted as $z = (H - Z)/H$, where Z represents the depth. In this context, the mean bed elevation and mean surface elevation along the pRES profile are designated as $z = 0$ and $z = 1$, respectively. Subsequently, we employ linear interpolation to obtain the spatial variation of the fabric parameters along the 2D transect (Fig. 7.3).

Depth-averaged values of the horizontal anisotropy $\Delta\lambda_H$ show differences on both sides of the divide (Fig. 7.3a). On the south-eastern side, where ice is thicker, values of $\Delta\lambda_H$ are in general larger and more variable than on the north-western side. In the 30 – 35 $\%$ depth-interval , the averaged $\Delta\lambda_H$ exhibits a local maximum beneath the summit that is approximately one ice thickness wide and is asymmetrical. The north-western side also exhibits slightly smaller maxima beneath the ice-rise flanks. The spatial distribution of the magnitude of the strongest estimated eigenvector λ_3 (Fig. 7.3b) exhibits a similar pattern in terms of a local maximum beneath the divide and has generally larger values on the north-western side. The depth-average orientation of $\vec{v}_2$, aligns within $10\mathrm{deg}$ with the North-South direction (Fig. 7.3c). This direction is $\sim 40\,\mathrm{deg}$ offset to the mean flow direction in the ice-rise flanks and $\sim 81\,\mathrm{deg}$ offset to the direction of maximum horizontal strain inferred from the SIA-based velocity field. The magnitude of the depth-averaged vertical strain rates (Fig. 7.3d) is highest in the top 20 $\%$ of the ice thickness (80 to 100 $\%$ depth interval), where the densification of firn is strongest. Vertical strain rates are also overall smaller in absolute value in the thinner north-western flank than the thicker south-eastern flank. At approximately 50$\%$ of the ice thickness, the vertical strain rates exhibit a pronounced (weakly double-peaked) minima beneath the divide which extends laterally for 1-2 ice thickness into the ice-rise flanks.

3.5 Discussion

Previous studies have investigated ice-rise evolution using flow-line modelling in combination with the internal isochronal radar stratigraphy as principal observations (Martín et al., 2009a,b; Hindmarsh et al., 2011; Martín and Gudmundsson, 2012; Drews et al., 2013, 2015b; Goel et al.,

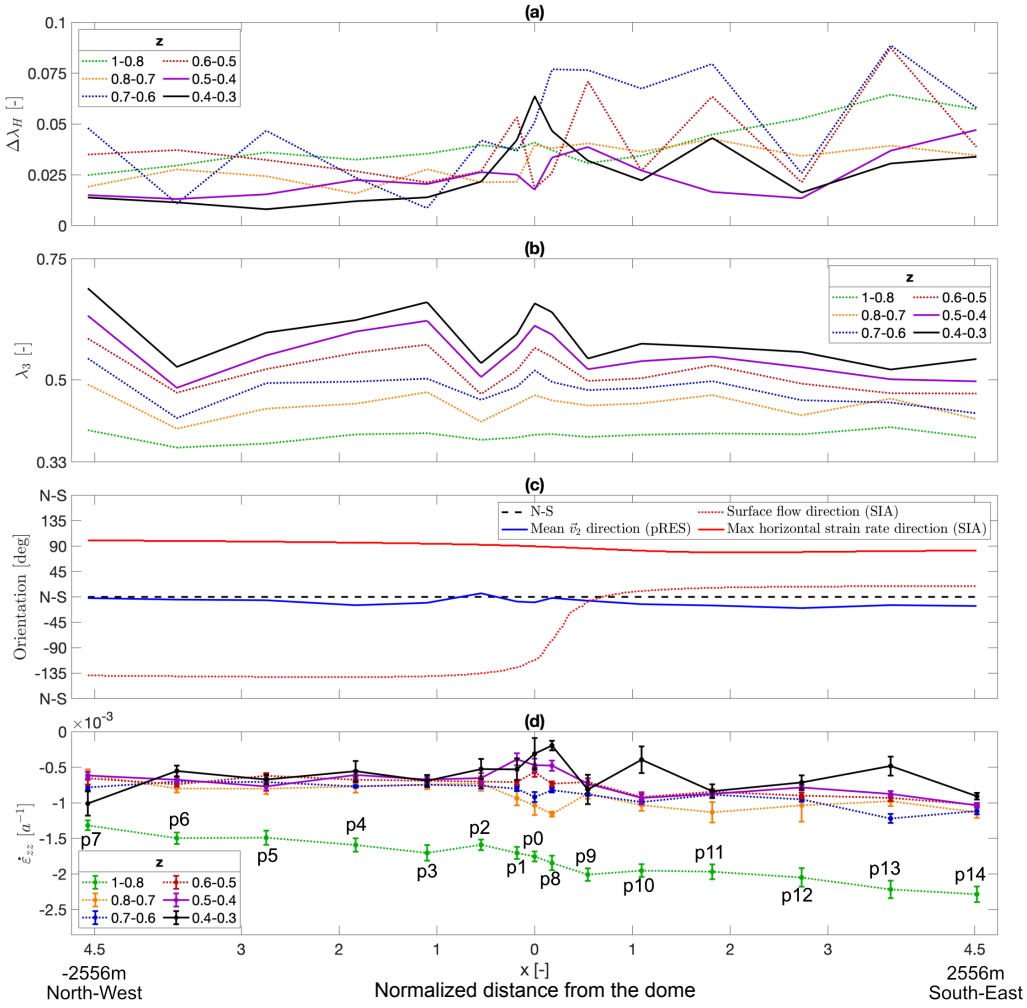

Figure 3.5: (a) Depth-averaged variation of $\Delta\lambda_H$ within a specific depth window. (b) Depth-averaged variation of λ_3 within a specific depth window. (c) Depth-averaged horizontal ice fabric orientation (blue line), surface flow direction derived from SIA (dashed red), and maximum strain direction derived from SIA (red line). (d) Vertical strain rates measured at each pRES site averaged over different depth intervals. Note that more negative strain rates indicate stronger deformation. The x-axis is the distance from the dome normalized by H.

2017, 2018) Two additional studies of a dome and ice rise, respectively, used the observed vertical strain rates (Gillet-Chaulet et al., 2011; Kingslake et al., 2014). Here we use all of the previous observations and add quad-polarimetric radar measurement as another possible observational constraint. We now investigate whether those observations capture signatures of the Raymond effect and, if so, how these can be contextualised with other geophysical observations of the

contemporary flow regime. This may guide the application of a future 3D model (incl. thermo-mechanical coupling and anisotropic rheology) which is capable of simulating the complex dynamics occurring at triple junction ice rises. Given that the extraction of ice-fabric parameters from quad-polarimetric data using non-linear inversion has so far only once been compared with direct ice-core measurements (Ershadi et al., 2022b), we first discuss the benefits and limitations of this method in general before moving on to investigate the flow history of HIR.

3.5.1 Applicability of the Inferred Ice-Fabric Eigenvalues

The quad-polarimetric analysis has a limitation in that it assumes one of the principal eigenvectors points upwards. Although this assumption can be relaxed (Rathmann et al., 2022), it leads to a more complicated forward model for which the inversion is not yet established. However, (Rathmann et al., 2022) show that the polarimetric radar response of nadir-looking radars is comparatively insensitive to ice fabrics that are vertically tilted. However, beneath ice domes vertical compression is assumed to dominate, which is expected to lead to a vertical point maximum in the c-axes distribution (Budd and Jacka, 1989; Llorens et al., 2022) We, therefore, consider the assumption of horizontal and vertical eigenvectors to be justified, and not likely a cause for the systematic mismatch in magnitude that we observe between the eigenvalues from the quad-polarimetric method and the ice-core-based values (Fig. 3.4a).

The systematic underestimation of $\Delta\lambda_H$ and $\Delta\lambda_V$ compared to ice-core values has to a lesser extent also been observed at the ice-core site of the European Project for Ice Coring in Antarctica (EPICA) at Concordia dome C (EDC), however, it does not occur at the EPICA site in Dronning Maud Land (EDML) (Ershadi et al., 2022b). We investigated if using a scaling factor to the dielectric anisotropy for a single crystal (commonly assumed to be 0.034 (Matsuoka et al., 1997)) can explain the underestimation. However, the mismatch did not significantly improve when changing dielectric anisotropy within the reported uncertainties. The inversion is also sensitive to the fabric orientation and backscatter ratio. The latter in turn varies according to the ice-core data on shorter spatial scales than what the inversion can currently resolve, particularly because it involves vertical averaging to smooth the phase gradient. The reason for the underestimation of $\Delta\lambda_H$ and $\Delta\lambda_V$ therefore requires further investigation, but given that the gradients are well reproduced, this does not hinder the interpretation of lateral ice-fabric variability.

3.5.2 pRES Detects Geo-Referenced Fabric Orientation

The estimated $\vec{v}_2$, as depicted in figure 3.5c, is derived solely from pRES data, without validation from field datasets. To overcome this limitation, we used surface flow direction data obtained from SIA modeling to compute the eigenvectors and eigenvalues of the strain rate tensor $\dot{\varepsilon}$. When comparing $\vec{v}_2$ to the surface flow direction, a deviation of $\sim 40°$ is observed (Fig. 3.5c blue vs. dashed red). In contrast, when compared to the direction of maximum horizontal strain rate, $\vec{v}_2$ shows a deviation of $\sim 81°$ (Fig. 3.5c blue vs. solid red).

It is established by Alley (1992) that during ice deformation, c-axes consistently rotate towards maximum finite shortening axes (compressive axes). Also, the principles of fabric orientation under vertical shortening is discussed by Passchier (1997) where the theory explains that basal planes rotate towards the horizontal plane, which serves as the fabric attractor. Consequently, the perpendicular c-axes rotate towards the vertical direction. The rotation is most rapid in the plane containing the direction of maximum shortening (vertical) and maximum

stretching. As a result, the variation in the horizontal c-axes, described by λ_1 in the direction $\vec{v}_1$, is narrowest in this plane. $\vec{v}_2$ is perpendicular to this direction in the horizontal plane, hence it is expected to be oriented at 90° to the direction of maximum stretching, which indeed corresponds to our observations in figure 3.5c ($\sim$ 81°). Also as suggested by the pRES and measurements, λ_1 and λ_2 exhibit similar intensities (weak $\Delta\lambda_H$), it follows that the same might hold true for $\dot{\varepsilon}_1$ and $\dot{\varepsilon}_2$. Their combination would then yield maximum horizontal strain at approximately 45° from $\vec{v}_1$ and $\vec{v}_2$. This explains why $\vec{v}_2$ appears at approximately 45° from the flow direction in figure 3.5c ($\sim$ 40°).

3.5.3 Synthesis of Radar Observations within the Ice-Dynamic Setting of HIR

The radar stratigraphy, the strain rates and the ice-fabric properties are all jointly influenced by the ice-dynamic evolution of HIR and encode parts of its history, even though it is not yet clear how rapidly ice-fabric parameters change with the ice-dynamic flow regime. Here we synthesise the different datasets with a particular focus on the Raymond effect and contextualise our findings with available modelling and observational studies of other ice rises.

The upward arches observed beneath the saddle (B-B', Fig. 3.2) are typical of ice rises in the sense that they are located beneath today's divides and that they are asymmetrical in shape. For example, a syncline as on the western side has also been observed at Derwael Ice Rise and explained with persistent accumulation patterns including erosion of snow at the crest and redeposition in the flanks (Drews et al., 2015b). Erosion of snow at the crest increases the amplitudes of the upward arches at larger depths which are, however, primarily formed by the Raymond effect. Both mechanisms require a stable ridge divide position and therefore testify that the saddle connecting HIR with the main ice sheet was stationary, probably for several t_D, i.e., several thousands of years. Upward arching also occurs beneath the dome (at kilometre 10 in profile A-A', Fig. 3.2), but the amplitudes are smaller compared to the saddle. The eastern side of A-A' is near-parallel to the eastern arm of the triple junction and hence strong upward arching is not expected in the stratigraphy here. It is therefore unclear if the triple junction of HIR exhibits a Raymond cupola as modelling would suggest (Hindmarsh et al., 2011), but if it does, the lower arch amplitudes could suggest that the dome position is younger than the saddle, although three-dimensional effects may be responsible.

For a two-dimensional, plain strain flow regime, it is well understood that lateral differences in vertical velocities that accompany the formation of Raymond arches, are expressed by corresponding patterns in the vertical strain rates. More specifically, the vertical strain rates are expected to be smaller in magnitude for 100 to 300 m depths (z from $\sim$ 0.8 to 0.5) beneath the divide compared to the flanks (Kingslake et al., 2014). Our observations (Fig. 3.5d) comply with these predictions, particularly for 330 to 380 m depths (z from $\sim$ 0.4 to 0.3). At shallow depths (top 100 m) the vertical strain rates are dominated by firn compaction, and deeper depth intervals could not be resolved. Observed magnitudes of approx. 1.0×10^{-3} m/a are comparable to what has been observed at other triple junctions (i.e., Fletcher Promontory (Kingslake et al., 2014)), although the amplitude of the vertical strain rate anomaly across the dome is smaller. Once a local divide or dome has formed, the effect on the velocity field is instantaneous, and hence the vertical strain rates do not contain information about the ice-rise history per se. However, ice-fabric types are strain-induced and develop over time (Budd and Jacka, 1989). Consequently, if the dome position was temporally stable, corresponding signatures should appear in the derived ice-fabric types from the quad-polarimetric analysis, indicating a temporarily stable dynamic

regime.

Regarding the ice fabric, below 150 m where the distribution of the crystals slowly (low values on the density scale) evolves from a more random distribution in the top of the ice core towards a single maximum closely centred on the vertical as expected from dominant uniaxial compression at ice domes‘ (e.g., Durand et al. (2007)). The build-up of this fabric anisotropy is clearly seen in the evolution of the measured eigenvalues in the left panel of Fig. 3.4a. Deformation-wise, this suggests a departure from pure-shear uniaxial compression with differential deformation (such as lateral extension) in the horizontal plane, coherent with the complexity of the geomorphological setting. The ice-fabric reconstruction from the quad-polarimetric data shows that minima in the vertical strain rates (Fig. 3.5d) are accompanied by corresponding maxima in $\Delta\lambda_H$ and λ_3 (Fig. 3.5a,b) in 330 to 380 m depth interval (z from $\sim$ 0.4 to 0.3). This is in line with measured ice fabric and two-dimensional model predictions Martín et al. (2009a) which predicts a single maximum fabric which is stronger beneath the divide compared to the flanks.

A quantitative comparison in terms of timing between our observations and the model predictions Martín et al. (2009a) is hampered in several ways: first, the assumed two-dimensional geometry does not include the triple junction geometry of HIR, and second, the model predictions assume an evolution from fully isotropic to fully anisotropic ice. The latter is unlikely to be the case for HIR as demonstrated by the measured ice fabric data. Notwithstanding, in steady-state (i.e., at approximately 10 times t_D) the predicted degree in ice-fabric anisotropy is larger than what is reconstructed from quad-polarimetric data here. The reconstructed $\Delta\lambda_H$ consistently remains below 0.1 which is comparable to other domes such as Dome C, but is much weaker than what has been observed in flank flow regimes such as the transient divide at the EDML drill site ($\Delta\lambda_H > 0.3$, Ershadi et al. (2022b)). Based on these comparisons, it appears that HIR in terms of its ice-fabric characteristic is not older than 4 times t_D (i.e., not older than approx. 5600 years). However, given the discrepancies between the model assumptions and observations, this time interval is not well constrained.

Taken together, the UWB radar profile across the saddle suggests a temporally stable divide position. The data at the dome is less conclusive in that sense, because arch amplitudes are smaller and because the ice fabric is only weakly developed. One plausible scenario uniting this would be that HIR undergoes a transition from a promontory towards an isle-type ice rise, which is a feature of deglaciation scenarios in this particular region (Favier and Pattyn, 2015). Thinning in the saddle area would then result in comparatively large arches relative to today's ice thickness in this area. The good match to the ice-core data reinforces that quad-polarimetric surveys can be a reliable tool to further constrain ice-rise evolution, in particular the influence of ice-anisotropy on Raymond arch evolution. For HIR, the comparatively weak ice -fabric suggests a comparatively young dome. However, a single two-dimensional profile heavily simplifies the dynamic complexity and modelling should account for these three-dimensional effects in the future.

3.6 Conclusion

We have investigated radar-derived properties of Hammarryggen Ice Rise: radar stratigraphy, strain rates, and ice-fabrics. Upward arching in the stratigraphy indicates a stable ice divide in the saddle area over, at least, several thousands of years. Upward arching beneath the dome is also observed but is less clear. Vertical strain rates are dominated by firn compaction near

the surface, and exhibit a minimum closer to bed indicative for the Raymond effect. The derived ice-fabric properties from quad-polarimetric radar fit ice-core-based values. The horizontal anisotropy is weak and thus young compared to steady-state, ice-dynamically evolved ice-fabric types predicted from two-dimensional models in comparable settings. This is perhaps indicative of thinning of the saddle connecting the dome to the mainland. There are also signatures of the Raymond effect in the ice-fabric. However, it is unclear how the triple junction geometry of Hammarryggen Ice Rise impacts both the vertical strain rates and the ice-fabric development. The synthesis of the different radar observations has the potential to constrain unknown parameters like the ice fabric in future ice-flow modelling, particularly if measurements cover larger areas. Overall, we suggest that these additional geophysical constraints provide another step forward towards a quantitative interpretation of Raymond arch amplitudes using observationally constrained, anisotropic, three-dimensional ice-flow models of triple junctions, flow regimes common to many ice rises around Antarctica.

Chapter 4

Autonomous Rover Enables Radar Profiling of Ice-Crystal Fabric in Antarctica

M. Reza Ershadi[1], Reinhard Drews[1], Jonathan Hawkins[2], Joshua Elliott[3], Austin P. Lines[3], Inka Koch[1], and Olaf Eisen[4,5]

[1] Department of Geosciences, University of Tübingen, Tübingen, Germany. [2] School of Earth and Environmental Sciences, Cardiff University, Cardiff, UK [3] Polar Research Equipment, Etna, NH, US. [4] Glaciology, Alfred Wegener Institute, Helmholtz Centre for Polar and Marine Research, Bremerhaven, Germany. [5] Department of Geosciences, University of Bremen, Bremen, Germany.

Submitted for publication in *IEEE Transactions on Geoscience and Remote Sensing Journal.* - October 2023.

Author Contribution

First author:
Scientific ideas: 60%, Data generation: 85%,
Analysis & interpretations: 90%, Paper writing: 80%

M. Reza Ershadi lead the code and hardware development of SLEDGE, data acquisition in the field and data processing. Reinhard Drews designed the study outline. Olaf Eisen supported the field test of SLEDGE. Reinhard Drews, Jonathan Hawkins, Inka Koch and Olaf Eisen supported the data acquisition in the field. Joshua Elliot and Austin P. Lines developed the original version of the rover (FROSTYBOY) and advised on hardware development for SLEDGE. All authors contributed to the writing and editing of the final paper.

Abstract

Ice-penetrating radar is an extensively used geophysical tool in cryosphere sciences with sounding depths of several kilometers due to the small radio-wave attenuation in ice sheets. Detection of the ice thickness (and in parts also the internal ice stratigraphy) has become standard. However, there is still observational gap in dielectric and mechanical ice-fabric anisotropy. Recently ground based phase coherent radar showed its potential to fill this gap. However, this requires that the corresponding ground-based radars cover profiles with several tens of kilometers in length. We address this challenge by modifying an autonomous rover to include real-time kinematic positioning and direct coupling with a phase-coherent, quad-polarimetric radar. In a proof-of-concept study in Antarctica, we demonstrate that this allows the collection of quad-polarimetric data along a 23 km profile mapping anisotropic ice-fabric properties at <100 m intervals across the transition of grounded to floating ice. This is a step forward to inform ice-flow models with currently missing rheological parameters. The system can drag more than 200 kg, operates autonomously with a battery run time of over six hours, and has a modular design that enables future integration of different radars or other geophysical sensors.

4.1 Introduction

Ice flow models predicting Antarctica's contribution to future sea level rise typically apply an isotropic rheology (Seroussi et al., 2020), although it is known that ice is mechanically anisotropic (Faria et al., 2014a). One reason why anisotropic rheology is not yet operationally implemented lies in insufficient observations which could spatially constrain anisotropic ice properties. The best observations are currently restricted to point information from ice cores predominantly taken from Antarctica's interior (Faria et al., 2014a; Weikusat et al., 2017). Radar and seismic surveys have been developed as an additional tool to estimate lower resolution ice-fabric anisotropy away from ice cores (Hargreaves, 1977, 1978; Fujita et al., 1999, 2006; Eisen et al., 2007; Jordan et al., 2019, 2020; Young et al., 2021; Ershadi et al., 2022b; Gerber et al., 2023), however, so far those approaches are also limited to point measurements.

A promising instrument to constrain anisotropic ice properties is the Autonomous phase-sensitive Radio Echo Sounder (ApRES) (Brennan et al., 2014; Nicholls et al., 2015). Here, this is referred to as pRES since the unattended mode is not used. pRES has had success in various other applications including determination of basal melt rates (Zeising et al., 2022), firn compaction rates (Case and Kingslake, 2021), vertical strain rates (Kingslake et al., 2014), and the Glen flow index (Gillet-Chaulet et al., 2011), and can also be used to infer horizontal ice-fabric anisotropy from quad-polarimetric data (Jordan et al., 2019, 2020; Young et al., 2021; Ershadi et al., 2022b; Zeising et al., 2023). However, the pRES was originally designed exclusively for stationary operations, limiting its versatility in obtaining spatially distributed data. In previous studies (Jordan et al., 2020; Young et al., 2021; Ershadi et al., 2022b), the spatial coverage was so far limited to selected profiles with < 10 km in length and with a sampling interval typically >500 m. This often makes it difficult to trace polarimetric (and hence ice-fabric) signatures spatially across different flow regimes. Here we combine the pRES with an autonomous rover so that ice-fabric properties can be inferred along longer and more densely spaced profiles from quad-polarimetric radar data.

Radar data has been collected by autonomous rovers both in the Arctic (Trautmann et al., 2009; Hoffman et al., 2019; Mankoff et al., 2020) and the Antarctic (Arcone et al., 2015). While

there are examples of coherent radars being deployed in this way (Ray et al., 2014; Hamran et al., 2020), many of these efforts rely on commercial, incoherent radars. These are excellent tools, e.g., for tracing internal layers (Koch et al., 2023a) and/or crevasse detection, but they have limitations in resolving properties such as ice-fabric anisotropy because the received signal phase is not recorded. This limits the applicability of polarimetric surveys as done here, but also of other applications such as synthetic aperture radar processing relevant for smaller-scale processes such as basal terracing (Dutrieux et al., 2014) or subglacial conduit formation (Drews et al., 2017; Church et al., 2020).

To address these limitations, we introduce a **S**elf-guided four-whee**L**ed rov**E**r for ra**D**ar profilin**G** on ic**E (SLEDGE)**, designed to (1) collect quad-polarimetric radar data with pRES radar along pre-defined tracks several tens of kilometers in length, (2) collect radar data with other phase-coherent radars suitable for SAR processing (not shown here) requiring a sub-dcm positioning along profiles more than several hundreds of meters in length, and (3) enable different measuring modes during profiling through integration of the rover and radar. Here, we use a multiple-input multiple-output (MIMO) pRES and integrate it into SLEDGE to autonomously map the ice base, detect internal layers, and, most significantly, acquire polarimetric data for inferring ice fabric properties (section 4.2). We then present the results of a first deployment on the Ekström ice shelf in East Antarctica (section 4.3) and report our test and field observations of SLEDGE for future development (section 4.3.4).

4.2 SLEDGE

4.2.1 Overview

The key components of SLEDGE (Fig. 4.1) include a four-wheeled rover equipped with a mini-industrial computer, two metal-free Cross Fox Sleds holding a pRES radar and four antennas, two GNSS navigation systems mounted on the rover, and a control station. The rover can drive, self-guided, to predefined locations and then trigger radar data acquisition. SLEDGE design is modular having enough space for additional sensors such as camera, a laser scanner, or other geophysical sensors. Here, only a pRES radar with a quad-polarimetric antenna setup will be shown. In terms of the driving mechanics, we rely on a commercially available rover, FrostyBoy (section 4.2.2). We modified some hardware and the entire software to facilitate radar and GNSS sensor integration (section 4.2.2). The commercial names, models, and information of the main components of SLEDGE are presented in Appendix 8.5.

4.2.2 Rover

The hardware of the rover, (Mankoff et al., 2020; Lines et al., 2023), is manufactured by Polar Research Equipment. This four-wheeled rover features four individual brushless DC electric motors, each with a 40:1 planetary gearbox, allowing for independent propulsion. Two motor controllers are used to manage the front and rear motors, which, according to our test, allow the rover to pull more than 200 kg on ice, however the payload in our case was roughly 100kg (incl. two sledges (60 kg) and the radar system (40 kg).) FrostyBoy is equipped with a radio transceiver and antenna for receiving commands and transmitting telemetry, along with a GNSS system for coarse navigation with a horizontal accuracy of approximately 3 m. At the core of the rover's electronic system is an Arduino board. The power supply is facilitated by seven Lithium-Ion (Li-ion) battery modules, collectively providing an approximate total voltage of 56V providing

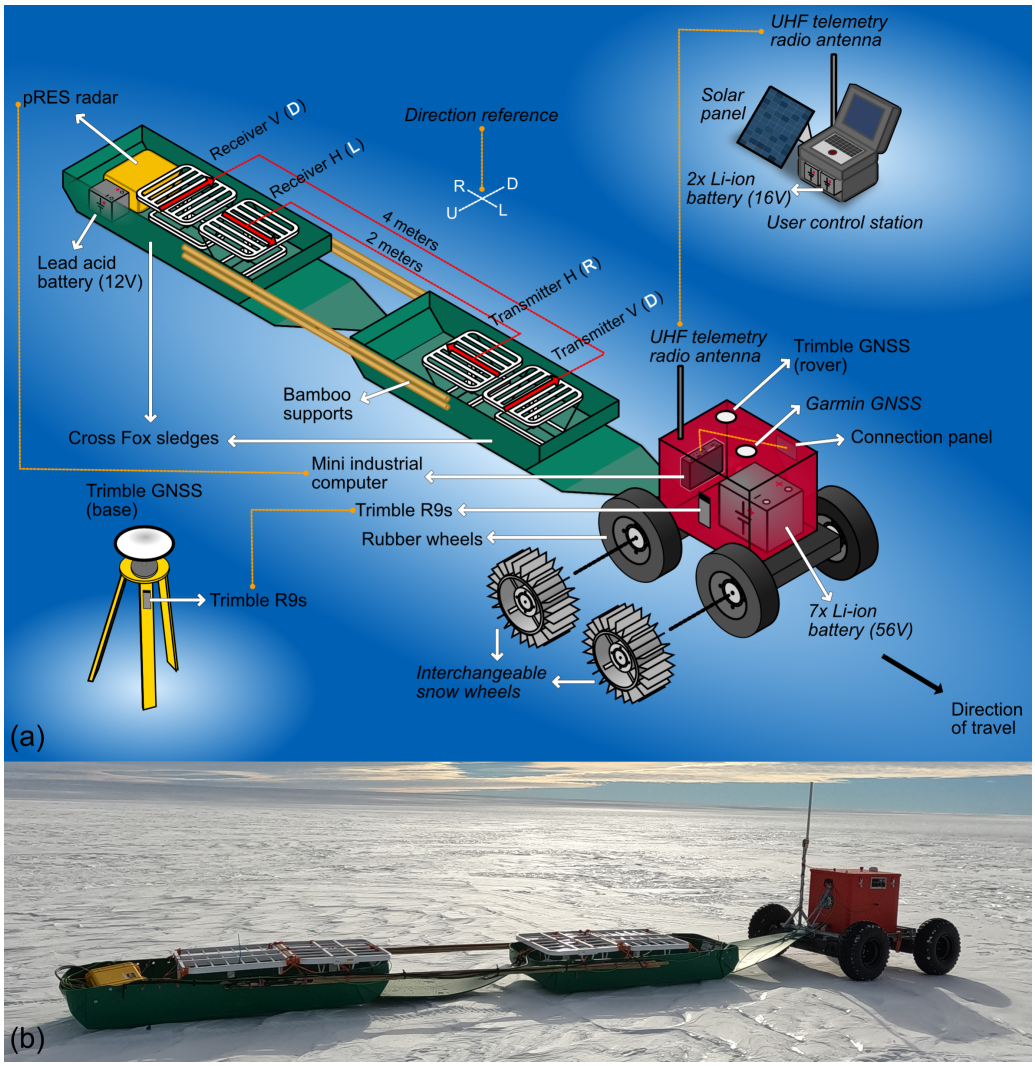

Figure 4.1: Schematic of SLEDGE. The red arrows on the radar antennas show the direction of the electrical field. The dashed yellow lines represent the communication between the two devices. Note that the figure is not to scale. The UHF telemetry and the rover (incl. wheels, power supply and driving system) are provided by Polar Research Equipment.

battery run time of over six hours. Within a waterproof and insulated enclosure are the rover's electronics, motor controllers, and batteries, while the radio and GNSS antennas are externally mounted (Fig. 4.1).

The control station associated with FrostyBoy is a Windows computer equipped with essential peripherals, radio transceiver, and antenna. It operates on a power supply provided by two Li-ion batteries, offering a $\sim$16V voltage output that can be replenished through solar charging.

The entire control station setup is enclosed within a waterproof case to ensure protection. Effective communication (up to 7 km line of sight) between the control station and the rover is facilitated by a 900 MHz radio modem, enabling the transmission of commands from the operator to the rover and real-time telemetry data at the control station. The real-time GPS shown in section C uses its own communication link.

For SLEDGE, we implemented some hardware and complete software changes to FrostyBoy. We added an industrial-grade mini-computer that includes all the necessary input-output and communication ports. This reduces the necessity for additional electronic components with the cost of some rewiring. We kept the Arduino board due to its flexibility for communication with the motor controllers. Although adding an industrial-grade mini-computer increases power consumption, it enables the use of Robotic Operating System version 2 (ROS2) - Foxy (Macenski et al., 2022) as a standardized option for hardware communications providing an interface to a suite of external sensors (Appendix 8.1). To facilitate external access to all the available ports without compromising the rover's internal electronics, we incorporated a dedicated ports panel on the true left side of the rover. This panel enables direct connection of external devices, such as radar systems, a secondary GNSS system, cameras, lights, and display, to the main computer.

While the hardware of the control station remains unchanged, we have developed a new MATLAB® Graphical User Interface (GUI) (Appendix 8.2). Through the new GUI, the operator can communicate with the rover, switch between navigation systems, manually control the radar, and design different types of radar surveys.

4.2.3 GNSS-based Navigation

SLEDGE connects to two GNSS systems simultaneously and chooses between them from the control station based on the type of survey. FrostyBoy came with a standard 19x HVS Garmin® GNSS unit mounted on top of the rover suitable for a survey where a sensor-limited positional accuracy of 3 m can be tolerated. However, to achieve the sub-dcm positioning for SAR surveys we used a Real-Time Kinematic (RTK) GNSS unit including two antennas and receivers (base and rover). Having a receiver connected to each GNSS antenna is necessary since the accurate positions are calculated relative to a coarsely determined base station location and transmitted to the rover receiver for corrections via radio connection (403-473 MHz) resulting in improved positioning accuracy (8mm horizontal, 15mm vertical). The base antenna and its receiver are positioned on a tripod (fixed position) while the rover antenna and its receiver are mounted on the top and right side of the rover, respectively. A range of 1 km line of sight is required in order to maintain the radio connection between the base and the rover. A signal booster (repeater) between the base and rover can be used if longer distances are necessary.

4.2.4 Polarimetric pRES Measurements

In the SLEDGE setup, we integrated a polarimetric version of pRES radar (Brennan et al., 2014; Nicholls et al., 2015) developed by the British Antarctic Survey (BAS) and University College London (UCL). The pRES transmits a linear, frequency-modulated continuous wave (FMCW) chirp with a frequency bandwidth of 200 MHz, centered at 300 MHz. It employs linearly polarized skeleton slot antennas, which exhibit peak directivity in the nadir (ice-facing) direction. To enable polarimetric measurements and avoid the need for mechanical rotation of the antennas, multiplexers were installed at the transmitter output and receiver input to select pairs of antennas with desired polarization characteristics. Because the antennas are multiplexed, rather

than unique channels, measurements from each transmit-receive pair are recorded sequentially which results in an increased observation time of several seconds proportional to the number of antenna combinations at each site. While a total of four antennas (2 times Tx, 2 times Rx) are used in experiments described here, this is extendable to a total of 8 transmit and 8 receive antennas. To facilitate pRES measurments at pre-defined locations, we integrated the pRES into the SLEDGE setup by mounting it, along with its antennas, inside two plastic sleds located at the rear of the rover (Fig. 4.1). The pRES box and antennas were fixed securely within the sleds using a rope and connected to the back of the rover for ease of towing. Communication between the pRES and the rover's computer is facilitated by a wired Ethernet link and HTTP REST API, which allows for the radar to be triggered at pre-defined waypoints, real-time configuration of the radar receiver settings, and backup of recorded measurements to the rover's computer.

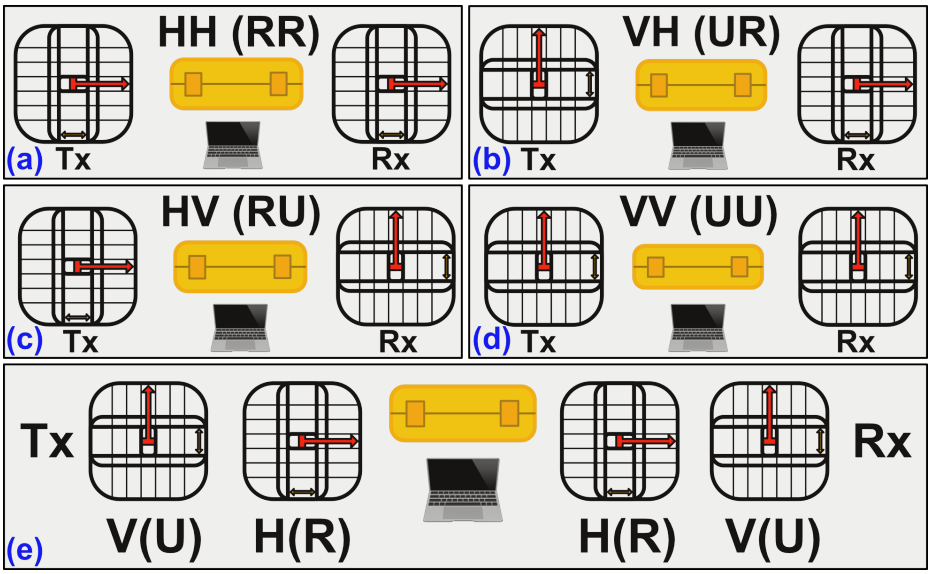

Figure 4.2: Schematic bird-eye view of pRES antenna configuration. (a-d) shows the step-by-step rotation for two antenna measurements and (e) shows the MIMO mode.

The orientation of the pRES antennas is important because the propagation velocity of the electromagnetic wave in ice is orientation-dependent (Hargreaves, 1977, 1978; Dall, 2010). This information is used for polarimetric data processing and ice-fabric analysis. Following notation used in satellite remote sensing literature, we refer to the two orthogonal polarizations as horizontal (H) and vertical (V) based on the orientation of their electric fields (E) relative to the aerial line connecting the Tx and Rx. We consider the electric field parallel to the aerial line as H polarization and the field perpendicular to the aerial line as the V polarization, although both polarizations lie in the horizontal plane. If the electrical field in the trasnmitter and receiver are perpendicular to each other, we refer to this as cross-polarization (HV or VH) otherwise it is co-polarization (HH or VV).

The full polarimetric response of the radar signal can be synthesized out of three (ideally four) measurements including the pairs HH, VV, and HV or VH as they are ideally the same (Ershadi et al., 2022b). In practice, these measurements can be collected in different ways depending on the polarity of the individual antennas. For the pRES antennas, the antenna polarity

is uniquely determined by the directivity of the cable feeds (Fig. 4.2). We therefore suggest that the direction of the cables is recorded during data acquisition so that HH corresponds to right-right (RR) meaning that antenna cables are pointing rightwards relative to a pre-defined direction (e.g., the ice-flow direction or geographic North). All other measurements follow this terminology (i.e., HV corresponds to right-up and so on). This terminology can also be applied in case only two antennas are available, so that the synthesis is achieved by counter-clockwise rotation of individual antennas (Fig. 4.2 a-e). We have found that a flipped antenna orientation (which corresponds to a 180-degree phase shift) may sometimes remain unnoticed in the post-processing and consequently lead to errors in determining both ice-fabric strength and the direction of the principal axis. In case the antennas require a different positioning, as was the case for this study due to cables length, then the phase needs to be corrected by 180 degrees (i.e. corresponding to a multiplication of the complex signal with -1) prior to further post-processing.

4.3 First Deployment Outcome

4.3.1 Study Area

This study showcases a proof-of-concept dataset derived from a 23 km long quad-polarimetric profile autonomously collected within the described setup. The dataset spans the grounding-zone of the Ekström Ice Shelf (Fig. 4.3), and was gathered with the logistical support of the Neumayer III station (Wesche et al., 2016b). First deployment and initial testing was done next to the station. Subsequently, the rover was transported to the grounding line of the Ekström Ice Shelf, located approximately 120 km south of Neumayer III, initiating the data collection phase across the grounding zone (Fig. 4.3).

4.3.2 Data Acquisition

In January 2022, SLEDGE collected two profiles of quad-polarimetric pRES data ($\sim$ 450 points) over an operational period of approximately 20 h (Table 4.1). This includes handling problems such as getting blocked by oversized sastrugi. Such problems were handled by the operator who was typically within 3 km range. This profile used the rubber wheel-setup (section 4.3.4) with a pRES configured to collect all four polarizations with 10 stacks and 40 sub-bursts. The total measuring time at each location was approximately 1 minute. The rover was operated at a speed of 1 m/s which is approximately one third of the maximum speed.

Table 4.1: SLEDGE operational time.

Date	Start	Finish	Duration [h]	Profile
03.01.2021	17:00	22:00	5	Along flow
04.01.2021	14:00	18:30	4:30	Along flow
05.01.2021	14:30	21:00	6:30	Along flow
06.01.2021	12:00	12:30	00:30	Along flow
06.01.2021	14:00	16:00	2	Across flow
06.01.2021	20:30	21:30	1	Along flow

The first profile is oriented along flow and extends over 18 km from A26 to $\sim$2 km before

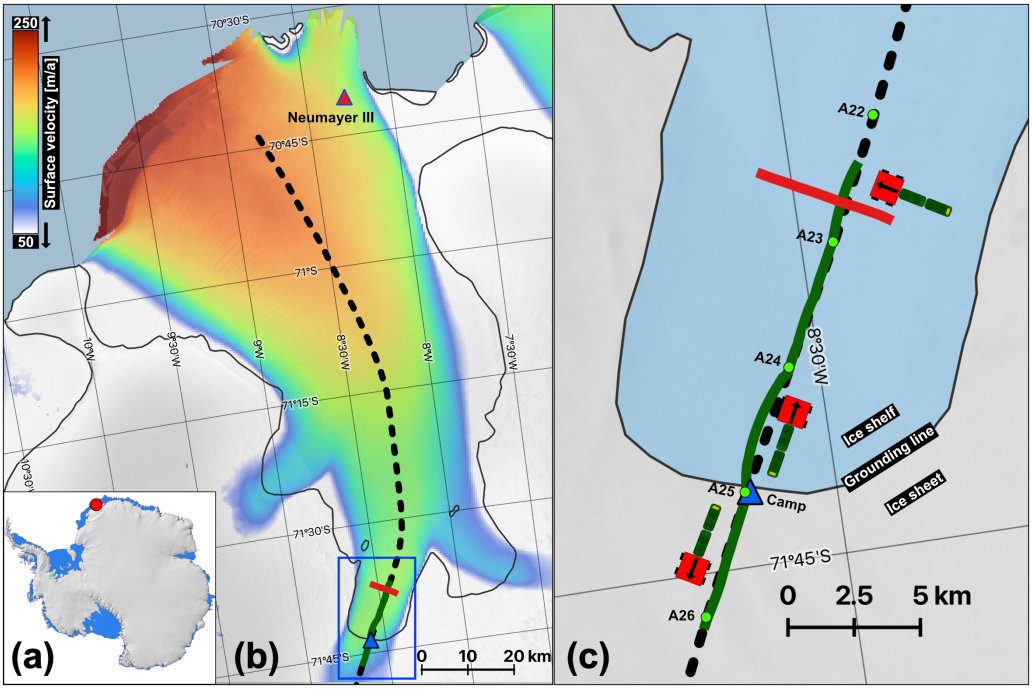

Figure 4.3: (a) Location of Ekström ice shelf in Antarctica. (b) Surface flow velocity in Ekström ice shelf. The red triangle is the location of Neumayer station and the blue triangle is the location of the camp at the grounding line. (c) Location of the radar profiles at the grounding line. The blue area is the Ekström Ice Shelf, separated from the ice sheet (gray area) by the grounding line (solid black line). The green and red profiles are the SLEDGE collected data along and across the ice flow, respectively. The schematic of the rover shows in which direction the data were collected.

A22 (Fig. 4.3c – green line). The radar trace spacing between points A26 to A25 was 20 m, and 100 m elsewhere. The second profile extends in the across-flow direction (perpendicular to the A23-A22 profile) with 100 m trace spacing throughout (Fig. 4.3c – red line). We have also collected a 800 m profile at 1 m spacing (6 operational hours) with a lower-frequency version of the pRES (20-40 MHz) using the RTK positioning system. Results of this will be reported elsewhere.

The first section (∼1 km) of the 20 m spacing profile (Fig. 4.3c, A25 to A26) suffers from oscillating positioning errors relative to the pre-defined locations with approximately ± 5 m (Fig. 4.4a). The source of this mismatch was linked to a wrongly initialized heading direction which was locally defined between the 20 m postings. Even a small angular uncertainty leads to an instable navigation in the case. This is improved when a single heading is defined using the far-end turning point of the profile. The spacing of individual radar measurements can then be defined using that heading and the along-track distance. The difference between both modes is evidenced in Fig. 4.4a where, by mistake, local headings were used for the first kilometer of the along flow profile. Changing the heading direction to the end of the profile reduced the positioning error with few exceptions (Fig. 4.4b) in strongly undulated terrain which we discuss

further in section 4.3.4. The same holds for the positioning at 100 m spacings both in along and across flow (Fig. 4.4c). An exception here occurs at waypoint A25 due to a wrong coordinate entry by the operator. For the bulk part of the profile, the deviation of observed positioning mismatch from the target is 1.2 $\pm$ 1.4 m (mean and standard deviation) which is within our expectations when operating the rover without the RTK. This will not impact the interpretation of the polarimetric radar data.

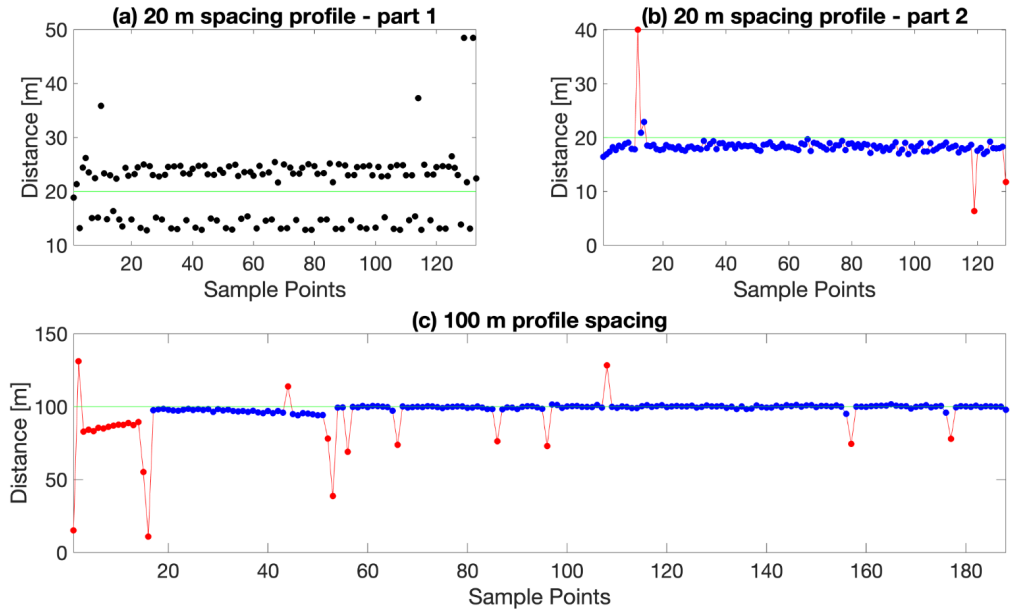

Figure 4.4: The distance between two adjacent pRES measurement points. (a) First 1 km of the 20 m spacing target. (b) Rest of the 20 m spacing profile. (c) All the points with 100 m spacing target. The green lines are the target spacing. All the data in (a) and all the red points are the external problems and were neglected for the mean and standard deviation calculations. Note that (a) and (b) showing the data from A26 to A25 profile in Fig. 4.3 and (c) shows all the data collected along and across flow in 100 m spacing.

Due to spatial limitations in the sleds and length of the cables, the polarimetric data were collected in non-standard mode (Fig. 4.1) which requires the 180-phase correction on HH and HV (see sec. 4.2.4). After that, each trace underwent polarimetric standard processing outlined by Ershadi et al. (2022b). That means that for each location the standard ice-thickness (and in parts internal stratigraphy) product is supplemented with the full orientation dependence from which the ice-fabric types can be reconstructed. This is a significant step forward compared to a manual deployment of the antennas where typically only a few tens of measurements can be collected in about 20 h (compared to 450 using SLEDGE).

4.3.3 Showcasing the Collected Data

Here we show the quad-polarimetric dataset and highlight the potential for further scientific application. In all profiles, the ice-bedrock and ice-ocean interfaces can clearly be detected also

including the transition of the grounding zone (Fig 4.5a). Internal reflection horizons are equally apparent, particularly in the 20 m spacings. In that sense SLEDGE provides similar results as pulsed ground-based radar systems in this area, albeit it requires a much longer acquisition time.

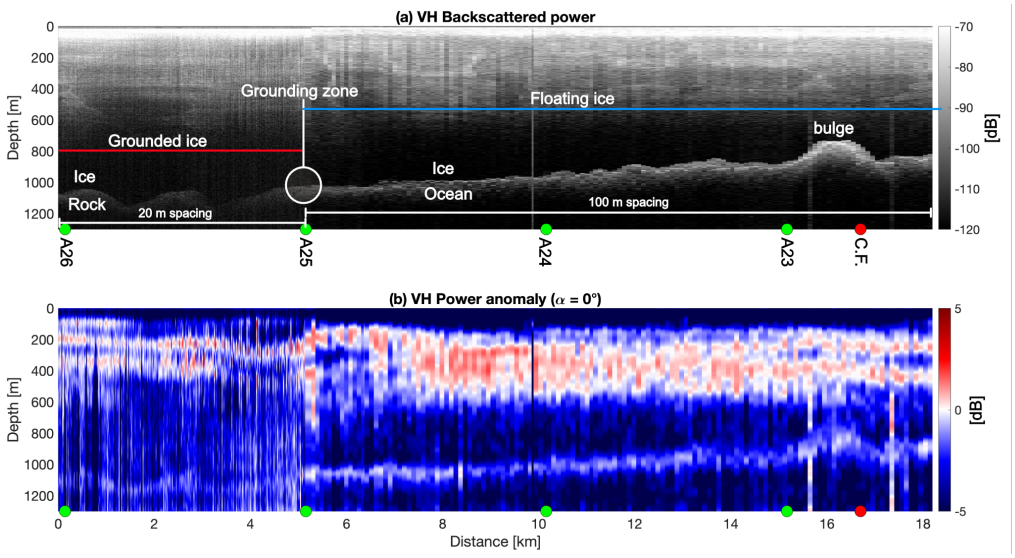

Figure 4.5: Recorded data along the flow profile illustration the backscattered power and cross polarized power anomaly both for VH antenna combination. Note that the red circle marked as C.F. shows the location of the across flow profile.

The added value of SLEDGE becomes apparent when evaluating the quad-polarimetric response which can be shown in different metrics such as backscattered power, power anomalies, coherence phase and its depth gradient. The backscattred power reveals the basal structures in all antenna combinations but with variable basal reflection amplitudes (Appendix - Fig. 8.2, e.g, VH backscattered power shows a stronger contrast). The large-scale basal structures are the same for all polarization combinations, but at a trace-by-trace level differences occur that, at least in part, also image variable basal roughness due to the polarization dependent antenna footprint. Independent of backscattered power, we apply standard quad-polarimetric radar processing at each trace which is sensitive to the dielectric anisotropic and hence birefringent properties of ice. The coherence phase describes the correlation between the two co-polarized signals (HH and VV) and its depth gradient is indicative for the magnitude of ice fabric anisotropy (Jordan et al., 2019, 2020). Power anomalies, which result from the constructive and destructive superposition of the ordinary and extra-ordinary waves, are used to infer the reflection ratio between layers (co-polarized power anomaly) and horizontal ice-fabric orientation (cross-polarized power anomaly). This enables the detection of depth-dependent ice-fabric types, both in terms of strength and orientation, in many flow regimes (Ershadi et al., 2022b).

The full azimuthal illustration of the polarimetric response at each trace in both along-flow and across-flow profiles is shown in the Appendix 8.4 (Fig 8.3). The inference of ice-fabric patterns, including travel time analysis (Zeising et al., 2023) and inversion (Ershadi et al., 2022b) will be done in a different study. Here, we restrict ourselves to demonstrate the VH backscatter

power (Fig. 4.5a) and the VH backscattered power anomaly extracted at an angle ($\alpha = 0$) parallel to the profile direction (Fig. 4.5b). Small values (i.e., the blue colors in Fig. 4.5b) indicate that one of the horizontal ice-fabric's principal axes is oriented along-flow. At shallower depths (i.e., the red colors) this is not the case, and we infer that the ice-fabric is rotated in this depth interval by approximately 45 degrees (Appendix 8.4 (Fig 8.3)). This effect becomes progressively stronger just downstream of the landward limit from the grounding zone. The coherence phase shows a strongly depth-variable gradient with multiple nodes throughout the profile. This pattern is comparable to other locations with significant ice flow (e.g., the EDML ice core site (Ershadi et al., 2022b)) and a stronger ice anisotropy as would be expected at, e.g., ice domes. Detecting such along-flow changes over many kilometers at 100 m spacings offers new possibilities for ground-based radar-polarimetric surveys which are of interest for ice-shelf (Lilien et al., 2023) and ice-stream shear margins (Young et al., 2021; Gerber et al., 2023).

4.3.4 Operational Challenges and Recommendations

The rover is equipped with two wheel sets. The first, metal blade wheels, are tailored for snow surfaces, preventing submersion in soft snow (Fig. 4.6b) and enhancing traction on medium-sized sastrugi. However, in near-melting temperatures, snow accumulation inside and outside the wheels can lead to immobilization (Fig. 4.6a). In such conditions, the second set of rubber wheels performs better. Larger sastrugi (∼50 cm vertical) can also immobilize the rover due to sled weight (Fig. 4.6c), and this was the biggest challenge preventing full autonomous operation.

The current transmission lacks sufficient torque to navigate sastrugi, especially when maneuvering the rover rapidly at sub-meter intervals and making frequent start-stop switches, crucial for scientific applications like SAR processing. To address this, a more robust transmission that delivers increased torque can effectively alleviate this issue. To ensure the rover maintains a straight trajectory toward its destination (Fig. 4.6d), revising the autonomous navigational algorithm along with adding a magnetometer sensor as a compass and direct feedback from rotary encoders on the wheels are recommended.

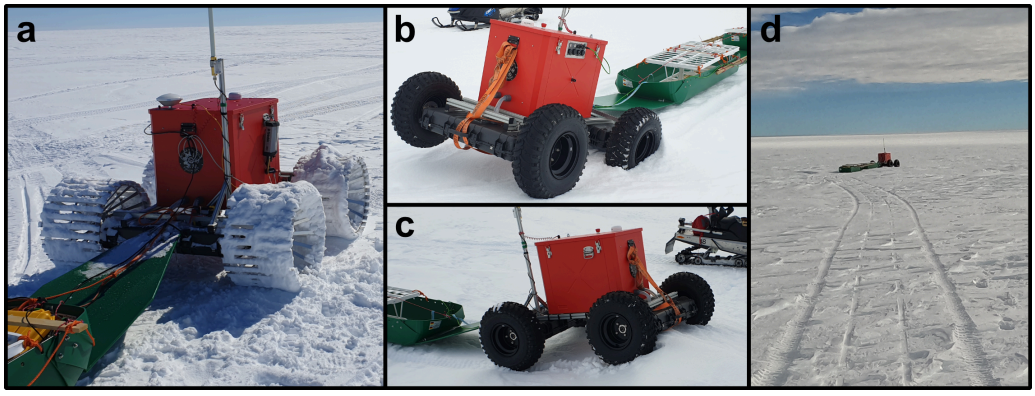

Figure 4.6: (a) Substantial accumulation of snow on metal wheels. (b) The rover sinking into soft snow with rubber wheels. (c) The rover facing difficulties traversing sastrugi. (d) The rover starting to deviate from the straight line.

The pRES system, not designed for rapid movement, experiences frequent Ethernet port disconnections, especially after traversing sastrugi. This can be improved by adding WIFI module to the pRES for wireless communication. Furthermore, the sleds used in deployments lacked brakes, resulting in occasional collisions with the rear of the rover. This can be prevented with including shock absorbers at the rover's rear. The sum of technical shortcomings and the difficult terrain with soft snow and frequent sastrugis prevented us to successfully deploy SLEDGE fully autonomous in overnight surveys. However, we believe that this will be possible in the future once the suggested improvements are implemented, and thus offer field teams another time efficient method of data collection.

4.4 Conclusion

The integration of a phase-coherent, quad-polarimetric radar with an autonomous rover, demonstrated in a proof-of-concept study in Antarctica, shows the system's capacity to collect quad-polarimetric data along extensive profiles, spanning up to 23 km in just 20 operational hours. This system now allows ground-based quad-polarimetric profiles to be collected at spacings previously unattainable. We've demonstrated this with transects in the grounding zone of the Ekström ice shelf. We suggest that the ice is more anisotropic compared to comparable measurements at the ice interior, and the ice-fabric direction rotates in some depth intervals across the grounding zone.

While presenting promising results, our first deployment observations highlight areas for improvement in future deployments. The most crucial ones, causing the most interruptions in data acquisition and requiring attention in the next deployment, are adjusting the transmission providing more torque to navigate larger sastrugi, revising the autonomous navigational algorithm, and ensuring a reliable network connection between pRES and the rover.

Looking ahead, SLEDGE's versatility opens possibilities for attaching other radars or geophysical sensors, such as magnetic, gravimetry, and electric sensors, broadening its applicability beyond ice-fabric anisotropy studies.

Chapter 5

Conclusion & Outlook

5.1 Synthesis of Major Findings

In the introduction, I highlighted the importance of ice fabric anisotropy in ice rheology, directly impacting ice flow behavior. Most ice flow models treat ice as isotropic, posing challenges in accurately predicting Antarctica's impact on sea level rise and climate change due to the lack of observations on spatial changes in ice fabric anisotropy and model complexity.

The main goal of my doctoral research was to address this gap by answering two primary research questions. The first question entailed the development of a data processing method to estimate ice fabric properties utilizing quad-polarimetric pRES radar data. The second question revolved around the design of a rover-based autonomous system, capable of collecting quad-polarimetric pRES data at predetermined locations along extended profiles spanning several kilometers.

Each chapter of my thesis contains a detailed discussion and conclusion specific to that chapter. Here, I refrain from redundancy, aiming to encapsulate key discoveries and achievements related to the primary motivation and research questions. Finally, I finish this thesis with a general outlook and suggestions for future advancements for those interested in continuing this line of work.

5.1.1 How can a method be developed to estimate ice fabric properties from quad-polarimetric pRES radar data?

To answer this question, in the first part of Chapter 2, I concentrated on formulating a non-linear multivariable inverse methodology to estimate the magnitude and orientation of horizontal ice fabric anisotropy within the ice column using quad-polarimetric pRES data. Subsequently, in the latter part of chapter 2 and throughout chapter 3, I applied this method to three distinct flow regimes in Antarctica, where I could compare my results with observations from nearby ice cores. Here are my primary findings concerning the first research question.

Estimating Ice Fabric Properties from quad-polarimetric pRES Data

Chapters 2 and 3 showcase the successful application of the developed inverse approach in deriving the magnitude $\Delta\lambda_H$, orientation ($\mathbf{v_1}$ & $\mathbf{v_2}$), and reflection ratio (r) of horizontal ice fab-

ric anisotropy from pRES radar data collected using a quad-polarimetric antenna combination. However, accurate estimation require adherence to two key assumptions.

The first assumption pertains to the orientation of the eigenvectors in space. Given that the nadir pRES signal exclusively identifies horizontal anisotropy, it necessitates one eigenvector in the vertical direction and the other two in the horizontal plane. Failure to meet this condition results in errors within the estimated horizontal anisotropy values, directly linked to the tilt angle of the vertical eigenvector as studied by Jordan et al. (2019); Rathmann et al. (2022) (*more on this in the outlook*).

The second assumption directly relates to the orientation of horizontal ice fabric ($\mathbf{v_1}$ & $\mathbf{v_2}$). My observations indicate that variations in fabric orientation with depth lead to complexities in reproducing the backscattered signal through the inverse approach, resulting in multiple potential solutions. Therefore, the inverse approach excels in estimating fabric properties when the fabric orientation remains relatively constant throughout the ice column, ensuring minimal variation in v1 and v2 with depth (*more on this in the outlook*).

Ice Fabric Full Orientation Tensor Approximation

The radar antenna's georeferenced positioning during data acquisition allowed for an inverse approach to estimate the georeferenced horizontal ice fabric orientation ($\mathbf{v_1}$ & $\mathbf{v_2}$). In Chapter 2, I contrasted this estimated orientation with the direction of the surface maximum horizontal strain rate, derived from GPS data. Chapter 3, employed the same approach, but in the absence of GPS data, the comparison was made with the horizontal strain rate orientation calculated from the shallow ice approximation. This led to a consistent alignment of one of the depth-averaged horizontal eigenvectors with the direction of the strongest horizontal strain rate (*more on this in the outlook*). This finding is significant as methods like satellite and GPS can only measure the horizontal strain on the surface, while gauging deeper strain remains a challenge, typically achieved by assessing ice deformation in an ice core using a well logger. The correlation of the horizontal ice fabric's orientation with the strongest strain rate direction on the surface allows for an estimation of the same in the deeper ice column, providing insights into the stress dynamics experienced by the ice in the study area.

The inverse approach could estimate the horizontal ice fabric anisotropy $\Delta\lambda_H$, but not the full orientation tensor (λ_1, λ_2 and λ_3). However, I discovered that it is possible to successfully approximate the full orientation tensor in an additional step using the estimated parameters from the inverse method. This technique has a top-to-bottom approach and requires $\Delta\lambda_H$ from two adjacent layers and the reflection ratio between them (r), starting from the top and assuming that the ice is isotropic ($\Delta\lambda_H = 0$) in the first layer.

I my opinion, this is a novel technique and the most significant achievement of my doctoral research. The ability to estimate the magnitude of all the three eigenvalues and the georeferenced fabric orientation within the ice column is a crucial step towards understanding the type of stress the ice has experienced and parametrizing ice fabric anisotropy into anisotropic ice flow models.

Ice Fabric Anisotropy Revealed Raymond Effect

The detection of Raymond arches through radargrams indicates the ice dynamic stability in ice domes and ice rises. The absence of these arches raises questions about the area's ice dynamic status. Previously model predicted that spatial changes in ice fabric anisotropy can reveal the Raymond effect in ice rises and ice domes (Martín et al., 2009a).

In this regard, in chapters 2 and 3, I estimated the ice fabric anisotropy on two pRES radar profiles: a 36 km profile on a dome area (DC) where radargrams did not detect Raymond arches, and a 5 km profile on a triple junction ice rise (HIR) where radargrams detected Raymond arches. Although, the spatial change of the estimated ice fabric anisotropy in these two profiles displayed varying degrees of anisotropy it showed a similar pattern in both profiles. Deeper sections of the ice column exhibit stronger ice fabric anisotropy under the dome compared to its fanks. Furthermore, in Chapter 3, I compared the estimated ice fabric anisotropy with an ideal ice rise model (Martín et al., 2009a).

The conducted analyses not only validate the model prediction but also for the first time, particularly in DC, demonstrate the observation of the spatial distribution of ice fabric anisotropy, is capable of detecting Raymond effect even when the Raymond arches are not formed yet (young dome). This proves the Raymond effect is presence in ice fabric anisotropy.

This implies that comparing the estimated spatial change in ice fabric anisotropy across a dome/ice rise (utilizing a quad-polarimetric pRES profile) with models can assess the current ice dynamic status in the area. Furthermore, in areas like HIR with a complex flow regime (triple junction), a three-dimensional observation of ice fabric anisotropy can enhance the optimization of models and contribute to understanding the area's ice dynamic stability.

The Importance and Effectiveness of Quad-Polarimetric Data

Theoretically, the full azimuthal backscattered pRES signal could be synthesized through only four individual measurements utilizing a quad-polarimetric approach (HH, HV, VH, and VV). Nevertheless, real data had not previously validated this proposition. In Chapet 6 (Sect. 6.5), I employed actual pRES data collected at 22.5° intervals for all combinations, demonstrating that quad-polarimetric data for a single direction suffices to replicate the full 180-degree azimuthal signal (*more on this in the outlook*). This holds significance in expediting pRES data collection for fabric analysis and the development of an autonomous system, as it eliminates the need for antenna rotation, thereby minimizing human error associated with antenna rotation.

Furthermore, in a related topic, I observed that a 180-degree rotation in the antenna during data acquisition induces a 180° phase shift on the collected signal. While this shift does not impact the detection of basal melt rate, it significantly affects the synthesis of the full azimuthal signal when employing quad-polarimetric data to estimate ice fabric properties. This discrepancy can lead to erroneous estimations of both magnitude and orientation of the ice fabric anisotropy. Therefore, as detailed in chapter 4 (Sect. 4.2.4), I recommended a data acquisition methodology for gathering quad-polarimetric pRES radar data in the field, aimed at circumventing the phase reversal issue.

5.1.2 How can an autonomous rover be designed to collect quad-polarimetric pRES radar data at predetermined locations?

Regarding this research question, as highlighted in chapter 4, I developed an autonomous rover-based system (SLEDGE) that pulls the pRES radar and four antennas capable of collecting data in quad-polarimetric mode at predefined locations for several kilometers. Subsequently, I conducted a proof of concept by collecting data with SLEDGE in the Ekström ice shelf grounding zone in Antarctica.

23 km Quad-Polarimetric pRES Data Collected in 20 Hours

In my opinion, the key outcome regarding this research question is the SLEDGE itself, the successful proof of concept and the insights acquired during the first deployment, focusing on enhancements for future deployments (*more on this in the outlook*). The significant achievement regarding this research question involved successfully collecting 450 measurement points in quad-polarimetric setup, covering 23 km profile within 20 operational hours. Previously, only a few tens of points could be measured in the same time frame. Additionally, utilizing the accuracy of the RTK GPS mounted on the rover, I successfully gathered 1 km of pRES data with 1 m spacing, showing that SLEDGE is capable of collecting data with high positioning accuracy suitable for other applications (e.g., SAR processing).

The data collected with SLEDGE has shown potential to reveal changes in ice fabric anisotropy from grounded to floating ice, providing a basis for radar-polarimetry in studying ice-stream formation and anisotropic modeling. Moreover, the system's modular design suggests adaptability beyond the pRES radar and ice fabric anisotropy (*more on this in the outlook*).

5.2 Research Perspectives

In this section, I concentrate on the topics that remained unexplored and hold potential for further investigation.

Machine Learning Algorithms Instead of Classical Inverse Approach

My developed inverse approach effectively estimated ice fabric properties in three distinct flow regimes in Antarctica. However, it has two limitations commonly encountered in classical inverse approaches, requiring further investigation and improvement.

The first limitation is the approach's high dependence on initial model parameters. To achieve a successful inversion, a precise initial guess about ice fabric properties is essential, posing a challenge, especially when inverting several hundred data points. The second limitation is that the inverse approach works best for depth-invariant ice fabric orientation. If the orientation of the ice fabric rotates with depth, the backscattered signal becomes complex, and the inverse approach struggles to detect a unique solution.

To overcome both limitations, I recommend enhancing the current inverse approach by replacing the classical method with a machine learning algorithm (e.g., simulation based inference). This shift can significantly aid in pattern detection. Additionally, machine learning can be more applicable by enabling it to analyze an entire profile rather than a singular point, estimating ice fabric properties and generating two-dimensional results without dependence on the initial guess of model parameters.

The Effect of Tilted Vertical Eigenvector

The first constraint is when one of the eigenvectors is not aligned vertically which cause error in estimating horizontal anisotropy. While it is technically feasible to rectify this error if the extent of the tilted eigenvector is known (Jordan et al., 2019; Rathmann et al., 2022), the detection of such a tilt remains a challenge in radar data. The primary method to address this issue involves employing wide-angle pRES radar measurements where the transmitter and receiver antenna are several tens of meter far from each other.

This topic has substantial potential to improve the assessment of ice fabric anisotropy using pRES radar data by addressing its current limitation. In my view, it is worthwhile to explore

the direct detection of the tilt degree in the vertical eigenvector from nadir pRES data. This can be achieved by observing the impact of the tilted eigenvector (calculated from wide-angle data) on polarimetric metrics. If the influence of the tilted eigenvector is discernible in observations from nadir pRES data, there may be a need and opportunity to extend Fujita's forward model (Fujita et al., 2006).

In the same context, it is crucial to comprehend the impact of a tilted eigenvector on pRES radar signals, especially concerning quad-polarimetric measurement and its role in synthesizing the complete azimuthal backscattered signal. Additional investigation is required to validate that the tilted eigenvector has no effect on the pRES data synthesized from quad-polarimetric measurements.

Ice Fabric Analysis - Easy Access for the Community

As the quantity of collected quad-polarimetric pRES data increases, I suggest establishing a website/software with friendly user interface where researchers can simply upload their pRES data in the correct format. This website/software would then process, plot and invert the data. Finally, utilizing AI, it generates a report about the ice fabric properties derived from the provided data. This method holds the potential to notably enhance the quantity of the existing observation and understanding of ice fabric properties.

Horizontal Strain Orientation in Deeper Ice

I observed a consistent pattern in three distinct study areas: the estimated eigenvector in the horizontal plane typically aligns with the direction of the strongest horizontal strain rate. However, this eigenvector is not consistently the same across all areas. In my findings, I noted that in DC and EDML, where the flow is less complex compared to HIR (a triple junction ice rise), the strongest horizintal eigenvector ($\mathbf{v_2}$) aligns with the direction of the strongest horizontal strain rate, whereas in HIR, it's $\mathbf{v_1}$. While this inconsistency might be attributed to different flow regimes in these study areas, it is crucial to investigate this discrepancy and establish a reliable correlation between the estimated ice fabric orientation and the direction of the horizontal strain rate. This correlation could provide valuable insights into the deeper ice column's rheology.

SLEDGE, Further Developments and Applications

In my suggestions for further developing SLEDGE, relevant information is available in chapters 4 and 8. Now, I will outline necessary changes for SLEDGE before another field deployment.

One persistent issue in data acquisition was the pRES radar disconnecting from the rover's computer due to a long ethernet cable from pRES to the rover. As the pRES is designed for stationary measurement, maintaining the ethernet connection while driving over sastrugi is unfeasible. Considering the rover computer's WIFI capability, I recommend mounting a WIFI module to pRES for a wireless connection between pRES and the rover.

Frequent interruptions occurred due to the rover getting stuck with sastrugi. To enhance field data acquisition and minimize issues with sastrugi, I propose changing the current transmission to provide more torque for the rover to navigate sastrugi. Additionally, a revision of the autonomous drive algorithm is advised. The main problem observed in the current algorithm was the rover deviating from a straight line and circling around the destination point when in close range. Although I addressed this temporarily, a thorough revision of the autonomous driving algorithm is recommended.

Before data collection, minor recommendations include ensuring the use of the proper wheel, considering snow conditions and temperature, as discussed in chapter 4. Moreover, before the first data acquisition and after every long traverse, calibrating the engines is crucial. Applying the same current to all four engines and measuring the rotation per minute in each wheel ensures consistent calibration, as discrepancies have been observed.

Finally, the modular design of the rover, both in hardware and software, extends its application beyond the pRES radar and ice fabric anisotropy. Its potential use with other radar systems for purposes like mapping ice bed and internal layers, as well as SAR processing with sub-decimeter spacing using the RTK GPS, is notable. Its adaptability to different geophysical instruments (e.g., magnetic and gravimetry), enhances its versatility for scientific applications. Therefore, I encourage those interested in continuing this work to explore the system's broader potential.

Chapter 6

Supporting information for chapter 2

6.1 ApRES Station Info Table

Table 6.1: ApRES stations info. Coordinates are shown in decimal degrees in the WGS84 reference system. Surface elevations are extracted from the Reference Elevation Model of Antarctica (REMA; Helm et al., 2014). Bed elevations are obtained from the polarimetric-radar data. Tx–Rx azimuth is measured by a compass with $\pm 15^{\circ}$ tolerance.

Site Name	Location	Longitude [DDs]	Latitude [DDs]	Surface elevation [m.a.s.l.]	Bed elevation [m.a.s.l.]	Tx-Rx azimuth [°]
LD01	DML	0.093410	-74.995730	2892.3	206.5	114
EPICA	Dome C	123.350000	-75.100000	3232.7	-8.0	163.6
W18	Dome C	122.909370	-75.000790	3226.9	-119.28	81.2
W12	Dome C	123.071950	-75.035100	3229.0	64.5	64.3
W06	Dome C	123.237540	-75.068530	3232.4	26.0	76.2
W4d5	Dome C	123.280150	-75.076690	3233.1	24.4	69
W2d5	Dome C	123.337480	-75.086960	3233.5	24.8	62.2
W1d5	Dome C	123.366290	-75.092090	3233.5	51.4	69.3
W1d0	Dome C	123.381070	-75.094670	3233.6	64.7	71.9
W0d5	Dome C	123.395540	-75.097190	3233.5	54.45	75.6
E0	Dome C	123.410151	-75.099738	3233.7	36.6	71.5
E0d5	Dome C	123.424700	-75.102290	3233.5	50.5	67.8
E1d0	Dome C	123.439460	-75.104780	3233.5	80.6	61.7
E1d5	Dome C	123.453870	-75.107310	3233.3	109.2	64.5
E02	Dome C	123.468390	-75.109810	3233.1	121.5	73.3
E03	Dome C	123.497900	-75.114910	3232.8	78.0	71.9
E4d5	Dome C	123.541160	-75.122690	3232.27	116.4	65.8
E06	Dome C	123.583990	-75.131010	3231.3	38.0	58.5
E09	Dome C	123.666480	-75.147581	3229.1	38.1	61.4
E12	Dome C	123.748400	-75.164990	3227.2	50.3	57.8
E18	Dome C	123.906540;	-75.201260	3224.8	17.8	70.2

6.2 Matrix-Based Radio Wave Propagation Parameters

Here, we briefly explain the parameters from Eq. (2.3.3). The depth factor in this equation is

$$D(z) = \frac{\exp(jk_0 z)}{4\pi z}, \tag{6.1}$$

where j is the imaginary unit, and $k_0 = 2\pi f_c c_0^{-1}$ is the wavenumber in a vacuum, with c_0 the speed of light in a vacuum.

The transmission of the signal is described by the transmission matrix $\mathbf{T}$ along the ice fabric horizontal principal axes. $\mathbf{T}$ is a function of wavenumbers k_x and k_y , whereas the wavenumbers can be expressed as a function of dielectric permittivities (ϵ'_x, ϵ'_y) and electrical conductivities (σ_x, σ_y) (Fujita et al., 2006).

$$k_x = (\epsilon_0 \mu_0 \epsilon'_x \omega^2 + j\mu_0 \sigma_x \omega)^{0.5}, \tag{6.2}$$

$$k_y = (\epsilon_0 \mu_0 \epsilon'_y \omega^2 + j\mu_0 \sigma_y \omega)^{0.5}, \tag{6.3}$$

where ϵ_0 and μ_0 are the dielectric permittivity in a vacuum and the magnetic permeability in a vacuum, respectively, and ω is the angular frequency. In this study we follow Ackley and Keliher (1979) and Fujita et al. (2006) and assume isotropic electrical conductivity ($\sigma_x = \sigma_y$). Using Eq. (2.3), $\mathbf{T}$ can be written as a function of eigenvalues

$$\mathbf{T}(\lambda 1_i, \lambda 2_i) = \begin{pmatrix} T_x(\lambda 1_i) & 0 \\ 0 & T_y(\lambda 2_i) \end{pmatrix}, \tag{6.4}$$

where it tracks the relative phase shifts induced by the dielectric anisotropy along the ice fabric principal axes. The reflection matrix $\mathbf{\Gamma}$ describes the reflection of the radio waves at an interface with changing dielectric properties

$$\mathbf{\Gamma}(\lambda 1_i, \lambda 2_i) = \begin{pmatrix} \Gamma_x(\lambda 1_i) & 0 \\ 0 & \Gamma_y(\lambda 2_i) \end{pmatrix}, \tag{6.5}$$

A rotation between the TR aerial line and $\mathbf{v1}$ of the ice fabric in layer i is accounted for by the rotation matrix $\mathbf{R}$ and its transpose ($\mathbf{R}'$):

$$\mathbf{R}(\theta_i) = \begin{pmatrix} \cos\theta_i & -\sin\theta_i \\ \sin\theta_i & \cos\theta_i \end{pmatrix}. \tag{6.6}$$

6.3 Matrix-Based Radio Wave Propagation in a Single Layer Case

Here we expand individual components of a single-layer case that are used later to determine the relationship between the anisotropic reflection ratio and the angular distance of the copolarization nodes. For this case, we drop the indices relating to the different layers and expand Eq. (2.3.3):

$$\mathbf{S} = D^2\mathbf{R}(\theta)\mathbf{T}^2\mathbf{\Gamma}\mathbf{R}'(\theta), \tag{6.7}$$

$$\mathbf{S} = \begin{pmatrix} s_{HH} & s_{VH} \\ s_{HV} & s_{VV} \end{pmatrix} = D^2 \begin{pmatrix} T_x^2\Gamma_x\cos^2\theta + T_y^2\Gamma_y\sin^2\theta & \sin\theta\cos\theta(T_x^2\Gamma_x - T_y^2\Gamma_y) \\ \sin\theta\cos\theta(T_x^2\Gamma_x - T_y^2\Gamma_y) & T_y^2\Gamma_y\cos^2\theta + T_x^2\Gamma_x\sin^2\theta \end{pmatrix}. \tag{6.8}$$

so that:

$$s_{HH}(\theta \pm \frac{\pi}{2}) = s_{VV}(\theta), \tag{6.9}$$

$$s_{HV}(\theta \pm \frac{\pi}{2}) = -s_{HV}(\theta). \tag{6.10}$$

The complex s_{HH}, its amplitude, and its phase are then

$$s_{HH} = \frac{1}{(4\pi z)^2}\left(\Gamma_x\cos^2(\theta)\exp(j2zk_x) + \Gamma_y\sin^2(\theta)\exp(j2zk_y)\right), \tag{6.11}$$

$$|s_{HH}| = \frac{\Gamma_x}{(4\pi z)^2}\left(\cos^4(\theta) + r^2\sin^4(\theta) + 2r\sin^2(\theta)\cos^2(\theta)\cos(2z(k_x - k_y))\right)^{0.5}, \tag{6.12}$$

$$\arg(s_{HH}) = \tan^{-1}\left(\frac{\sin(2zk_x) + r\tan^2(\theta)\sin(2zk_y)}{\cos(2zk_x) + r\tan^2(\theta)\cos(2zk_y)}\right), \tag{6.13}$$

respectively. Also, the complex s_{HV}, its amplitude, and its phase, respectively, are

$$s_{HV} = \frac{\sin(\theta)\cos(\theta)}{(4\pi z)^2}\left(\Gamma_x\exp(j2zk_x) - \Gamma_y\exp(j2zk_y)\right), \tag{6.14}$$

$$|s_{Hv}| = \frac{\Gamma_x\sin(\theta)\cos(\theta)}{(4\pi z)^2}\left(1 + r^2 - 2r\cos(2z(k_x - ky))\right)^{0.5}, \tag{6.15}$$

$$\arg(s_{HV}) = \tan^{-1}\left(\frac{\sin(2zk_x) + r\sin(2zk_y)}{\cos(2zk_x) + r\cos(2zk_y)}\right). \tag{6.16}$$

6.4 Polarity of the Coherence Phase Gradient

This section details the relationship between the polarity of the phase gradient and the corresponding directions of the eigenvectors. Care has to be taken here as the deramping during ApRES data acquisition is equivalent to a complex conjugation of the received signal. If this is not accounted for, the inferred eigenvector **v1** and **v2** will be swapped. More specifically, for a received signal at $\theta = 0°$,

$$s_{HH} = A\left(\Gamma_x \cos(2zk_x) + j\Gamma_x \sin(2zk_x)\right), \tag{6.17}$$
$$s_{VV} = A\left(\Gamma_y \cos(2zk_y) + j\Gamma_y \sin(2zk_y)\right), \tag{6.18}$$

so that the coherence phase results in:

$$C_{HHVV} = \left(\cos(2z(k_x - k_y)) + j\sin(2z(k_x - k_y))\right), \tag{6.19}$$
$$\phi_{HHVV}(\theta = 0) = 2z(k_x - k_y), \tag{6.20}$$

and conversely for $\theta = 90°$:

$$\phi_{HHVV}(\theta = 90°) = 2z(k_y - k_x). \tag{6.21}$$

As explained in Appendix 6.2, k_x and k_y are a function of $\lambda 1$ and $\lambda 2$, respectively. Because $\lambda 1 \leq \lambda 2$ it follows that $k_x < k_y$. Therefore, $\phi_{HHVV}(\theta = 0°) < 0$ and $\frac{\phi_{HHVV}(\theta=0°)}{dz} < 0$. The reverse holds for $\theta = 90°$.

6.5 Reconstruction of Azimuthal Measurements from a Single Quad-Polarimetric Acquisition

The transformation is purely geometrical and corresponds to a coordinate transformation into a rotated reference system for an arbitrary γ:

$$\begin{pmatrix} s_{HH}(\theta \pm \gamma) & s_{VH}(\theta \pm \gamma) \\ s_{HV}(\theta \pm \gamma) & s_{VV}(\theta \pm \gamma) \end{pmatrix} =$$
$$\begin{pmatrix} \cos(\theta \pm \gamma) & -\sin(\theta \pm \gamma) \\ \sin(\theta \pm \gamma) & \cos(\theta \pm \gamma) \end{pmatrix} \begin{pmatrix} s_{HH}(\theta) & s_{VH}(\theta) \\ s_{HV}(\theta) & s_{VV}(\theta) \end{pmatrix} \begin{pmatrix} \cos(\theta \pm \gamma) & \sin(\theta \pm \gamma) \\ -\sin(\theta \pm \gamma) & \cos(\theta \pm \gamma) \end{pmatrix}, \tag{6.22}$$

resulting in:

$$s_{HH}(\theta \pm \gamma) =$$
$$\cos^2(\theta \pm \gamma) s_{HH}(\theta) + \sin^2(\theta \pm \gamma) s_{VV}(\theta) - \sin(\theta \pm \gamma)\cos(\theta \pm \gamma)(s_{HV}(\theta) + s_{VH}(\theta)), \tag{6.23}$$

$$s_{VH}(\theta \pm \gamma) =$$
$$\cos^2(\theta \pm \gamma) s_{VH}(\theta) - \sin^2(\theta \pm \gamma) s_{HV}(\theta) + \sin(\theta \pm \gamma)\cos(\theta \pm \gamma)(s_{HH}(\theta) - s_{VV}(\theta)), \tag{6.24}$$

$$s_{HV}(\theta \pm \gamma) = \cos^2(\theta \pm \gamma)s_{HV}(\theta) - \sin^2(\theta \pm \gamma)s_{VH}(\theta) + \sin(\theta \pm \gamma)\cos(\theta \pm \gamma)(s_{HH}(\theta) - s_{VV}(\theta)), \tag{6.25}$$

$$s_{VV}(\theta \pm \gamma) = \cos^2(\theta \pm \gamma)s_{VV}(\theta) + \sin^2(\theta \pm \gamma)s_{HH}(\theta) + \sin(\theta \pm \gamma)\cos(\theta \pm \gamma)(s_{HV}(\theta) + s_{VH}(\theta)). \tag{6.26}$$

Figure 6.1 demonstrates this approach for the EDML site, where quad-polarimetric measurements were additionally complemented by a dataset collected with rotating antennas. There are no structural differences between both datasets.

6.6 Correlation Between HH Power Anomaly (δP_{HH}) Nodes and Anisotropic Reflection Ratio (r)

Here, we quantify the angular distance of co-polarization nodes (AD) as a function of the anisotropic reflection ratio (r). This defaults to a two-dimensional minimization problem in z and θ in the power anomaly δP_{HH}. A co-polarization node in Eq. (6.12) requires

$$\cos(2zk_y) = -1. \tag{6.27}$$

The remaining quadratic equation has two solutions corresponding to the two co-polarization nodes:

$$\theta_{node1} = \tan^{-1}(\frac{1}{\sqrt{r}} + \theta), \tag{6.28}$$

$$\theta_{node2} = \tan^{-1}(\frac{1}{\sqrt{r}} - \theta). \tag{6.29}$$

The angular distance between these nodes then results in

$$AD = |\theta_{node2} - \theta_{node1}| = 2\tan^{-1}(\frac{1}{\sqrt{r}}), \tag{6.30}$$

which can be re-arranged for the reflection ratio as:

$$r = \frac{1}{\tan^2(\frac{AD}{2})}. \tag{6.31}$$

6.7 The Effect of Vertical Insensitivity in Polarimetric Radar

Since polarimetric radar is insensitive to the vertical component of the ice fabric, it is only possible to estimate its horizontal anisotropy from the matrix model alone (Sect. 2.3.3). As shown in Fig. 6.2, the value of $\Delta\lambda = \lambda 2 - \lambda 1$ is not sufficient to infer the ice fabric type. End-member cases in Fig. 6.2a–c are the values for $\lambda 1$, $\lambda 2$, and $\lambda 3$ for an isotropic (I), singlepole maximum (S), and girdle-type (G) ice fabric. Although the uncertainty in detecting the ice fabric type decreases for stronger $\Delta\lambda$, to constrain the ice fabric type from the polarimetric radar, all three eigenvalues along the ice fabric principal axes are necessary. The triangular shape of Fig. 6.2 is due to the constraints on the $\lambda 1$, $\lambda 2$, and $\lambda 3$ values, as mentioned in Sect. 2.3.1.

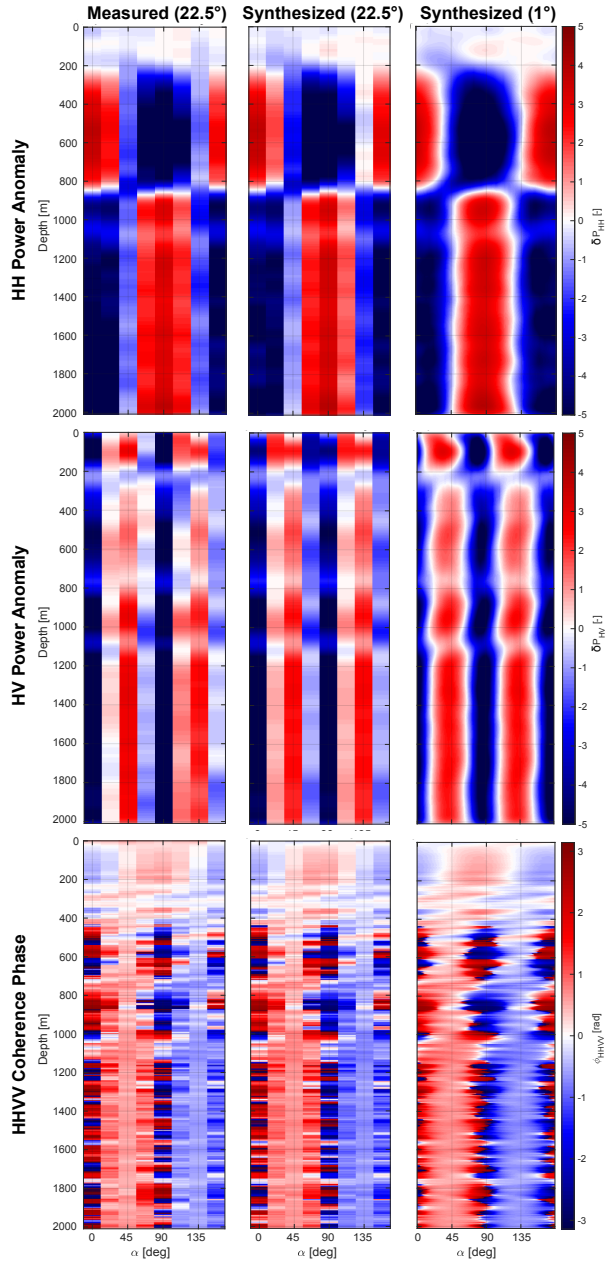

Figure 6.1: Comparison between measured and synthesized ApRES data at the EDML site. Left column: measured ApRES data (22.5° azimuthal spacing). Middle column: synthesized ApRES data (22.5° azimuthal spacing). Right column: synthesized ApRES data (1° azimuthal spacing).

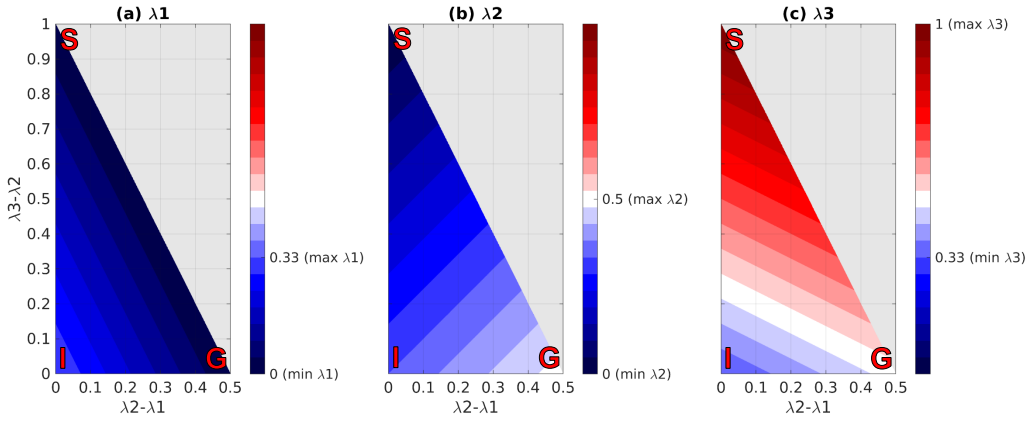

Figure 6.2: Ice fabric type and eigenvalue (a)$\lambda 1$, (b)$\lambda 2$, (c)$\lambda 3$ as a function of eigenvalue differences $\lambda 2 - \lambda 1$ and $\lambda 3 - \lambda 2$. (I) isotropic ice fabric where $\lambda 2 - \lambda 1$ and $\lambda 3 - \lambda 2$. (S) Single-pole maximum ice fabric where $\lambda 2 - \lambda 1 = 0$ and $\lambda 3 - \lambda 2 = 1$. (G) Vertical girdle ice fabric where $\lambda 2 - \lambda 1 = 0.5$ and $\lambda 3 - \lambda 2 = 0$.

6.8 Code and Data Availability

The entire code was written by the author and is publicly available on GitHub (https://github.com/RezaErshadi/ApRES_InverseApproach, last access: 19 April 2022; DOI: https://doi.org/10.5281/zenodo.4447487; Ershadi, 2021). EDML radar data are cited as Christmann et al. (2020) https://doi.org/10.1594/PANGAEA.913719. Dome C radar data are cited as Corr et al. (2021); DOI: https://doi.org/10.5285/634EE206-258F-4B47-9237-EFFF4EF9EEDD.

6.9 Competing Interests

At least one of the (co-)authors is a member of the editorial board of The Cryosphere. The peer-review process was guided by an independent editor, and the authors also have no other competing interests to declare.

6.10 Disclaimer

Publisher's note: Copernicus Publications remains neutral with regard to jurisdictional claims in published maps and institutional affiliations.

6.11 Acknowledgements

M. Reza Ershadi and Reinhard Drews were supported by a DFG Emmy Noether grant (grant no. DR 822/3-1). This publication was also generated in the frame of Beyond EPICA Oldest Ice. The project has received funding from the European Union's Horizon 2020 research and innovation program under grant agreement nos. 815384 (Oldest Ice Core) and 730258 (CSA). It

is supported by national partners and funding agencies in Belgium, Denmark, France, Germany, Italy, Norway, Sweden, Switzerland, the Netherlands, and the United Kingdom. The Dome C measurements were made possible by the logistics provided by IPEV (prog. 902) and PNRA. We thank Luca Vittuari (University of Bologna, Italy) for the positioning of the stakes. The opinions expressed and arguments employed herein do not necessarily reflect the official views of the European Union funding agency or other national funding bodies. This is Beyond EPICA publication number 25. We thank the AWI logistics personnel for support of the work at Kohnen, made available through Alfred-Wegener-Institut Helmholtz-Zentrum für Polar- und Meeresforschung (2016).

6.12 Financial Support

This research has been supported by the Deutsche Forschungsgemeinschaft (grant no. DR 822/3-1) and the Horizon 2020 research and innovation program and coordination and support action (Beyond EPICA (grant no. 815384) and BE-OI (grant no. 730258)). This open-access publication was funded by the University of Tübingen.

6.13 Review Statement

This paper was edited by Adam Booth and reviewed by Thomas Jordan, Emma C. Smith, and one anonymous referee.

Chapter 7

Supporting Information for Chapter 3

7.1 Limitations in Depth of Investigation

In Fig. 7.1, we present the ice thickness and coherence magnitude at the p0 radar site (located at the centre of the profile). As detailed in Section 3.3.1, if the coherence magnitude falls below 0.4 (red zone in Fig.7.1), the signal is considered unreliable for further phase analysis. As depicted in the figure, the coherence magnitude falls below 0.4 at approximately 400 m depth. As a result, for all pRES data analysed in this study, only the top 400 m are used.

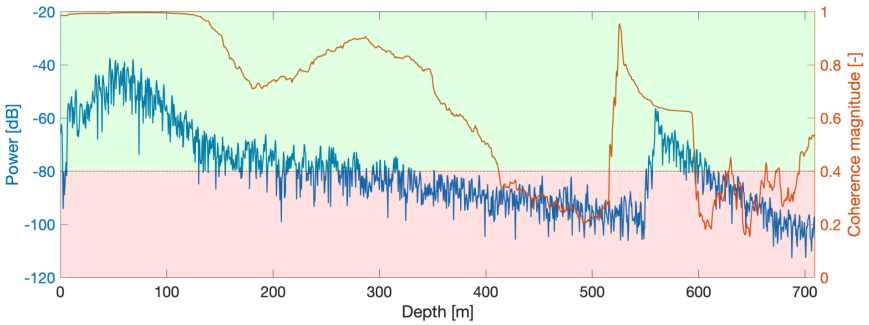

Figure 7.1: (a) Radar backscattered power (blue line) reveals the ice thickness. (b) The magnitude of complex polarimetric coherence between HH and VV signal (red line). The red zone is the area below 0.4 coherence magnitude.

7.2 Woodcock Plot (pRES and Ice Core)

Woodcock (1977) introduced the parameter $K = \frac{\ln(\lambda_3/\lambda_2)}{\ln(\lambda_2/\lambda_1)}$ as a logarithmic ratio between the Eigenvalues, dividing the ice fabric type into the cluster zone ($K > 1$) and the girdle zone ($K < 1$). The extreme cases are the uniaxial girdle (K close to 0) and the uniaxial cluster (K close to infinity), with $K = 1$ representing the transition zone. Additionally, Woodcock introduced the parameter $C = \ln(\lambda_3/\lambda_1)$ as a measure of the preferred orientation strength. Higher C values indicate a greater concentration of the c-axis and a lower noise level. By using Woodcock's method, the ice fabric type obtained from estimated and measured Eigenvalues can be compared.

Here we regenerated the figure 1 from Woodcock (1977) add added some extra information to it. Hand-drawn Schmidt diagrams illustrate the shape of the ice fabric type in each zone, where the top left and bottom right show the uniaxial cluster and the uniaxial girdle, respectively. The isotropic ice fabric is situated at the origin of the figure. Not that the thin sections in Schmidt diagrams from the ice core analysis in Fig 3.4c are vertical while the Schmidt diagrams shown in Fig 7.2 are oblique.The estimated and measured ice fabric types are depicted as green squares and black circles, respectively, within the 50 to 260 m range. Both the estimated and measured ice fabric types suggest that the fabric is in the weak cluster zone, although the estimated fabric is slightly weaker compared to the measured fabric.

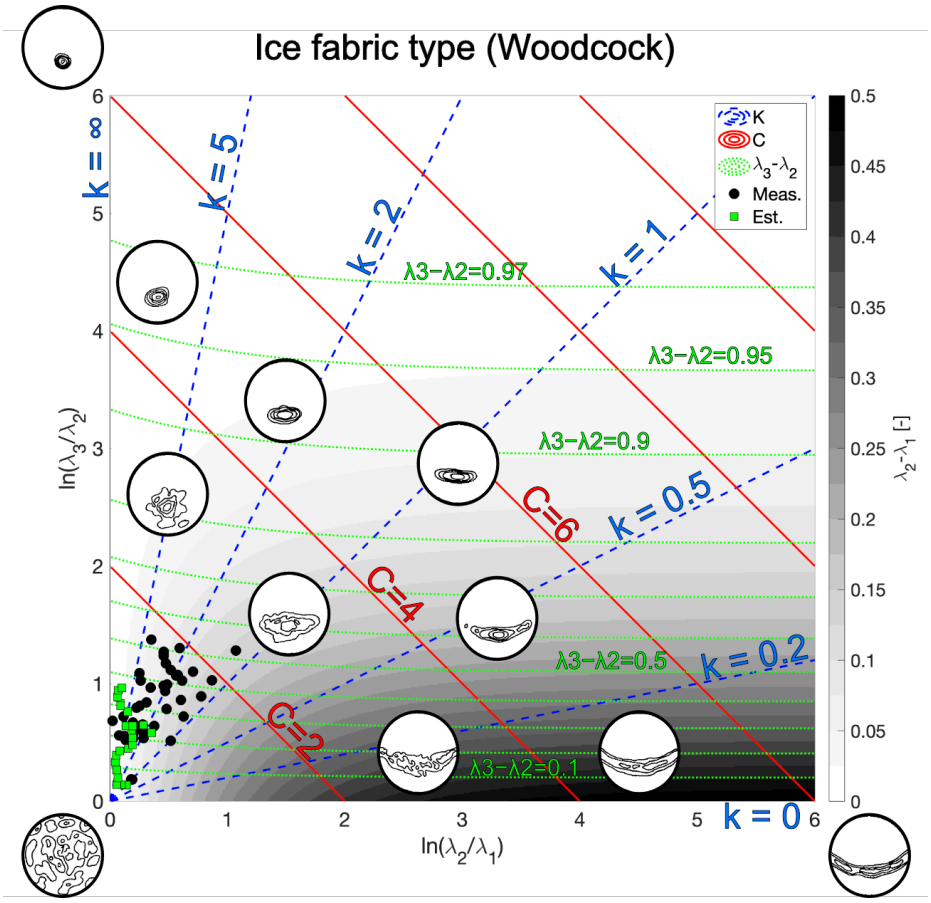

Figure 7.2: Regenerated Woodcock (1977), categorising the ice fabric type according to Woodcock's parameters. The background colour shows the change of $\Delta\lambda_H$, green dashed contours show the $\Delta\lambda_V$, blue dashed contours represent the K values, and rde contours are the C values. The Schmidt diagrams are copied directly from Woodcock (1977). The green squares and black circles are estimated from radar data and measured from the ice core, respectively, between 50 to 260 m depth.

7.3 2D Interpolated Fabric Spatial Change

A 2D interpolated spatial distribution of fabric properties inferred from pRES data is provided in figure 7.3. The values depicted in figure. 7.3a and 7.3b represent $\Delta\lambda_H$ and λ_3, respectively, directly estimated from the pRES data. On the other hand, figure 7.3c and 7.3d illustrate the deviation between the estimated ice fabric orientation $\vec{v}_2$ and the surface flow direction from SIA and between $\vec{v}_2$ and the maximum strain direction from SIA, respectively.

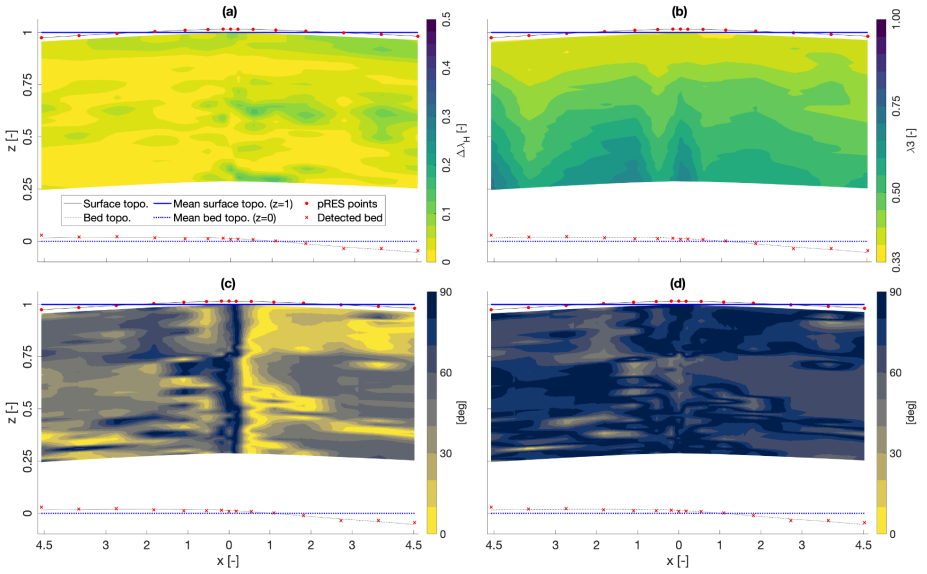

Figure 7.3: Showing the two dimensional interpolation of (a) horizontal ice fabric anisotropy. (b) Magnitude of the strongest eigenvalue ($lambda_3$). (c) deviation of $\vec{v}_2$ from surface flow direction. (d) deviation of $\vec{v}_2$ from maximum strain rate direction. Not that both X and Y axes are normalised by the mean ice thickness (H $\backsimeq$ 550 m).

7.4 SIA Results

The magnitude and orientation of surface velocity along with the magnitude and orientation of the maximum horizontal strain eastimated from SIA as explained in section 3.3.5 are shown all over HIR in Fig. 7.4

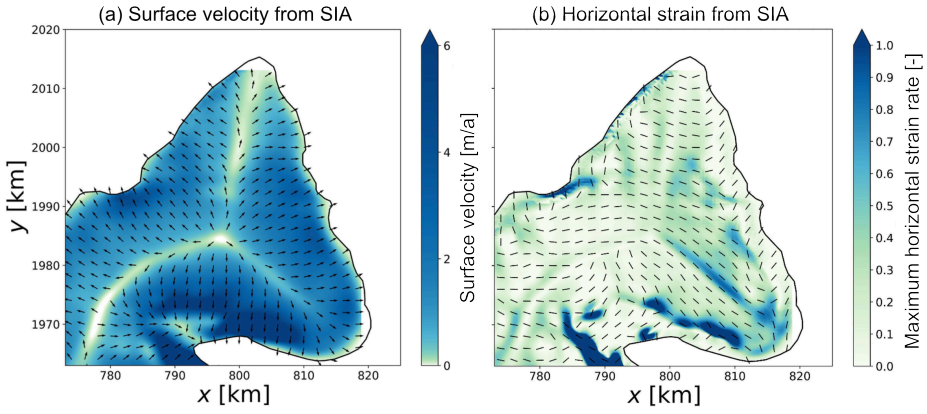

Figure 7.4: Estimated from SIA, (a) magnitude and direction of surface velocity. (b) magnitude and direction of maximum horizontal strain rate.

7.5 Code and Data availability

- Source Code is available on GitHub:
  RezaErshadi/HammarryggenIceRiseSourceCode_FabricInversion_Strainrates_SIA
  (Ershadi et al., 2023).
- prES and ice core data are available on Zenodo:
  https://zenodo.org/record/8095508
  (Pattyn et al., 2023).
- UWB data: Franke et al. (2020); Koch et al. (2023b).

7.6 Competing Interests

At least one of the (co-)authors is a an associate chief editor in JOG.

7.7 Acknowledgements

We would like to mention:

- M. Reza Ershadi, Reinhard Drews and Inka Koch were supported by Deutsche Forschungsgemeinschaft (DFG) Emmy Noether grant (grant no. DR 822/3-1).
- C. Henry was supported by DFG in the framework of the priority programme 1158 "Antarctic Research with comparative investigations in Arctic ice areas" by a grant SCHA 2139/1-1.
- F. Oraschewsik was supported by a scholarship from the Studienstiftung des Deutschen Volkes.
- Sarah Wauthy benefited from a Research Fellow grant of the F.R.S.-F.N.R.S.
- The ice core project was supported by The Belgian Research Action through Interdisciplinary Networks (BRAIN-be) from the Belgian Science Policy Office (BELSPO) in the framework of the project “East Antarctic surface mass balance in the Anthropocene: observations and multi-scale modelling (Mass2Ant) with contract no. BR/165/A2/Mass2Ant.
- We gratefully acknowledge the data acquisition of the UWB radar data by Daniela Jansen and Steven Franke and the contributions of Steven Franke to original data processing and the Ken Borek crew and PES staff for logistic support.

7.8 Financial Support

This research has been supported by

- Deutsche Forschungsgemeinschaft (DFG) Emmy Noether grant (grant no. DR 822/3-1).

- Deutsche Forschungsgemeinschaft (DFG) in the framework of the priority programme 1158 "Antarctic Research with comparative investigations in Arctic ice areas" by a grant SCHA 2139/1-1.
- Studienstiftung des Deutschen Volkes.
- Research Fellow grant of the F.R.S.-F.N.R.S.
- Belgian Research Action through Interdisciplinary Networks (BRAIN-be) from the Belgian Science Policy Office (BELSPO) in the framework of the project “East Antarctic surface mass balance in the Anthropocene: observations and multi-scale modelling (Mass2Ant) with contract no. BR/165/A2/Mass2Ant.

Chapter 8

Supporting Information for Chapter 4

8.1 ROS2 Structure

ROS2 (Macenski et al., 2022) facilitates simultaneous communication among all the components within the SLEDGE. Fig. 8.1 provides an overview of the nodes, topics, and services, illustrating how they interconnect. The system comprises a total of 11 nodes responsible for various tasks, communicating with each other through topics and services.

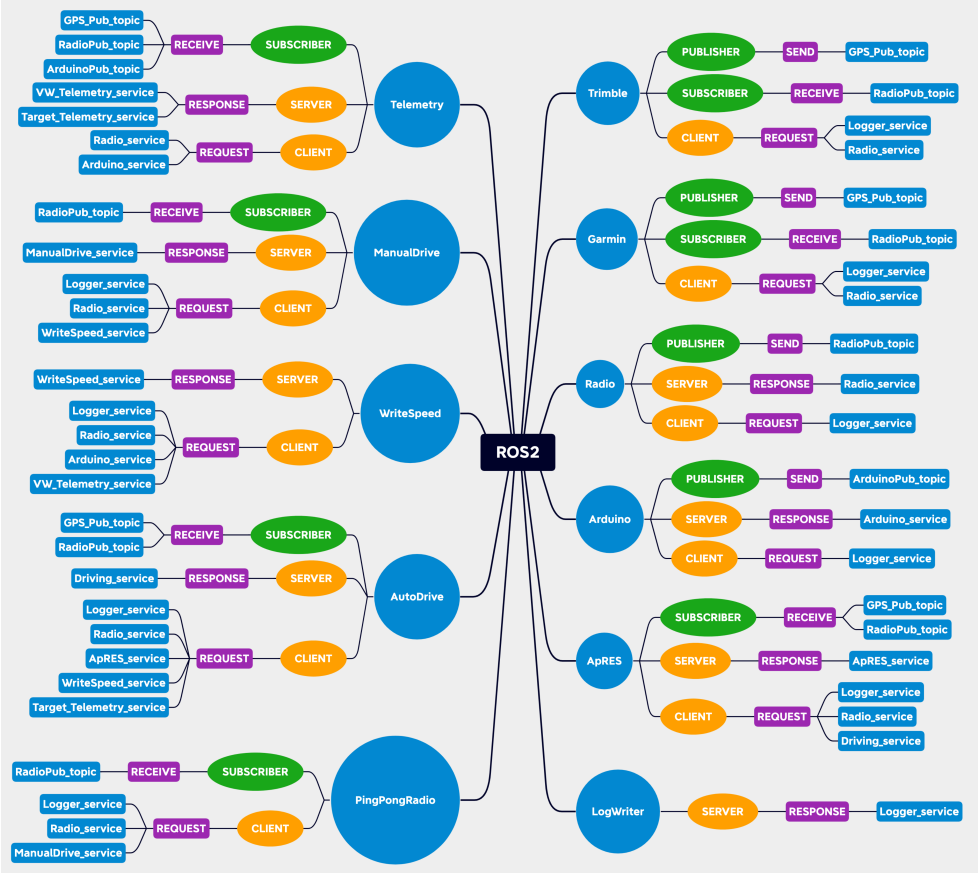

Figure 8.1: Flow chart of the ROS2 nodes, topics, and server structure for SLEDGE. blue circles are the nodes, green and orange ovals are the type of communication that nodes are capable of, purple rectangles are the direction of the actions, and blue rectangles are the names of the topics and servers.

These nodes can be divided into two categories. The first category consists of nodes directly controlling the components connected to the system. This includes two GNSS nodes (Trimble and Garmin) that read and publish GNSS information for other nodes, a Radio node for sending and receiving radio data, an Arduino node responsible for writing the final linear and angular velocities to the engines, and an ApRES node that triggers the pRES device. The second category comprises six nodes that perform various tasks and calculations. The LogWriter node records log files documenting all actions within the system, while the Telemetry node publishes telemetry information for the operator. The PingPongRadio node continuously checks the radio

connection and stops the rover if no connection is detected. The ManualDrive node is active when the operator is manually controlling the rover, while the AutoDrive node controls autonomous driving. Finally, the WriteSpeed node handles the finalization of linear and angular velocities.

8.2 Control Station User Interface

As mentioned in section 4.2.2, the control station interface, which provides the operator with full remote control over the rover, has been completely rewritten. The new version uses the MATLAB GUI toolbox, offering convenient control options according to our needs. This interface allows for seamless switching between GNSS systems, triggering the pRES, and manual or autonomous driving of the rover. Moreover, it provides the capability to design autonomous radar surveys using three different methods: single-point, profile, and area. When designing an autonomous radar survey, the survey designer prompts the operator for relevant survey information and creates a survey path along with a simulated rover path. The interface also presents visual information to the operator, including telemetry data such as battery level, current linear and angular velocities, and a map displaying the rover's current location and target points.

8.3 Backscattered Power

Here we show the backscattered power from all the antenna combinations collected by SLEDGE. In Fig. 8.2 we can see the reflection between the ice and both bedrock and ocean are stronger in VH signal. The expectation is to have the same quality of reflection in the HV signal as well however HV shows slightly weaker reflection, but it is still stronger than HH and VV.

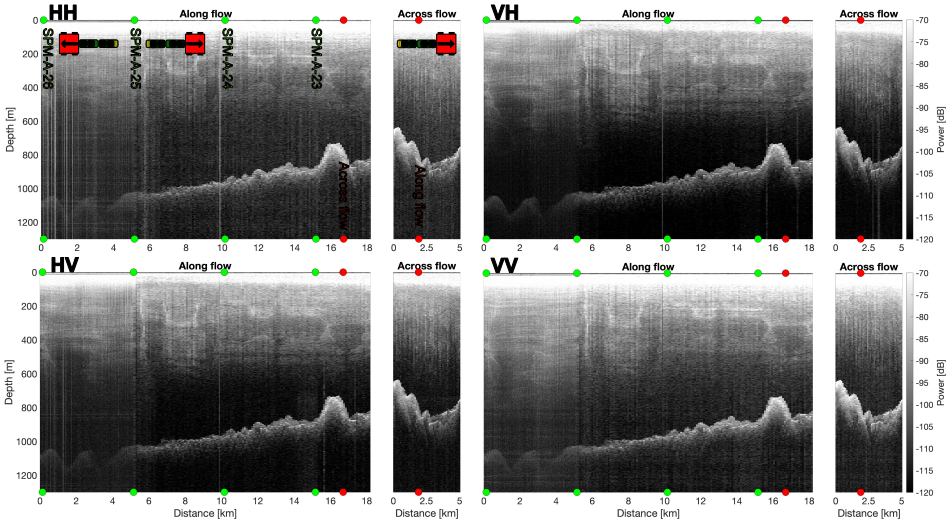

Figure 8.2: Backscattered power from all the antenna combinations.

8.4 Polarimetric Coherence

Here, in Fig. 8.3a we present an example of a standard figure for quad-polarimetric data (Ershadi et al., 2022b) for a single point and quad-polarimetric metrics for the along-flow profile, fully synthesized for a 180° orientation, where alpha = 0 and 180 degrees align with the driving direction. This includes co-polarized (HH) and cross-polarized (VH) power anomalies, along with the coherence phase between HH and VV.

In Fig. 8.3a1, the power (a1) depicts the backscattered power of the signal, indicating ice thickness (885 m). The absence of 90° symmetry in the co-polarized power anomaly (a2) detects anisotropic reflection. In contrast, the cross-polarized power anomaly (a3) exhibits a 90° periodicity, with minima at 0 and 90 degrees, representing the orientation of the strongest and weakest anisotropy directions on a horizontal plane. The coherence phase between HH and VV (a4), varying sign every 90 degrees while maintaining the pattern, clarifies the 90° ambiguity for the weakest and strongest fabric orientation directions, with the scaled factor of its depth gradient serving as a proxy for the magnitude of ice-fabric anisotropy. More details about the parameters and patterns in this type of figures are explained in (Ershadi et al., 2022b).

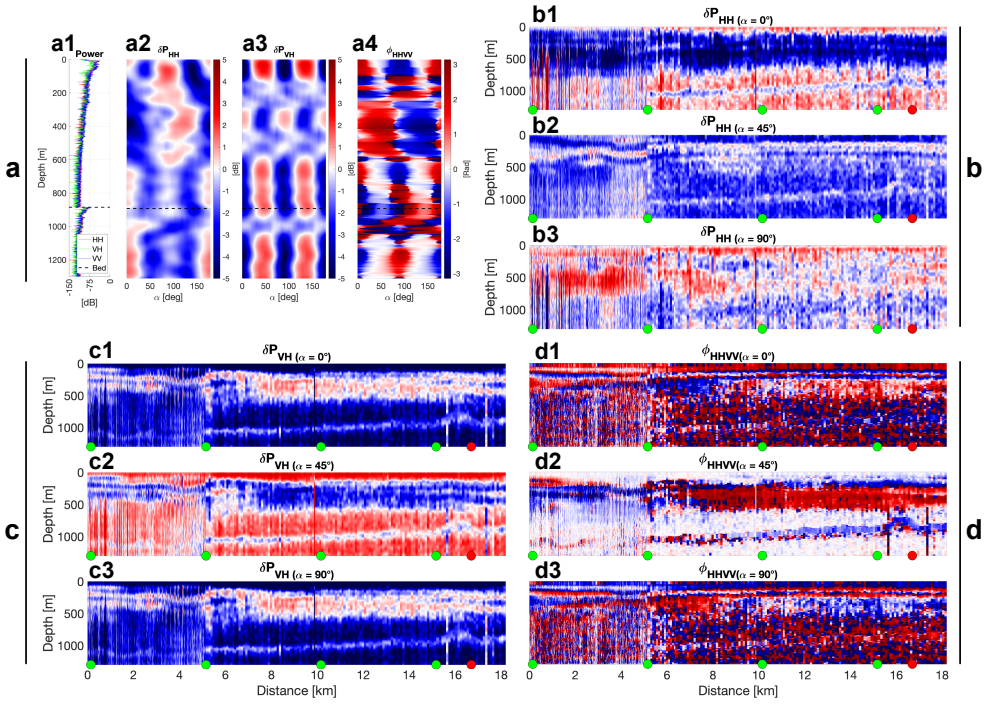

Figure 8.3: a: standard quad-polarimetric plot for a single measured point (at 12 km distance along flow profile) where a1 shows the backscattered power, a2 shows the HH power anomaly, a3 shows the VH power anomaly and a4 shows the coherence phase between HH and VV. b: HH power anomaly for all the measured points along the flow profile at 0° (b1), 45° (b2) and 90° (b3) orientation. This section shares the color map with a2. c: Same as (b) but for VH power anomaly. This section shares the color map with a3. d: same as (a) and (b) but for the coherence phase between HH and VV. This section shares the color map with a4.

Figure 8.3b-d show the quad-polarimetric metrics for the along-flow profile, fully synthesized for a 180° orientation, where alpha = 0 align with the driving direction. To illustrate these metrics in a profile, three synthesized orientations (0, 45, and 90 degrees relative to the driving direction) were chosen and are shown. The HH (co-polarized) power anomaly (Fig. 8.3-b), indicating anisotropic reflection across the area. The VH (cross-polarized) power anomaly (Fig. 8.3-c) with the blue color dominance at 0° and, as expected, at 90°. Notably, the red band at 0 and 90° turns blue at 45°, suggesting a fabric rotation of approximately 45 degrees in that part of the ice column, consistently observed in the floating ice. While a detailed analysis of the degree of anisotropy requires further examination of the coherence phase (Fig. 8.3-d), certain patterns in the 45° orientation resemble those observed in the coherence phase and this band's dominance in the floating ice with a different polarity indicates a fabric change after the ice passes the grounding line.

8.5 SLEDGE - List of Components

Here we list all the major components of SLEDGE including their names, produced, and links to their website.

- The rover (FrostyBoy)
  - Polar Research Equipment
  - https://www.polarresearchequipment.com/
- Motor controller
  - RoboteQ FBL brushless dc motor controller
  - https://www.roboteq.com/products/products-brushless-dc-motor-controllers/fbl-family
- Motors
  - ElectroCraft Rapid Power Brushless DC engine
  - https://www.electrocraft.com/products/bldc/
- Transmission
  - NEUGART economy gearbox
  - https://www.neugart.com/en/gearboxes#economy-gearboxes
- Radio modem and antenna
  - Digi XBee SX RF Modems
  - https://www.digi.com/products/embedded-systems/digi-xbee/digi-xbee-gateways/digi-xbee-sx-rf-modems
- Mini industrial computer
  - ADVANTECH ARK1551
  - https://www.advantech.com/en-eu/products/92d96fda-cdd3-409d-aae5-2e516c0f1b01/ark-1551/mod_47d30ee7-28b6-41bc-83a1-a7ca416e68cd

- Arduino board
  - Arduino Due
  - https://store.arduino.cc/products/arduino-due
- Garmin navigation system
  - Garmin 19x HVS GNSS package
  - https://www.garmin.com/de-DE/p/100686
- Trimble navigation system
  - Trimble Two Zephyr 3 antennas
  - https://geospatial.trimble.com/products-and-solutions/trimble-zephyr-3
  - Trimble R9s-type receivers
  - https://stg-geospatial.trimble.com/sites/geospatial.trimble.com/files/2021-01/Datasheet%20-%20Trimble%20R9s%20GNSS%20Receiver%20-%20German%20-%20Screen.pdf
- Sleds
  - AIRFRAMEALASKA Cross Fox Sleds
  - https://www.airframesalaska.com/cross-fox-sleds-s/2253.htm
- pRES radar
  - Brennan et al. (2014); Nicholls et al. (2015)

8.6 Code and Data Availability

- The rover (ROS2) and interface (MATLAB GIU) source code for SLEDGE: https://zenodo.org/records/10064669
- pRES HTTP REST API: https://zenodo.org/records/10047461
- pRES quad-polarimetric for field manual and code: https://zenodo.org/records/10064673
- Data in the process of submission to the PANGAEA database.

8.7 Competing Interests

- JE and APL are commercial robotic suppliers of the rover (FROSTYBOY) used in this study.

8.8 Acknowledgment

- We would like to mention M. Reza Ershadi, Inka Koch, and Reinhard Drews were supported by Deutsche Forschungsgemeinschaft (DFG) Emmy Noether grant (grant no. DR 822/3-1).
- We would like to mention Jonathan Hawkins was funded by Royal Society Enhancement Award number RGF\EA\180173 awarded to Dr Lai Bun Lok.
- We would like to thank the GrouZe team and the logistic support from Neumayer III.

8.9 Financial Support

This research has been supported by:

- Deutsche Forschungsgemeinschaft (DFG) Emmy Noether grant (grant no. DR 822/3-1).

Bibliography

Ackley, S. F. and Keliher, T. E.: Ice Sheet Internal Radio-Echo Reflections and Associated Physical Property Changes with Depth, Journal of Geophysical Research, 84, 5675, doi: 10.1029/JB084iB10p05675, 1979.

Alley, R. B.: Flow-Law Hypotheses for Ice-Sheet Modeling, Journal of Glaciology, 38, 245–256, doi: 10.3189/S0022143000003658, 1992.

Andreasen, J. R., Hogg, A. E., and Selley, H. L.: Change in Antarctic Ice Shelf Area from 2009 to 2019, The Cryosphere, 17, 2059–2072, doi: 10.5194/tc-17-2059-2023, 2023.

Arcone, S. A.: High Resolution of Glacial Ice Stratigraphy: A Ground-penetrating Radar Study of Pegasus Runway, McMurdo Station, Antarctica, GEOPHYSICS, 61, 1653–1663, doi: 10.1190/1.1444084, 1996.

Arcone, S. A., Lever, J. H., Ray, L. E., Walker, B. S., Hamilton, G., and Kaluzienski, L.: Ground-Penetrating Radar Profiles of the McMurdo Shear Zone, Antarctica, Acquired with an Unmanned Rover: Interpretation of Crevasses, Fractures, and Folds within Firn and Marine Ice, Geophysics, doi: 10.1190/geo2015-0132.1, 2015.

Assmann, K. M., Darelius, E., Wåhlin, A. K., Kim, T. W., and Lee, S. H.: Warm Circumpolar Deep Water at the Western Getz Ice Shelf Front, Antarctica, Geophysical Research Letters, 46, 870–878, doi: 10.1029/2018GL081354, 2019.

Azuma, N.: A Flow Law for Anisotropic Ice and Its Application to Ice Sheets, Earth and Planetary Science Letters, 128, 601–614, doi: 10.1016/0012-821X(94)90173-2, 1994.

Azuma, N. and Goto-Azuma, K.: An Anisotropic Flow Law for Ice-Sheet Ice and Its Implications, Annals of Glaciology, 23, 202–208, doi: 10/gpbxx7, 1996.

Azuma, N., Wang, Y., Mori, K., Narita, H., Hondoh, T., Shoji, H., and Watanabe, O.: Textures and Fabrics in the Dome F (Antarctica) Ice Core, Annals of Glaciology, 29, 163–168, doi: 10/b7w24f, 1999.

Bentley, C. R.: Seismic-Wave Velocities in Anisotropic Ice: A Comparison of Measured and Calculated Values in and around the Deep Drill Hole at Byrd Station, Antarctica, Journal of Geophysical Research (1896-1977), 77, 4406–4420, doi: 10.1029/JB077i023p04406, 1972.

Bentley, M. J., Ó Cofaigh, C., Anderson, J. B., Conway, H., Davies, B., Graham, A. G. C., Hillenbrand, C.-D., Hodgson, D. A., Jamieson, S. S. R., Larter, R. D., Mackintosh, A., Smith, J. A., Verleyen, E., Ackert, R. P., Bart, P. J., Berg, S., Brunstein, D., Canals, M., Colhoun, E. A., Crosta,

X., Dickens, W. A., Domack, E., Dowdeswell, J. A., Dunbar, R., Ehrmann, W., Evans, J., Favier, V., Fink, D., Fogwill, C. J., Glasser, N. F., Gohl, K., Golledge, N. R., Goodwin, I., Gore, D. B., Greenwood, S. L., Hall, B. L., Hall, K., Hedding, D. W., Hein, A. S., Hocking, E. P., Jakobsson, M., Johnson, J. S., Jomelli, V., Jones, R. S., Klages, J. P., Kristoffersen, Y., Kuhn, G., Leventer, A., Licht, K., Lilly, K., Lindow, J., Livingstone, S. J., Massé, G., McGlone, M. S., McKay, R. M., Melles, M., Miura, H., Mulvaney, R., Nel, W., Nitsche, F. O., O'Brien, P. E., Post, A. L., Roberts, S. J., Saunders, K. M., Selkirk, P. M., Simms, A. R., Spiegel, C., Stolldorf, T. D., Sugden, D. E., van der Putten, N., van Ommen, T., Verfaillie, D., Vyverman, W., Wagner, B., White, D. A., Witus, A. E., and Zwartz, D.: A Community-Based Geological Reconstruction of Antarctic Ice Sheet Deglaciation since the Last Glacial Maximum, Quaternary Science Reviews, 100, 1–9, doi: 10.1016/j.quascirev.2014.06.025, 2014.

Bergstrom, A., Gooseff, M. N., Myers, M., Doran, P. T., and Cross, J. M.: The Seasonal Evolution of Albedo across Glaciers and the Surrounding Landscape of Taylor Valley, Antarctica, The Cryosphere, 14, 769–788, doi: 10.5194/tc-14-769-2020, 2020.

Bintanja, R., van Oldenborgh, G. J., and Katsman, C. A.: The Effect of Increased Fresh Water from Antarctic Ice Shelves on Future Trends in Antarctic Sea Ice, Annals of Glaciology, 56, 120–126, doi: 10.3189/2015AoG69A001, 2015.

Bohleber, P., Wagner, N., and Eisen, O.: Permittivity of Ice at Radio Frequencies: Part II. Artificial and Natural Polycrystalline Ice, Cold Regions Science and Technology, 83–84, 13–19, doi: 10/9rf, 2012.

Bons, P. D., Kleiner, T., Llorens, M.-G., Prior, D. J., Sachau, T., Weikusat, I., and Jansen, D.: Greenland Ice Sheet: Higher Nonlinearity of Ice Flow Significantly Reduces Estimated Basal Motion, Geophysical Research Letters, 45, 6542–6548, doi: 10.1029/2018GL078356, 2018.

Brennan, P. V., Lok, L. B., Nicholls, K., and Corr, H.: Phase-sensitive FMCW Radar System for High-precision Antarctic Ice Shelf Profile Monitoring, IET Radar, Sonar & Navigation, 8, 776–786, doi: 10/ghhvxb, 2014.

Brisbourne, A. M., Martín, C., Smith, A. M., Baird, A. F., Kendall, J. M., and Kingslake, J.: Constraining Recent Ice Flow History at Korff Ice Rise, West Antarctica, Using Radar and Seismic Measurements of Ice Fabric, Journal of Geophysical Research: Earth Surface, 124, 175–194, doi: 10/gm5w7t, 2019.

Bronselaer, B., Winton, M., Griffies, S. M., Hurlin, W. J., Rodgers, K. B., Sergienko, O. V., Stouffer, R. J., and Russell, J. L.: Change in Future Climate Due to Antarctic Meltwater, Nature, 564, 53–58, doi: 10.1038/s41586-018-0712-z, 2018.

Brook, E. J. and Buizert, C.: Antarctic and Global Climate History Viewed from Ice Cores, Nature, 558, 200–208, doi: 10.1038/s41586-018-0172-5, 2018.

Budd, W. F. and Jacka, T. H.: A Review of Ice Rheology for Ice Sheet Modelling, Cold Regions Science and Technology, 16, 107–144, doi: 10.1016/0165-232X(89)90014-1, 1989.

Case, E. and Kingslake, J.: Phase-Sensitive Radar as a Tool for Measuring Firn Compaction, Journal of Glaciology, pp. 1–14, doi: 10/gm6vd3, 2021.

Cavitte, M. G. P., Blankenship, D. D., Young, D. A., Schroeder, D. M., Parrenin, F., Lemeur, E., Macgregor, J. A., and Siegert, M. J.: Deep Radiostratigraphy of the East Antarctic Plateau: Connecting the Dome C and Vostok Ice Core Sites, Journal of Glaciology, 62, 323–334, doi: 10/f8s9p9, 2016.

Cavitte, M. G. P., Goosse, H., Wauthy, S., Kausch, T., Tison, J.-L., Liefferinge, B. V., Pattyn, F., Lenaerts, J. T. M., and Claeys, P.: From Ice Core to Ground-Penetrating Radar: Representativeness of SMB at Three Ice Rises along the Princess Ragnhild Coast, East Antarctica, Journal of Glaciology, pp. 1–13, doi: 10.1017/jog.2022.39, 2022.

Chartrand, R.: Numerical Differentiation of Noisy, Nonsmooth Data, ISRN Applied Mathematics, 2011, 1–11, doi: 10/fjh7d5, 2011.

Christmann, J., Zeising, O., and Humbert, A.: Polarimetric Phase-Sensitive Radio Echo Sounder Measurements at EDML, 2017, doi: 10.1594/PANGAEA.913719, 2020.

Church, G., Grab, M., Schmelzbach, C., Bauder, A., and Maurer, H.: Monitoring the Seasonal Changes of an Englacial Conduit Network Using Repeated Ground-Penetrating Radar Measurements, The Cryosphere, 14, 3269–3286, doi: 10.5194/tc-14-3269-2020, 2020.

Church, G., Bauder, A., Grab, M., and Maurer, H.: Ground-Penetrating Radar Imaging Reveals Glacier's Drainage Network in 3D, The Cryosphere, 15, 3975–3988, doi: 10.5194/tc-15-3975-2021, 2021.

Chuter, S. J. and Bamber, J. L.: Antarctic Ice Shelf Thickness from CryoSat-2 Radar Altimetry, Geophysical Research Letters, 42, 10,721–10,729, doi: 10.1002/2015GL066515, 2015.

Conway, H. and Wilbour, C.: Evolution of Snow Slope Stability during storms, Version 1.5d from 1997/04/28.1, Cold Regions Science and Technology, 30, 67–77, doi: 10.1016/S0165-232X(99)00009-9, 1999.

Cook, S. J., Swift, D. A., Kirkbride, M. P., Knight, P. G., and Waller, R. I.: The Empirical Basis for Modelling Glacial Erosion Rates, Nature Communications, 11, 759, doi: 10/gm5w7v, 2020.

Corr, H., Ritz, C., and Martin, C.: Polarimetric ApRES Data on a Profile across Dome C, East Antarctica, 2013-2014, doi: 10.5285/634EE206-258F-4B47-9237-EFFF4EF9EEDD, 2021.

Corr, H. F. J., Jenkins, A., Nicholls, K. W., and Doake, C. S. M.: Precise Measurement of Changes in Ice-Shelf Thickness by Phase-Sensitive Radar to Determine Basal Melt Rates, Geophysical Research Letters, 29, 73–1–74–4, doi: 10/bmw9nc, 2002.

Dall, J.: Ice Sheet Anisotropy Measured with Polarimetric Ice Sounding Radar, in: 2010 IEEE International Geoscience and Remote Sensing Symposium, pp. 2507–2510, IEEE, Honolulu, HI, USA, doi: 10/dvwxpd, 2010.

Davies, B. J., Hambrey, M. J., Smellie, J. L., Carrivick, J. L., and Glasser, N. F.: Antarctic Peninsula Ice Sheet Evolution during the Cenozoic Era, Quaternary Science Reviews, 31, 30–66, doi: 10.1016/j.quascirev.2011.10.012, 2012.

Diez, A. and Eisen, O.: Seismic Wave Propagation in Anisotropic Ice – Part 1: Elasticity Tensor and Derived Quantities from Ice-Core Properties, The Cryosphere, 9, 367–384, doi: 10/f648p5, 2015.

Diez, A., Eisen, O., Weikusat, I., Eichler, J., Hofstede, C., Bohleber, P., Bohlen, T., and Polom, U.: Influence of Ice Crystal Anisotropy on Seismic Velocity Analysis, Annals of Glaciology, 55, 97–106, doi: 10.3189/2014AoG67A002, 2014.

Diez, A., Eisen, O., Hofstede, C., Lambrecht, A., Mayer, C., Miller, H., Steinhage, D., Binder, T., and Weikusat, I.: Seismic Wave Propagation in Anisotropic Ice – Part 2: Effects of Crystal Anisotropy in Geophysical Data, The Cryosphere, 9, 385–398, doi: 10/f647nh, 2015.

Diprinzio, C. L., Wilen, L. A., Alley, R. B., Fitzpatrick, J. J., Spencer, M. K., and Gow, A. J.: Fabric and Texture at Siple Dome, Antarctica, Journal of Glaciology, 51, 281–290, doi: 10.3189/172756505781829359, 2005.

Doake, C. S. M.: Polarization of Radio Waves in Ice Sheets, Geophysical Journal International, 64, 539–558, doi: 10/c6jgb4, 1981.

Doake, C. S. M., Corr, H. F. J., and Jenkins, A.: Polarization of Radio Waves Transmitted through Antarctic Ice Shelves, Annals of Glaciology, 34, 165–170, doi: 10/d76vnd, 2002.

Doake, C. S. M., Corr, H. F. J., Jenkins, A., Nicholls, K. W., and Stewart, C.: Interpretation of Polarimetric Ice Penetrating Radar Data over Antarctic Ice Shelves., Tech. rep., 2003.

Dong, H., Sun, W., Shen, Y., Baláz, M., Balázová, L., Ding, L., Löffler, M., Hamilton, B., Klöting, N., Blüher, M., Neubauer, H., Klein, H., and Wolfrum, C.: Identification of a Regulatory Pathway Inhibiting Adipogenesis via RSPO2, Nature Metabolism, 4, 90–105, doi: 10.1038/s42255-021-00509-1, 2022.

Drews, R., Eisen, O., Steinhage, D., Weikusat, I., Kipfstuhl, S., and Wilhelms, F.: Potential Mechanisms for Anisotropy in Ice-Penetrating Radar Data, Journal of Glaciology, 58, 613–624, doi: 10/ghvgx8, 2012.

Drews, R., Martín, C., Steinhage, D., and Eisen, O.: Characterizing the Glaciological Conditions at Halvfarryggen Ice Dome, Dronning Maud Land, Antarctica, Journal of Glaciology, 59, 9–20, doi: 10/ghvgvz, 2013.

Drews, R., Brown, J., Matsuoka, K., Witrant, E., Philippe, M., Hubbard, B., and Pattyn, F.: Anomalously-Dense Firn in an Ice-Shelf Channel Revealed by Wide-Angle Radar, Preprint, Antarctic, doi: 10.5194/tcd-9-5647-2015, 2015a.

Drews, R., Matsuoka, K., Martín, C., Callens, D., Bergeot, N., and Pattyn, F.: Evolution of Derwael Ice Rise in Dronning Maud Land, Antarctica, over the Last Millennia: DREWS ET AL., Journal of Geophysical Research: Earth Surface, 120, 564–579, doi: 10/gm5w7w, 2015b.

Drews, R., Pattyn, F., Hewitt, I. J., Ng, F. S. L., Berger, S., Matsuoka, K., Helm, V., Bergeot, N., Favier, L., and Neckel, N.: Actively Evolving Subglacial Conduits and Eskers Initiate Ice Shelf Channels at an Antarctic Grounding Line, Nature Communications, 8, 15 228, doi: 10/f96p87, 2017.

Durand, G., Gillet-Chaulet, F., Svensson, A., Gagliardini, O., Kipfstuhl, S., Meyssonnier, J., Parrenin, F., Duval, P., and Dahl-Jensen, D.: Change in Ice Rheology during Climate Variations – Implications for Ice Flow Modelling and Dating of the EPICA Dome C Core, Climate of the Past, 3, 155–167, doi: 10/fskxzw, 2007.

Durand, G., Svensson, A., Persson, A., Gagliardini, O., Gillet-Chaulet, F., Sjolte, J., Montagnat, M., and Dahl-Jensen, D.: Evolution of the Texture along the EPICA Dome C Ice Core, Low Temperature Science, 68, 91–105, 2009.

Dutrieux, P., Vaughan, D. G., Corr, H. F. J., Jenkins, A., Holland, P. R., Joughin, I., and Fleming, A. H.: Pine Island Glacier Ice Shelf Melt Distributed at Kilometre Scales, The Cryosphere, 7, 1543–1555, doi: 10.5194/tc-7-1543-2013, 2013.

Dutrieux, P., Stewart, C., Jenkins, A., Nicholls, K. W., Corr, H. F. J., Rignot, E., and Steffen, K.: Basal Terraces on Melting Ice Shelves, Geophysical Research Letters, 41, 5506–5513, doi: 10.1002/2014GL060618, 2014.

Duval, P., Ashby, M. F., and Anderman, I.: Rate-Controlling Processes in the Creep of Polycrystalline Ice, The Journal of Physical Chemistry, 87, 4066–4074, doi: 10/ccnxz3, 1983.

Edwards, T. L., Nowicki, S., Marzeion, B., Hock, R., Goelzer, H., Seroussi, H., Jourdain, N. C., Slater, D. A., Turner, F. E., Smith, C. J., McKenna, C. M., Simon, E., Abe-Ouchi, A., Gregory, J. M., Larour, E., Lipscomb, W. H., Payne, A. J., Shepherd, A., Agosta, C., Alexander, P., Albrecht, T., Anderson, B., Asay-Davis, X., Aschwanden, A., Barthel, A., Bliss, A., Calov, R., Chambers, C., Champollion, N., Choi, Y., Cullather, R., Cuzzone, J., Dumas, C., Felikson, D., Fettweis, X., Fujita, K., Galton-Fenzi, B. K., Gladstone, R., Golledge, N. R., Greve, R., Hattermann, T., Hoffman, M. J., Humbert, A., Huss, M., Huybrechts, P., Immerzeel, W., Kleiner, T., Kraaijenbrink, P., Le clec'h, S., Lee, V., Leguy, G. R., Little, C. M., Lowry, D. P., Malles, J.-H., Martin, D. F., Maussion, F., Morlighem, M., O'Neill, J. F., Nias, I., Pattyn, F., Pelle, T., Price, S. F., Quiquet, A., Radić, V., Reese, R., Rounce, D. R., Rückamp, M., Sakai, A., Shafer, C., Schlegel, N.-J., Shannon, S., Smith, R. S., Straneo, F., Sun, S., Tarasov, L., Trusel, L. D., Van Breedam, J., van de Wal, R., van den Broeke, M., Winkelmann, R., Zekollari, H., Zhao, C., Zhang, T., and Zwinger, T.: Projected Land Ice Contributions to Twenty-First-Century Sea Level Rise, Nature, 593, 74–82, doi: 10.1038/s41586-021-03302-y, 2021.

Eisen, O., Wilhelms, F., Nixdorf, U., and Miller, H.: Identifying Isochrones in GPR Profiles from DEP-based Forward Modeling, Annals of Glaciology, 37, 344–350, doi: 10/d4f244, 2003.

Eisen, O., Hamann, I., Kipfstuhl, S., Steinhage, D., and Wilhelms, F.: Direct Evidence for Continuous Radar Reflector Originating from Changes in Crystal-Orientation Fabric, The Cryosphere, 1, 1–10, doi: 10/fg9vf3, 2007.

Eisen, O., Nixdorf, U., Keck, L., and Wagenbach, D.: Alpine Ice Cores and Ground Penetrating Radar: Combined Investigations for Glaciological and Climatic Interpretations of a Cold Alpine Ice Body, Tellus B: Chemical and Physical Meteorology, 55, 1007–1017, doi: 10.3402/tellusb.v55i5.16394, 2011.

Ershadi, M. R., Drews, R., Koch, I., Oraschewski, F., Prinz, R., Martin, C., and Eisen, O.: Mapping the Bed in Challenging Radar Environments on Alpine Glaciers and Ice Sheets Using Radar Polarimetry, Tech. Rep. EGU22-9915, Copernicus Meetings, doi: 10.5194/egusphere-egu22-9915, 2022a.

Ershadi, M. R., Drews, R., Martín, C., Eisen, O., Ritz, C., Corr, H., Christmann, J., Zeising, O., Humbert, A., and Mulvaney, R.: Polarimetric Radar Reveals the Spatial Distribution of Ice Fabric at Domes and Divides in East Antarctica, The Cryosphere, 16, 1719–1739, doi: 10.5194/tc-16-1719-2022, 2022b.

Ershadi, M. R., Henry, A. C. J., and Oraschewski, F. M.: Source Code to Estimate Ice Fabric Anisotropy and Strain Rate at Hammarryggen Ice Rise - Antarctica (Supplementary Material), Zenodo, doi: 10.5281/zenodo.8364628, 2023.

Faria, S. H., Weikusat, I., and Azuma, N.: The Microstructure of Polar Ice. Part II: State of the Art, Journal of Structural Geology, 61, 21–49, doi: 10/gmqk4w, 2014a.

Faria, S. H., Weikusat, I., and Azuma, N.: The Microstructure of Polar Ice. Part I: Highlights from Ice Core Research, Journal of Structural Geology, 61, 2–20, doi: 10.1016/j.jsg.2013.09.010, 2014b.

Favier, L. and Pattyn, F.: Antarctic Ice Rise Formation, Evolution, and Stability, Geophysical Research Letters, 42, 4456–4463, doi: 10.1002/2015GL064195, 2015.

Favier, L., Gagliardini, O., Durand, G., and Zwinger, T.: A Three-Dimensional Full Stokes Model of the Grounding Line Dynamics: Effect of a Pinning Point beneath the Ice Shelf, The Cryosphere, 6, 101–112, doi: 10.5194/tc-6-101-2012, 2012.

Favier, L., Durand, G., Cornford, S. L., Gudmundsson, G. H., Gagliardini, O., Gillet-Chaulet, F., Zwinger, T., Payne, A. J., and Le Brocq, A. M.: Retreat of Pine Island Glacier Controlled by Marine Ice-Sheet Instability, Nature Climate Change, 4, 117–121, doi: 10.1038/nclimate2094, 2014.

Franke, S., Jansen, D., Drews, R., and Eisen, O.: Ice Thickness from the Coast of Dronning Maud Land (Antarctica), Recorded 2018/19 with the AWI UWB Radar System, doi: 10.1594/PANGAEA.911868, 2020.

Franke, S., Eisermann, H., Jokat, W., Eagles, G., Asseng, J., Miller, H., Steinhage, D., Helm, V., Eisen, O., and Jansen, D.: Preserved Landscapes underneath the Antarctic Ice Sheet Reveal the Geomorphological History of Jutulstraumen Basin, Earth Surface Processes and Landforms, 46, 2728–2745, doi: 10.1002/esp.5203, 2021.

Franke, S., Jansen, D., Binder, T., Paden, J. D., Dörr, N., Gerber, T. A., Miller, H., Dahl-Jensen, D., Helm, V., Steinhage, D., Weikusat, I., Wilhelms, F., and Eisen, O.: Airborne Ultra-Wideband Radar Sounding over the Shear Margins and along Flow Lines at the Onset Region of the Northeast Greenland Ice Stream, Earth System Science Data, 14, 763–779, doi: 10.5194/essd-14-763-2022, 2022.

Franke, S., Bons, P. D., Streng, K., Mundel, F., Binder, T., Weikusat, I., Bauer, C. C., Paden, J. D., Dörr, N., Helm, V., Steinhage, D., Eisen, O., and Jansen, D.: Three-Dimensional Topology Dataset of Folded Radar Stratigraphy in Northern Greenland, Scientific Data, 10, 525, doi: 10.1038/s41597-023-02339-0, 2023.

Frémand, A. C., Bodart, J. A., Jordan, T. A., Ferraccioli, F., Robinson, C., Corr, H. F. J., Peat, H. J., Bingham, R. G., and Vaughan, D. G.: British Antarctic Survey's Aerogeophysical Data: Releasing 25 Years of Airborne Gravity, Magnetic, and Radar Datasets over Antarctica, Earth System Science Data, 14, 3379–3410, doi: 10.5194/essd-14-3379-2022, 2022.

Fromm, T., Oberdieck, C., Heitland, T., and Köhler, P.: Expeditions to Antarctica: ANT-Land 2018/19 Neumayer Station III, Kohnen Station, Flight Operations and Field Campaigns, doi: 10.2312/BzPM_0733_2019, 2019.

Fujita, S. and Mae, S.: Relation between Ice Sheet Internal Radio-Echo Reflections and Ice Fabric at Mizuho Station, Antarctica, Annals of Glaciology, 17, 269–275, doi: 10.3189/S0260305500012957, 1993.

Fujita, S., Maeno, H., Uratsuka, S., Furukawa, T., Mae, S., Fujii, Y., and Watanabe, O.: Nature of Radio Echo Layering in the Antarctic Ice Sheet Detected by a Two-Frequency Experiment, Journal of Geophysical Research: Solid Earth, 104, 13 013–13 024, doi: 10/d7q7jq, 1999.

Fujita, S., Matsuoka, T., Ishida, T., Matsuoka, K., and Mae, S.: A Summary of the Complex Dielectric Permittivity of Ice in the Megahertz Range and Its Applications for Radar Sounding of Polar Ice Sheets, Physics of Ice Core Records, pp. 185–212, 2000.

Fujita, S., Matsuoka, K., Maeno, H., and Furukawa, T.: Scattering of VHF Radio Waves from within an Ice Sheet Containing the Vertical-Girdle-Type Ice Fabric and Anisotropic Reflection Boundaries, Annals of Glaciology, 37, 305–316, doi: 10/c4p56s, 2003.

Fujita, S., Maeno, H., and Matsuoka, K.: Radio-Wave Depolarization and Scattering within Ice Sheets: A Matrix-Based Model to Link Radar and Ice-Core Measurements and Its Application, Journal of Glaciology, 52, 407–424, doi: 10/dhz7vf, 2006.

Fürst, J. J., Goelzer, H., and Huybrechts, P.: Ice-Dynamic Projections of the Greenland Ice Sheet in Response to Atmospheric and Oceanic Warming, The Cryosphere, 9, 1039–1062, doi: 10.5194/tc-9-1039-2015, 2015.

Fyke, J., Sergienko, O., Löfverström, M., Price, S., and Lenaerts, J. T. M.: An Overview of Interactions and Feedbacks Between Ice Sheets and the Earth System, Reviews of Geophysics, 56, 361–408, doi: 10.1029/2018RG000600, 2018.

Gagliardini, O., Gillet-Chaulet, F., and Montagnat, M.: A Review of Anisotropic Polar Ice Models : From Crystal to Ice-Sheet Flow Models, Low Temperature Science, 68, 149–166, 2009.

Gagliardini, O., Zwinger, T., Gillet-Chaulet, F., Durand, G., Favier, L., de Fleurian, B., Greve, R., Malinen, M., Martín, C., Råback, P., Ruokolainen, J., Sacchettini, M., Schäfer, M., Seddik, H., and Thies, J.: Capabilities and Performance of Elmer/Ice, a New-Generation Ice Sheet Model, Geoscientific Model Development, 6, 1299–1318, doi: 10.5194/gmd-6-1299-2013, 2013.

Gerber, T. A., Lilien, D. A., Rathmann, N. M., Franke, S., Young, T. J., Valero-Delgado, F., Ershadi, M. R., Drews, R., Zeising, O., Humbert, A., Stoll, N., Weikusat, I., Grinsted, A., Hvidberg, C. S., Jansen, D., Miller, H., Helm, V., Steinhage, D., O'Neill, C., Paden, J., Gogineni, S. P., Dahl-Jensen, D., and Eisen, O.: Crystal Orientation Fabric Anisotropy Causes Directional Hardening of the Northeast Greenland Ice Stream, Nature Communications, 14, 2653, doi: 10.1038/s41467-023-38139-8, 2023.

Gillet-Chaulet, F., Gagliardini, O., Meyssonnier, J., Montagnat, M., and Castelnau, O.: A User-Friendly Anisotropic Flow Law for Ice-Sheet Modeling, Journal of Glaciology, 51, 3–14, doi: 10.3189/172756505781829584, 2005.

Gillet-Chaulet, F., Gagliardini, O., Meyssonnier, J., Zwinger, T., and Ruokolainen, J.: Flow-induced anisotropy in polar ice and related ice-sheet flow modelling, Journal of Non-Newtonian Fluid Mechanics, 134, 33–43, doi: https://doi.org/10.1016/j.jnnfm.2005.11.005, 2nd Annual European Rheology Conference, 2006.

Gillet-Chaulet, F., Hindmarsh, R. C. A., Corr, H. F. J., King, E. C., and Jenkins, A.: In-Situ Quantification of Ice Rheology and Direct Measurement of the Raymond Effect at Summit, Greenland Using a Phase-Sensitive Radar: *IN-SITU* QUANTIFICATION OF ICE RHEOLOGY, Geophysical Research Letters, 38, n/a–n/a, doi: 10.1029/2011GL049843, 2011.

Glen, J. W.: Experiments on the Deformation of Ice, Journal of Glaciology, 2, 111–114, doi: 10.3189/S0022143000034067, 1952.

Glen, J. W. and Perutz, M. F.: The Creep of Polycrystalline Ice, Proceedings of the Royal Society of London. Series A. Mathematical and Physical Sciences, 228, 519–538, doi: 10.1098/rspa.1955.0066, 1997.

Gödert, G.: A Mesoscopic Approach for Modelling Texture Evolution of Polar Ice Including Recrystallization Phenomena, Annals of Glaciology, 37, 23–28, doi: 10/bhns9f, 2003.

Goel, V., Brown, J., and Matsuoka, K.: Glaciological Settings and Recent Mass Balance of Blåskimen Island in Dronning Maud Land, Antarctica, The Cryosphere, 11, 2883–2896, doi: 10.5194/tc-11-2883-2017, 2017.

Goel, V., Martín, C., and Matsuoka, K.: Ice-Rise Stratigraphy Reveals Changes in Surface Mass Balance over the Last Millennia in Dronning Maud Land, Journal of Glaciology, 64, 932–942, doi: 10.1017/jog.2018.81, 2018.

Goel, V., Matsuoka, K., Berger, C. D., Lee, I., Dall, J., and Forsberg, R.: Characteristics of Ice Rises and Ice Rumples in Dronning Maud Land and Enderby Land, Antarctica, Journal of Glaciology, 66, 1064–1078, doi: 10/gm52qg, 2020.

Goldstein, R. M., Engelhardt, H., Kamb, B., and Frolich, R. M.: Satellite Radar Interferometry for Monitoring Ice Sheet Motion: Application to an Antarctic Ice Stream, Science, 262, 1525–1530, doi: 10.1126/science.262.5139.1525, 1993.

Gow, A. J. and Williamson, T.: Rheological Implications of the Internal Structure and Crystal Fabrics of the West Antarctic Ice Sheet as Revealed by Deep Core Drilling at Byrd Station, Geological Society of America Bulletin, 87, 1665, doi: 10/d7chtb, 1976.

Graham, F. S., Morlighem, M., Warner, R. C., and Treverrow, A.: Implementing an Empirical Scalar Constitutive Relation for Ice with Flow-Induced Polycrystalline Anisotropy in Large-Scale Ice Sheet Models, The Cryosphere, 12, 1047–1067, doi: 10.5194/tc-12-1047-2018, 2018.

Greve, R. and Blatter, H.: Dynamics of Ice Sheets and Glaciers, Advances in Geophysical and Environmental Mechanics and Mathematics, Springer Berlin Heidelberg, Berlin, Heidelberg, doi: 10.1007/978-3-642-03415-2, 2009.

Griggs, J. A. and Bamber, J. L.: Antarctic Ice-Shelf Thickness from Satellite Radar Altimetry, Journal of Glaciology, 57, 485–498, doi: 10.3189/002214311796905659, 2011.

Gudmundsson, G. H.: Ice-Shelf Buttressing and the Stability of Marine Ice Sheets, The Cryosphere, 7, 647–655, doi: 10.5194/tc-7-647-2013, 2013.

Gusmeroli, A., Pettit, E. C., Kennedy, J. H., and Ritz, C.: The Crystal Fabric of Ice from Full-Waveform Borehole Sonic Logging, Journal of Geophysical Research: Earth Surface, 117, doi: 10/ghvgjr, 2012.

Hale, R., Miller, H., Gogineni, S., Yan, J. B., Rodriguez-Morales, F., Leuschen, C., Paden, J., Li, J., Binder, T., Steinhage, D., Gehrmann, M., and Braaten, D.: Multi-Channel Ultra-Wideband Radar Sounder and Imager, in: 2016 IEEE International Geoscience and Remote Sensing Symposium (IGARSS), pp. 2112–2115, doi: 10.1109/IGARSS.2016.7729545, 2016.

Hamilton, G. S. and Whillans, I. M.: Point Measurements of Mass Balance of the Greenland Ice Sheet Using Precision Vertical Global Positioning System (GPS) Surveys, Journal of Geophysical Research: Solid Earth, 105, 16 295–16 301, doi: 10.1029/2000JB900102, 2000.

Hamran, S.-E., Paige, D. A., Amundsen, H. E. F., Berger, T., Brovoll, S., Carter, L., Damsgård, L., Dypvik, H., Eide, J., Eide, S., Ghent, R., Helleren, Ø., Kohler, J., Mellon, M., Nunes, D. C., Plettemeier, D., Rowe, K., Russell, P., and Øyan, M. J.: Radar Imager for Mars' Subsurface Experiment—RIMFAX, Space Science Reviews, 216, 128, doi: 10.1007/s11214-020-00740-4, 2020.

Hargreaves, N. D.: The Polarization of Radio Signals in the Radio Echo Sounding of Ice Sheets, Journal of Physics D: Applied Physics, 10, 1285–1304, doi: 10.1088/0022-3727/10/9/012, 1977.

Hargreaves, N. D.: The Radio-Frequency Birefringence of Polar Ice, Journal of Glaciology, 21, 301–313, doi: 10/gjqntq, 1978.

Haseloff, M. and Sergienko, O. V.: The Effect of Buttressing on Grounding Line Dynamics, Journal of Glaciology, 64, 417–431, doi: 10.1017/jog.2018.30, 2018.

Headley, R., Hallet, B., Roe, G., Waddington, E. D., and Rignot, E.: Spatial Distribution of Glacial Erosion Rates in the St. Elias Range, Alaska, Inferred from a Realistic Model of Glacier Dynamics: SEWARD THROAT GLACIAL EROSION RATES, Journal of Geophysical Research: Earth Surface, 117, n/a–n/a, doi: 10/gf2snb, 2012.

Helm, V., Humbert, A., and Miller, H.: Elevation and Elevation Change of Greenland and Antarctica Derived from CryoSat-2, The Cryosphere, 8, 1539–1559, doi: 10/f6hzgq, 2014.

Henry, A. C. J., Drews, R., Schannwell, C., and Višnjević, V.: Hysteretic Evolution of Ice Rises and Ice Rumples in Response to Variations in Sea Level, EGUsphere, pp. 1–25, doi: 10.5194/egusphere-2022-128, 2022.

Hindmarsh, R. C. A., King, E. C., Mulvaney, R., Corr, H. F. J., Hiess, G., and Gillet-Chaulet, F.: Flow at Ice-Divide Triple Junctions: 2. Three-dimensional Views of Isochrone Architecture from Ice-Penetrating Radar Surveys, Journal of Geophysical Research: Earth Surface, 116, doi: 10.1029/2009JF001622, 2011.

Hoffman, A. O., Steen-Larsen, H. C., Christianson, K., and Hvidberg, C.: A Low-Cost Autonomous Rover for Polar Science, Geoscientific Instrumentation, Methods and Data Systems, 8, 149–159, doi: 10.5194/gi-8-149-2019, 2019.

Holt, J. W., Safaeinili, A., Plaut, J. J., Head, J. W., Phillips, R. J., Seu, R., Kempf, S. D., Choudhary, P., Young, D. A., Putzig, N. E., Biccari, D., and Gim, Y.: Radar Sounding Evidence for Buried Glaciers in the Southern Mid-Latitudes of Mars, Science (New York, N.Y.), 322, 1235–1238, doi: 10.1126/science.1164246, 2008.

Hooke, R. L.: Principles of Glacier Mechanics, Cambridge University Press, Cambridge, 2 edn., doi: 10.1017/CBO9780511614231, 2005.

Howat, I., Porter, C., Noh, M.-J., Husby, E., Khuvis, S., Danish, E., Tomko, K., Gardiner, J., Negrete, A., Yadav, B., Klassen, J., Kelleher, C., Cloutier, M., Bakker, J., Enos, J., Arnold, G., Bauer, G., and Morin, P.: The Reference Elevation Model of Antarctica - Strips, Version 4.1, doi: 10.7910/DVN/X7NDNY, 2022.

Howat, I. M., Porter, C., Smith, B. E., Noh, M.-J., and Morin, P.: The Reference Elevation Model of Antarctica, The Cryosphere, 13, 665–674, doi: 10/ggfskk, 2019.

Hutter, K.: Theoretical Glaciology, Springer Netherlands, Dordrecht, doi: 10.1007/978-94-015-1167-4, 1983.

Intergovernmental Panel on Climate Change (IPCC): Climate Change 2022 – Impacts, Adaptation and Vulnerability: Working Group II Contribution to the Sixth Assessment Report of the Intergovernmental Panel on Climate Change, Cambridge University Press, Cambridge, doi: 10.1017/9781009325844, 2023.

Jenkins, A., Corr, H. F., Nicholls, K. W., Stewart, C. L., and Doake, C. S.: Interactions between Ice and Ocean Observed with Phase-Sensitive Radar near an Antarctic Ice-Shelf Grounding Line, Journal of Glaciology, 52, 325–346, doi: 10/bq5mmc, 2006.

Jordan, T. M., Schroeder, D. M., Castelletti, D., Li, J., and Dall, J.: A Polarimetric Coherence Method to Determine Ice Crystal Orientation Fabric From Radar Sounding: Application to the NEEM Ice Core Region, IEEE Transactions on Geoscience and Remote Sensing, 57, 8641–8657, doi: 10/gm5xnk, 2019.

Jordan, T. M., Schroeder, D. M., Elsworth, C. W., and Siegfried, M. R.: Estimation of Ice Fabric within Whillans Ice Stream Using Polarimetric Phase-Sensitive Radar Sounding, Annals of Glaciology, 61, 74–83, doi: 10/ghn49k, 2020.

Kanagaratnam, P., Gogineni, S. P., Gundestrup, N., and Larsen, L.: High-Resolution Radar Mapping of Internal Layers at the North Greenland Ice Core Project, Journal of Geophysical Research: Atmospheres, 106, 33 799–33 811, doi: 10.1029/2001JD900191, 2001.

Karlsson, N. B., Schmidt, L. S., and Hvidberg, C. S.: Volume of Martian Midlatitude Glaciers from Radar Observations and Ice Flow Modeling, Geophysical Research Letters, 42, 2627–2633, doi: 10.1002/2015GL063219, 2015.

Kerch, J., Eisen, O., Eichler, J., Binder, T., Freitag, J., Bohleber, P., Bons, P., and Weikusat, I.: Short-Scale Variations in High-Resolution Crystal-Preferred Orientation Data in an Alpine Ice Core - Do We Need a New Statistical Approach?, Preprint, Geophysics, doi: 10.1002/essoar.10503278.1, 2020.

Kingslake, J., Hindmarsh, R. C. A., Aðalgeirsdóttir, G., Conway, H., Corr, H. F. J., Gillet-Chaulet, F., Martín, C., King, E. C., Mulvaney, R., and Pritchard, H. D.: Full-Depth Englacial Vertical Ice Sheet Velocities Measured Using Phase-Sensitive Radar: Measuring Englacial Ice Velocities, Journal of Geophysical Research: Earth Surface, 119, 2604–2618, doi: 10/ghn5f5, 2014.

Koch, I., Drews, R., Franke, S., Jansen, D., Oraschewski, F. M., Muhle, L. S., Višnjević, V., Matsuoka, K., Pattyn, F., and Eisen, O.: Radar internal reflection horizons from multisystem data reflect ice dynamic and surface accumulation history along the Princess Ragnhild Coast, Dronning Maud Land, East Antarctica, Journal of Glaciology, p. 1–19, doi: 10.1017/jog.2023.93, 2023a.

Koch, I., Drews, R., Muhle, L. S., Franke, S., Jansen, D., Oraschewski, F., Spiegel, H., Višnjević, V., Matsuoka, K., Pattyn, F., and Eisen, O.: Internal Reflection Horizons of Ice Shelves and Ice Rises in Eastern Dronning Maud Land (East Antarctica) from Multisystem Radio-Echo Sounding Data, doi: 10.1594/PANGAEA.950383, 2023b.

Kohler, J., Moore, J. C., and Isaksson, E.: Comparison of Modelled and Observed Responses of a Glacier Snowpack to Ground-Penetrating Radar, Annals of Glaciology, 37, 293–297, doi: 10.3189/172756403781815528, 2003.

Langway, C. C.: Ice Fabrics and the Universal Stage, Report, U.S. Army Snow, Ice, and Permafrost Research Establishment., 1958.

Lauber, J., Hattermann, T., de Steur, L., Darelius, E., Auger, M., Nøst, O. A., and Moholdt, G.: Warming beneath an East Antarctic Ice Shelf Due to Increased Subpolar Westerlies and Reduced Sea Ice, Nature Geoscience, 16, 877–885, doi: 10.1038/s41561-023-01273-5, 2023.

Lenaerts, J. T. M., Brown, J., Broeke, M. R. V. D., Matsuoka, K., Drews, R., Callens, D., Philippe, M., Gorodetskaya, I. V., Meijgaard, E. V., Reijmer, C. H., Pattyn, F., and Lipzig, N. P. M. V.: High Variability of Climate and Surface Mass Balance Induced by Antarctic Ice Rises, Journal of Glaciology, 60, 1101–1110, doi: 10.3189/2014JoG14J040, 2014.

Li, J., Vélez González, J. A., Leuschen, C., Harish, A., Gogineni, P., Montagnat, M., Weikusat, I., Rodriguez-Morales, F., and Paden, J.: Multi-Channel and Multi-Polarization Radar Measurements around the NEEM Site, The Cryosphere, 12, 2689–2705, doi: 10/gd5wwc, 2018.

Lilien, D. A., Rathmann, N. M., Hvidberg, C. S., Grinsted, A., Ershadi, M. R., Drews, R., and Dahl-Jensen, D.: Simulating Higher-Order Fabric Structure in a Coupled, Anisotropic Ice-Flow Model: Application to Dome C, Journal of Glaciology, pp. 1–20, doi: 10.1017/jog.2023.78, 2023.

Lines, A. P., Elliott, J. J., and Ray, L. E.: Incipient Immobilization Detection for Lightweight Rovers Operating in Deformable Terrain, Journal of Autonomous Vehicles and Systems, 2, doi: 10.1115/1.4056408, 2023.

Liu, C., Bentley, C. R., and Lord, N. E.: C Axes from Radar Depolarization Experiments at Upstream B Camp, Antarctica, in 1991–92, Annals of Glaciology, 20, 169–176, doi: 10.3189/1994AoG20-1-169-176, 1994.

Llorens, M.-G., Griera, A., Bons, P. D., Weikusat, I., Prior, D. J., Gomez-Rivas, E., de Riese, T., Jimenez-Munt, I., García-Castellanos, D., and Lebensohn, R. A.: Can Changes in Deformation Regimes Be Inferred from Crystallographic Preferred Orientations in Polar Ice?, The Cryosphere, 16, 2009–2024, doi: 10.5194/tc-16-2009-2022, 2022.

L.Wang, W. and Warner, R. C.: Modelling of Anisotropic Ice Flow in Law Dome, East Antarctica, Annals of Glaciology, 29, 184–190, doi: 10.3189/172756499781820932, 1999.

Macenski, S., Foote, T., Gerkey, B., Lalancette, C., and Woodall, W.: Robot Operating System 2: Design, Architecture, and Uses in the Wild, Science Robotics, 7, eabm6074, doi: 10.1126/scirobotics.abm6074, 2022.

Mankoff, K. D., van As, D., Lines, A., Bording, T., Elliott, J., Kraghede, R., Cantalloube, H., Oriot, H., Dubois-Fernandez, P., du Plessis, O. R., Christiansen, A. V., Auken, E., Hansen, K., Colgan, W., and Karlsson, N. B.: Search and Recovery of Aircraft Parts in Ice-Sheet Crevasse Fields Using Airborne and in Situ Geophysical Sensors, Journal of Glaciology, 66, 496–508, doi: 10.1017/jog.2020.26, 2020.

Martín, C. and Gudmundsson, G. H.: Effects of Nonlinear Rheology, Temperature and Anisotropy on the Relationship between Age and Depth at Ice Divides, The Cryosphere, 6, 1221–1229, doi: 10/f4c9fm, 2012.

Martín, C., Hindmarsh, R. C. A., and Navarro, F. J.: Dating Ice Flow Change near the Flow Divide at Roosevelt Island, Antarctica, by Using a Thermomechanical Model to Predict Radar Stratigraphy, Journal of Geophysical Research: Earth Surface, 111, doi: 10.1029/2005JF000326, 2006.

Martín, C., Gudmundsson, G. H., Pritchard, H. D., and Gagliardini, O.: On the Effects of Anisotropic Rheology on Ice Flow, Internal Structure, and the Age-Depth Relationship at Ice Divides, Journal of Geophysical Research, 114, F04 001, doi: 10/fhvht2, 2009a.

Martín, C., Hindmarsh, R. C. A., and Navarro, F. J.: On the Effects of Divide Migration, along-Ridge Flow, and Basal Sliding on Isochrones near an Ice Divide, Journal of Geophysical Research: Earth Surface, 114, doi: 10/bgz2wj, 2009b.

Matsuoka, K., Furukawa, T., Fujita, S., Maeno, H., Uratsuka, S., Naruse, R., and Watanabe, O.: Crystal Orientation Fabrics within the Antarctic Ice Sheet Revealed by a Multipolarization Plane and Dual-Frequency Radar Survey: RADAR SURVEY OF ANTARCTIC ICE FABRICS, Journal of Geophysical Research: Solid Earth, 108, doi: 10/d5sc97, 2003.

Matsuoka, K., Uratsuka, S., Fujita, S., and Nishio, F.: Ice-Flow-Induced Scattering Zone within the Antarctic Ice Sheet Revealed by High-Frequency Airborne Radar, Journal of Glaciology, 50, 382–388, doi: 10/b6x9nq, 2004.

Matsuoka, K., Wilen, L., Hurley, S., and Raymond, C.: Effects of Birefringence Within Ice Sheets on Obliquely Propagating Radio Waves, IEEE Transactions on Geoscience and Remote Sensing, 47, 1429–1443, doi: 10/dj47fx, 2009.

Matsuoka, K., Power, D., Fujita, S., and Raymond, C. F.: Rapid Development of Anisotropic Ice-Crystal-Alignment Fabrics Inferred from Englacial Radar Polarimetry, Central West Antarctica: RADAR-REVEALED ANISOTROPIC ICE FABRICS, Journal of Geophysical Research: Earth Surface, 117, n/a–n/a, doi: 10/gm5xnm, 2012.

Matsuoka, K., Hindmarsh, R. C., Moholdt, G., Bentley, M. J., Pritchard, H. D., Brown, J., Conway, H., Drews, R., Durand, G., Goldberg, D., Hattermann, T., Kingslake, J., Lenaerts, J. T., Martín, C., Mulvaney, R., Nicholls, K. W., Pattyn, F., Ross, N., Scambos, T., and Whitehouse, P. L.: Antarctic Ice Rises and Rumples: Their Properties and Significance for Ice-Sheet Dynamics and Evolution, Earth-Science Reviews, 150, 724–745, doi: 10/f7z95x, 2015.

Matsuoka, T., Fujita, S., Morishima, S., and Mae, S.: Precise Measurement of Dielectric Anisotropy in Ice Ih at 39 GHz, Journal of Applied Physics, 81, 2344–2348, doi: 10/c5zkfj, 1997.

Miners, W. D., Hildebrand, A., Gerland, S., Blindow, N., Steinhage, D., and Wolff, E. W.: Forward Modeling of the Internal Layers in Radio Echo Sounding Using Electrical and Density Measurements from Ice Cores, The Journal of Physical Chemistry B, 101, 6201–6204, doi: 10.1021/jp963218+, 1997.

Miners, W. D., Wolff, E. W., Moore, J. C., Jacobel, R., and Hempel, L.: Modeling the Radio Echo Reflections inside the Ice Sheet at Summit, Greenland, Journal of Geophysical Research: Solid Earth, 107, EPM 6–1–EPM 6–11, doi: 10.1029/2001JB000535, 2002.

Montagnat, M., Buiron, D., Arnaud, L., Broquet, A., Schlitz, P., Jacob, R., and Kipfstuhl, S.: Measurements and Numerical Simulation of Fabric Evolution along the Talos Dome Ice Core, Antarctica, Earth and Planetary Science Letters, 357–358, 168–178, doi: 10/gm5xnp, 2012.

Montagnat, M., Azuma, N., Dahl-Jensen, D., Eichler, J., Fujita, S., Gillet-Chaulet, F., Kipfstuhl, S., Samyn, D., Svensson, A., and Weikusat, I.: Fabric along the NEEM Ice Core, Greenland, and Its Comparison with GRIP and NGRIP Ice Cores, The Cryosphere, 8, 1129–1138, doi: 10/gb9p3v, 2014.

Moore, J. C.: Dielectric Variability of a 130 m Antarctic Ice Core: Implications for Radar Sounding, Annals of Glaciology, 11, 95–99, doi: 10.3189/S026030550000639X, 1988.

Morlighem, M.: MEaSUREs BedMachine Antarctica, Version 3, doi: 10.5067/FPSU0V1MWUB6, 2022.

Morlighem, M., Rignot, E., Binder, T., Blankenship, D., Drews, R., Eagles, G., Eisen, O., Ferraccioli, F., Forsberg, R., Fretwell, P., Goel, V., Greenbaum, J. S., Gudmundsson, H., Guo, J., Helm, V., Hofstede, C., Howat, I., Humbert, A., Jokat, W., Karlsson, N. B., Lee, W. S., Matsuoka, K., Millan, R., Mouginot, J., Paden, J., Pattyn, F., Roberts, J., Rosier, S., Ruppel, A., Seroussi, H., Smith, E. C., Steinhage, D., Sun, B., van den Broeke, M. R., van Ommen, T. D., van Wessem, M., and Young, D. A.: Deep Glacial Troughs and Stabilizing Ridges Unveiled beneath the Margins of the Antarctic Ice Sheet, Nature Geoscience, 13, 132–137, doi: 10/gjqnwz, 2020.

Naughten, K. A., Holland, P. R., and De Rydt, J.: Unavoidable Future Increase in West Antarctic Ice-Shelf Melting over the Twenty-First Century, Nature Climate Change, pp. 1–7, doi: 10.1038/s41558-023-01818-x, 2023.

Nereson, N. A. and Waddington, E. D.: Isochrones and Isotherms beneath Migrating Ice Divides, Journal of Glaciology, 48, 95–108, doi: 10.3189/172756502781831647, 2002.

Nereson, N. A., Hindmarsh, R. C. A., and Raymond, C. F.: Sensitivity of the Divide Position at Siple Dome, West Antarctica, to Boundary Forcing, Annals of Glaciology, 27, 207–214, doi: 10.3189/1998AoG27-1-207-214, 1998.

Nicholls, K. W., Corr, H. F., Stewart, C. L., Lok, L. B., Brennan, P. V., and Vaughan, D. G.: A Ground-Based Radar for Measuring Vertical Strain Rates and Time-Varying Basal Melt Rates in Ice Sheets and Shelves, Journal of Glaciology, 61, 1079–1087, doi: 10/ghhvzt, 2015.

Nobes, D. C.: Ground Penetrating Radar Measurements Over Glaciers, in: Encyclopedia of Snow, Ice and Glaciers, edited by Singh, V. P., Singh, P., and Haritashya, U. K., Encyclopedia of Earth Sciences Series, pp. 490–503, Springer Netherlands, Dordrecht, doi: 10.1007/978-90-481-2642-2_230, 2011.

Oraschewski, F. M., Koch, I., Ershadi, M. R., Hawkins, J., Eisen, O., and Drews, R.: Layer-optimized SAR processing with a mobile phase-sensitive radar for detecting the deep englacial stratigraphy of Colle Gnifetti, Switzerland/Italy, EGUsphere, 2023, 1–21, doi: 10.5194/egusphere-2023-2731, 2023.

Paden, J., Mathews, R., jiluli, mohanadalibadi, theresa-moore, da Silva, V. B., jsprick, Talasila, H. M., Gordon, Holschuh, N., gamer10bm, Barnett, C., Aegidius7, Hsien), S. C. K., Ibikunle, Jutila, A., Choudhari, R., and Christoffersen, M.: CReSIS/Cresis-Toolbox: CReSIS Toolbox Version 3.01, Zenodo, doi: 10.5281/zenodo.5683959, 2021.

Paren, J. G.: Reflection Coefficient at a Dielectric Interface, Journal of Glaciology, 27, 203–204, doi: 10/gjqns9, 1981.

Parrenin, F., Jouzel, J., Kawamura, K., Lemieux-Dudon, B., Loulergue, L., Masson-Delmotte, V., Narcisi, B., Raisbeck, G., Raynaud, D., Ruth, U., Schwander, J., Severi, M., Spahni, R., Steffensen, J. P., Svensson, A., Udisti, R., Waelbroeck, C., and Wolff, E.: The EDC3 Chronology for the EPICA Dome C Ice Core, Clim. Past, p. 13, doi: 10/drbxns, 2007.

Passchier, C. W.: The Fabric Attractor, Journal of Structural Geology, 19, 113–127, doi: 10.1016/S0191-8141(96)00077-6, 1997.

Pattyn, F., Wauthy, S., Sun, S., Tison, J.-L., and Tsibulskaya, V.: Polarimetric Radar Data and Ice Core Data Collected at Hammarryggen Ice Rise, Antarctica, doi: 10.5281/zenodo.8095508, 2023.

Petit, R. J., Aguinagalde, I., de Beaulieu, J.-L., Bittkau, C., Brewer, S., Cheddadi, R., Ennos, R., Fineschi, S., Grivet, D., Lascoux, M., Mohanty, A., Müller-Starck, G., Demesure-Musch, B., Palmé, A., Martín, J. P., Rendell, S., and Vendramin, G. G.: Glacial Refugia: Hotspots but Not Melting Pots of Genetic Diversity, Science (New York, N.Y.), 300, 1563–1565, doi: https://www.science.org/doi/10.1126/science.1083264, 2003.

Pettit, E. C., Thorsteinsson, T., Jacobson, H. P., and Waddington, E. D.: The Role of Crystal Fabric in Flow near an Ice Divide, Journal of Glaciology, 53, 277–288, doi: 10/fq47nj, 2007.

Philippe, M., Tison, J.-L., Fjøsne, K., Hubbard, B., Kjær, H. A., Lenaerts, J. T. M., Drews, R., Sheldon, S. G., De Bondt, K., Claeys, P., and Pattyn, F.: Ice Core Evidence for a 20th Century Increase in Surface Mass Balance in Coastal Dronning Maud Land, East Antarctica, The Cryosphere, 10, 2501–2516, doi: 10.5194/tc-10-2501-2016, 2016.

Picotti, S., Vuan, A., Carcione, J. M., Horgan, H. J., and Anandakrishnan, S.: Anisotropy and Crystalline Fabric of Whillans Ice Stream (West Antarctica) Inferred from Multicomponent Seismic Data, Journal of Geophysical Research: Solid Earth, 120, 4237–4262, doi: 10.1002/2014JB011591, 2015.

Pirazzini, R.: Surface Albedo Measurements over Antarctic Sites in Summer, Journal of Geophysical Research: Atmospheres, 109, doi: 10.1029/2004JD004617, 2004.

Powell, M. J. D.: Variable Metric Methods for Constrained Optimization, in: Mathematical Programming The State of the Art: Bonn 1982, edited by Bachem, A., Korte, B., and Grötschel, M., pp. 288–311, Springer, Berlin, Heidelberg, doi: 10.1007/978-3-642-68874-4_12, 1983.

Rathmann, N. M., Lilien, D. A., Grinsted, A., Gerber, T. A., Young, T. J., and Dahl-Jensen, D.: On the Limitations of Using Polarimetric Radar Sounding to Infer the Crystal Orientation Fabric of Ice Masses, Geophysical Research Letters, 49, e2021GL096 244, doi: 10/gpch5q, 2022.

Ray, L., Adolph, A., Morlock, A., Walker, B., Albert, M., Lever, J. H., and Dibb, J.: Autonomous Rover for Polar Science Support and Remote Sensing, in: 2014 IEEE Geoscience and Remote Sensing Symposium, pp. 4101–4104, doi: 10.1109/IGARSS.2014.6947388, 2014.

Raymond, C. F.: Deformation in the Vicinity of Ice Divides, Journal of Glaciology, 29, 357–373, doi: 10/gjqnvn, 1983.

Rémy, F. and Tabacco, I. E.: Bedrock Features and Ice Flow near the EPICA Ice Core Site (Dome C, Antarctica), Geophysical Research Letters, 27, 405–408, doi: 10/cnkmhz, 2000.

Ridley, J. K., Cudlip, W., and Laxon, S. W.: Identification of Subglacial Lakes Using ERS-1 Radar Altimeter, Journal of Glaciology, 39, 625–634, doi: 10.3189/S002214300001652X, 1993.

Rignot, E. and Jacobs, S. S.: Rapid Bottom Melting Widespread near Antarctic Ice Sheet Grounding Lines, Science, 296, 2020–2023, doi: 10.1126/science.1070942, 2002.

Rignot, E., Mouginot, J., and Scheuchl., B.: MEaSUREs InSAR-Based Antarctica Ice Velocity Map, Version 2, doi: 10.5067/D7GK8F5J8M8R, 2017.

Rignot, E., Mouginot, J., Scheuchl, B., van den Broeke, M., van Wessem, M. J., and Morlighem, M.: Four Decades of Antarctic Ice Sheet Mass Balance from 1979–2017, Proceedings of the National Academy of Sciences, 116, 1095–1103, doi: 10.1073/pnas.1812883116, 2019.

Rintoul, S. R., Silvano, A., Pena-Molino, B., van Wijk, E., Rosenberg, M., Greenbaum, J. S., and Blankenship, D. D.: Ocean Heat Drives Rapid Basal Melt of the Totten Ice Shelf, Science Advances, 2, e1601 610, doi: 10.1126/sciadv.1601610, 2016.

Robel, A. A., Wilson, E., and Seroussi, H.: Layered Seawater Intrusion and Melt under Grounded Ice, The Cryosphere, 16, 451–469, doi: 10.5194/tc-16-451-2022, 2022.

Rodriguez-Morales, F., Gogineni, S., Leuschen, C. J., Paden, J. D., Li, J., Lewis, C. C., Panzer, B., Gomez-Garcia Alvestegui, D., Patel, A., Byers, K., Crowe, R., Player, K., Hale, R. D., Arnold, E. J., Smith, L., Gifford, C. M., Braaten, D., and Panton, C.: Advanced Multifrequency Radar Instrumentation for Polar Research, IEEE Transactions on Geoscience and Remote Sensing, 52, 2824–2842, doi: 10.1109/TGRS.2013.2266415, 2014.

Russell, J. L.: Southern Ocean Heat Sink Hindered by Melting Ice, Nature, 615, 799–800, doi: 10.1038/d41586-023-00835-2, 2023.

Schannwell, C., Drews, R., Ehlers, T. A., Eisen, O., Mayer, C., and Gillet-Chaulet, F.: Kinematic Response of Ice-Rise Divides to Changes in Ocean and Atmosphere Forcing, The Cryosphere, 13, 2673–2691, doi: 10/gm5xnt, 2019.

Schannwell, C., Drews, R., Ehlers, T. A., Eisen, O., Mayer, C., Malinen, M., Smith, E. C., and Eisermann, H.: Quantifying the Effect of Ocean Bed Properties on Ice Sheet Geometry over 40 000 Years with a Full-Stokes Model, The Cryosphere, 14, 3917–3934, doi: 10/ghm3hq, 2020.

Schroeder, D. M.: Paths Forward in Radioglaciology, Annals of Glaciology, pp. 1–5, doi: 10.1017/aog.2023.3, 2023.

Seddik, H., Greve, R., Placidi, L., Hamann, I., and Gagliardini, O.: Application of a Continuum-Mechanical Model for the Flow of Anisotropic Polar Ice to the EDML Core, Antarctica, Journal of Glaciology, 54, 631–642, doi: 10/c9s97b, 2008.

Seddik, H., Greve, R., Zwinger, T., and Placidi, L.: A Full Stokes Ice Flow Model for the Vicinity of Dome Fuji, Antarctica, with Induced Anisotropy and Fabric Evolution, The Cryosphere, 5, 495–508, doi: 10.5194/tc-5-495-2011, 2011.

Seidov, D. and Haupt, B. J.: How to Run a Minimalist's Global Ocean Conveyor, Geophysical Research Letters, 32, doi: 10.1029/2005GL022559, 2005.

Seo, M., Kim, H.-C., Huh, M., Yeom, J.-M., Lee, C. S., Lee, K.-S., Choi, S., and Han, K.-S.: Long-Term Variability of Surface Albedo and Its Correlation with Climatic Variables over Antarctica, Remote Sensing, 8, 981, doi: 10.3390/rs8120981, 2016.

Seroussi, H., Nowicki, S., Payne, A. J., Goelzer, H., Lipscomb, W. H., Abe-Ouchi, A., Agosta, C., Albrecht, T., Asay-Davis, X., Barthel, A., Calov, R., Cullather, R., Dumas, C., Galton-Fenzi, B. K., Gladstone, R., Golledge, N. R., Gregory, J. M., Greve, R., Hattermann, T., Hoffman, M. J., Humbert, A., Huybrechts, P., Jourdain, N. C., Kleiner, T., Larour, E., Leguy, G. R., Lowry, D. P., Little, C. M., Morlighem, M., Pattyn, F., Pelle, T., Price, S. F., Quiquet, A., Reese, R., Schlegel, N.-J., Shepherd, A., Simon, E., Smith, R. S., Straneo, F., Sun, S., Trusel, L. D., Van Breedam, J., van de Wal, R. S. W., Winkelmann, R., Zhao, C., Zhang, T., and Zwinger, T.: ISMIP6 Antarctica: A Multi-Model Ensemble of the Antarctic Ice Sheet Evolution over the 21st Century, The Cryosphere, 14, 3033–3070, doi: 10.5194/tc-14-3033-2020, 2020.

Seu, R., Phillips, R. J., Biccari, D., Orosei, R., Masdea, A., Picardi, G., Safaeinili, A., Campbell, B. A., Plaut, J. J., Marinangeli, L., Smrekar, S. E., and Nunes, D. C.: SHARAD Sounding Radar on the Mars Reconnaissance Orbiter, Journal of Geophysical Research: Planets, 112, doi: 10.1029/2006JE002745, 2007.

Shepherd, T. G., Boyd, E., Calel, R. A., Chapman, S. C., Dessai, S., Dima-West, I. M., Fowler, H. J., James, R., Maraun, D., Martius, O., Senior, C. A., Sobel, A. H., Stainforth, D. A., Tett, S. F. B., Trenberth, K. E., van den Hurk, B. J. J. M., Watkins, N. W., Wilby, R. L., and Zenghelis, D. A.: Storylines: An Alternative Approach to Representing Uncertainty in Physical Aspects of Climate Change, Climatic Change, 151, 555–571, doi: 10.1007/s10584-018-2317-9, 2018.

Siegert, M. J. and Kwok, R.: Ice-Sheet Radar Layering and the Development of Preferred Crystal Orientation Fabrics between Lake Vostok and Ridge B, Central East Antarctica, Earth and Planetary Science Letters, 179, 227–235, doi: 10.1016/S0012-821X(00)00121-7, 2000.

Smith, E. C., Baird, A. F., Kendall, J. M., Martín, C., White, R. S., Brisbourne, A. M., and Smith, A. M.: Ice Fabric in an Antarctic Ice Stream Interpreted from Seismic Anisotropy, Geophysical Research Letters, 44, 3710–3718, doi: 10/f983xm, 2017.

Sun, S., Hattermann, T., Pattyn, F., Nicholls, K. W., Drews, R., and Berger, S.: Topographic Shelf Waves Control Seasonal Melting Near Antarctic Ice Shelf Grounding Lines, Geophysical Research Letters, 46, 9824–9832, doi: 10.1029/2019GL083881, 2019.

Surawy-Stepney, T., Hogg, A. E., Cornford, S. L., and Hogg, D. C.: Mapping Antarctic Crevasses and Their Evolution with Deep Learning Applied to Satellite Radar Imagery, The Cryosphere, 17, 4421–4445, doi: 10.5194/tc-17-4421-2023, 2023.

Tabacco, I. E., Bianchi, C., Zirizzotti, A., Zuccheretti, E., Forieri, A., and Vedova, A. D.: Airborne Radar Survey above Vostok Region, East-Central Antarctica: Ice Thickness and Lake Vostok Geometry, Journal of Glaciology, 48, 62–69, doi: 10.3189/172756502781831656, 2002.

Thompson, S. S., Cook, S., Kulessa, B., Winberry, J. P., Fraser, A. D., and Galton-Fenzi, B. K.: Comparing Satellite and Helicopter-Based Methods for Observing Crevasses, Application in East Antarctica, Cold Regions Science and Technology, 178, 103 128, doi: 10.1016/j.coldregions.2020.103128, 2020.

Thorsteinsson, T., Kipfstuhl, J., and Miller, H.: Textures and Fabrics in the GRIP Ice Core, Journal of Geophysical Research: Oceans, 102, 26 583–26 599, doi: 10.1029/97JC00161, 1997.

Trautmann, E., Ray, L., and Lever, J.: Development of an Autonomous Robot for Ground Penetrating Radar Surveys of Polar Ice, in: 2009 IEEE/RSJ International Conference on Intelligent Robots and Systems, pp. 1685–1690, doi: 10.1109/IROS.2009.5354290, 2009.

Tsutaki, S., Fujita, S., Kawamura, K., Abe-Ouchi, A., Fukui, K., Motoyama, H., Hoshina, Y., Nakazawa, F., Obase, T., Ohno, H., Oyabu, I., Saito, F., Sugiura, K., and Suzuki, T.: High-Resolution Subglacial Topography around Dome Fuji, Antarctica, Based on Ground-Based Radar Surveys over 30 Years, The Cryosphere, 16, 2967–2983, doi: 10.5194/tc-16-2967-2022, 2022.

Ulaby, F. and Elachi, C.: Radar Polaritnetry for Geoscience Applications, Geocarto International, 5, 38–38, doi: 10/ctmgm7, 1990.

Vaňková, I., Cook, S., Winberry, J. P., Nicholls, K. W., and Galton-Fenzi, B. K.: Deriving Melt Rates at a Complex Ice Shelf Base Using In Situ Radar: Application to Totten Ice Shelf, Geophysical Research Letters, 48, e2021GL092 692, doi: https://doi.org/10.1029/2021GL092692, e2021GL092692 2021GL092692, 2021.

Vittuari, L., Vincent, C., Frezzotti, M., Mancini, F., Gandolfi, S., Bitelli, G., and Capra, A.: Space Geodesy as a Tool for Measuring Ice Surface Velocity in the Dome C Region and along the ITASE Traverse, Annals of Glaciology, 39, 402–408, doi: 10/fscdbv, 2004.

Walford, M. E. R. and Harper, M. F. L.: The Detailed Study of Glacier Beds Using Radio-Echo Techniques, Geophysical Journal International, 67, 487–514, doi: 10.1111/j.1365-246X.1981.tb02762.x, 1981.

Waltz, R., Morales, J., Nocedal, J., and Orban, D.: An Interior Algorithm for Nonlinear Optimization That Combines Line Search and Trust Region Steps, Mathematical Programming, 107, 391–408, doi: 10/dp848r, 2006.

Wang, B., Tian, G., Cui, X., and Zhang, X.: The Internal COF Features in Dome A of Antarctica Revealed by Multi-Polarization-Plane RES, Applied Geophysics, 5, 230–237, doi: 10.1007/s11770-008-0029-z, 2008.

Wang, Z., Chung, A., Steinhage, D., Parrenin, F., Freitag, J., and Eisen, O.: Mapping Age and Basal Conditions of Ice in the Dome Fuji Region, Antarctica, by Combining Radar Internal Layer Stratigraphy and Flow Modeling, The Cryosphere, 17, 4297–4314, doi: 10.5194/tc-17-4297-2023, 2023.

Wauthy, S., Tison, J.-L., Inoue, M., El Amri, S., Sun, S., Claeys, P., and Pattyn, F.: Physico-Chemical Properties of the Top 120 m of Two Ice Cores in Dronning Maud Land (East Antarctica): An Open Window on Spatial and Temporal Regional Variability of Environmental Proxies, Earth System Science Data Discussions, pp. 1–33, doi: 10.5194/essd-2023-152, 2023.

Weikusat, I., Jansen, D., Binder, T., Eichler, J., Faria, S. H., Wilhelms, F., Kipfstuhl, S., Sheldon, S., Miller, H., Dahl-Jensen, D., and Kleiner, T.: Physical Analysis of an Antarctic Ice Core—towards an Integration of Micro- and Macrodynamics of Polar Ice, Philosophical Transactions of the Royal Society A: Mathematical, Physical and Engineering Sciences, 375, 20150 347, doi: 10/gmf6vq, 2017.

Wendler, G. and Kelley, J.: On the Albedo of Snow in Antarctica: A Contribution to I.A.G.O., Journal of Glaciology, 34, 19–25, doi: 10.3189/S0022143000009011, 1988.

Wesche, C., Eisen, O., Oerter, H., Schulte, D., and Steinhage, D.: Surface Topography and Ice Flow in the Vicinity of the EDML Deep-Drilling Site, Antarctica, Journal of Glaciology, 53, 442–448, doi: 10/fcc9z8, 2007.

Wesche, C., Steinhage, D., and Nixdorf, U.: Polar Aircraft Polar5 and Polar6 Operated by the Alfred Wegener Institute, Journal of large-scale research facilities JLSRF, 2, A87–A87, doi: 10.17815/jlsrf-2-153, 2016a.

Wesche, C., Weller, R., König-Langlo, G., Fromm, T., Eckstaller, A., Nixdorf, U., and Kohlberg, E.: Neumayer III and Kohnen Station in Antarctica Operated by the Alfred Wegener Institute, Journal of large-scale research facilities JLSRF, 2, A85–A85, doi: 10.17815/jlsrf-2-152, 2016b.

Westhoff, J., Stoll, N., Franke, S., Weikusat, I., Bons, P., Kerch, J., Jansen, D., Kipfstuhl, S., and Dahl-Jensen, D.: A Stratigraphy-Based Method for Reconstructing Ice Core Orientation, Annals of Glaciology, pp. 1–12, doi: 10/gm5xnx, 2020.

Williams, M. J. M., Warner, R. C., and Budd, W. F.: The Effects of Ocean Warming on Melting and Ocean Circulation under the Amery Ice Shelf, East Antarctica, Annals of Glaciology, 27, 75–80, doi: 10.3189/1998AoG27-1-75-80, 1998.

Wilson, C. J. L., Russell-Head, D. S., and Sim, H. M.: The Application of an Automated Fabric Analyzer System to the Textural Evolution of Folded Ice Layers in Shear Zones, Annals of Glaciology, 37, 7–17, doi: 10.3189/172756403781815401, 2003.

Winebrenner, D. P., Smith, B. E., Catania, G. A., Conway, H. B., and Raymond, C. F.: Radio-Frequency Attenuation beneath Siple Dome,West Antarctica, from Wide-Angle and Profiling Radar Observations, Annals of Glaciology, 37, 226–232, doi: 10/db824p, 2003.

Winkelmann, R., Martin, M. A., Haseloff, M., Albrecht, T., Bueler, E., Khroulev, C., and Levermann, A.: The Potsdam Parallel Ice Sheet Model (PISM-PIK) – Part 1: Model Description, The Cryosphere, 5, 715–726, doi: 10.5194/tc-5-715-2011, 2011.

Woodcock, N. H.: Specification of Fabric Shapes Using an Eigenvalue Method, Geological Society of America Bulletin, 88, 1231, doi: 10/fw4xp7, 1977.

Woodruff, A. H. W. and Doake, C. S. M.: Depolarization of Radio Waves Can Distinguish between Floating and Grounded Ice Sheets, Journal of Glaciology, 23, 223–232, doi: 10/gjqntb, 1979.

Yan, J.-B., Li, L., Nunn, J. A., Dahl-Jensen, D., O'Neill, C., Taylor, R. A., Simpson, C. D., Wattal, S., Steinhage, D., Gogineni, P., Miller, H., and Eisen, O.: Multiangle, Frequency, and Polarization Radar Measurement of Ice Sheets, IEEE Journal of Selected Topics in Applied Earth Observations and Remote Sensing, 13, 2070–2080, doi: 10/gm5xpc, 2020.

Young, T. J., Martín, C., Christoffersen, P., Schroeder, D. M., Tulaczyk, S. M., and Dawson, E. J.: Rapid and Accurate Polarimetric Radar Measurements of Ice Crystal Fabric Orientation at the Western Antarctic Ice Sheet (WAIS) Divide Ice Core Site, The Cryosphere, 15, 4117–4133, doi: 10.5194/tc-15-4117-2021, 2021.

Zeising, O., Steinhage, D., Nicholls, K. W., Corr, H. F. J., Stewart, C. L., and Humbert, A.: Basal Melt of the Southern Filchner Ice Shelf, Antarctica, The Cryosphere, 16, 1469–1482, doi: 10.5194/tc-16-1469-2022, 2022.

Zeising, O., Gerber, T. A., Eisen, O., Ershadi, M. R., Stoll, N., Weikusat, I., and Humbert, A.: Improved Estimation of the Bulk Ice Crystal Fabric Asymmetry from Polarimetric Phase Co-Registration, The Cryosphere, 17, 1097–1105, doi: 10.5194/tc-17-1097-2023, 2023.

"Yesterday I was clever, so I wanted to change the world.
Today I am wise, so I am changing myself."
Rumi

به هر جا که هستید خروش آورید
جهنده جهان را به جوش آورید

همه یک به یک مهربانی کنید
به کل جهان پاسبانی کنید

به صلح جهانی بکوشید سخت
به فر جهان باور نیک بخت

جهان را بسازید همچون بهشت
مگوئید هرگز سخن های زشت

بگوئید این جمله درگوش باد
چو ایران نباشد تن من مباد

Ferdosi